Moisture Effects and Viscoelasticity in Polymers Used for Microelectronic Packaging

by

Promod Roy Chowdhury

A dissertation submitted to the Graduate Faculty of
Auburn University
in partial fulfillment of the
requirements for the Degree of
Doctor of Philosophy

Auburn, Alabama
December 14, 2019

Keywords: underfill, solder mask, moisture, mechanical properties, viscoelastic, and finite element analysis

Copyright 2019 by Promod Roy Chowdhury

Approved by

Jeffrey C. Suhling, Chair, Quina Distinguished Professor of Mechanical Engineering
Hareesh V. Tippur, McWane Professor of Mechanical Engineering
Peter Schwartz, Professor Emeritus of Mechanical Engineering
Edward Davis, Assistant Professor of Materials Engineering

Abstract

In the microelectronics packaging industry, polymer based materials are used widely. Reliable, consistent and comprehensive material property data are required for mechanical design, process optimization, and reliability assessment of electronic packages. In this study, mechanical behavior and mechanical properties of underfill encapsulants and solder mask materials have been investigated. Due to absorption of moisture, softening of the polymer materials can occur as well as new failure modes in electronic assemblies (e.g. popcorn failure).

In the first part of this work, the effects of moisture absorption on the stress-strain and creep behavior of an underfill encapsulant were evaluated experimentally. The fabricated and preconditioned uniaxial test specimens were then exposed to moisture for various durations (0, 1, 3, 10, 20, 30, 60 days) in an environmental chamber using three different sets of hygrothermal conditions based on the JEDEC standard. After the moisture exposures, a microscale tension-torsion testing machine was used to measure the room temperature stress-strain behavior of the material. In addition, the viscoelastic mechanical responses of the underfill encapsulant after the moisture exposures were also characterized via creep testing for a large range of applied stress levels. From the recorded results, it was found that the moisture exposures degrade the mechanical properties of the tested underfill including the effective elastic modulus, ultimate tensile stress, and tensile creep rate. Pre-

baking was found to increase the initial material properties before moisture exposure, but the degradations due to subsequent moisture exposures occurred in an analogous manner. The moisture absorption into the underfill samples was also characterized by weight gain measurements for up to 60 days of exposure. From the results, it has been shown that maximum water weight gain in the material is about 1%. The results also showed that mechanical properties were only dependent on amount of water that has been absorbed by the material, regardless of how rapidly it was absorbed.

In the second part of this study, both frequency dependent dynamic mechanical analysis (DMA) measurements and strain and temperature dependent stress relaxation experiments were performed on a typical underfill material in order to characterize its linear viscoelastic behavior. In both cases, a master curve was determined using the assumption of time-temperature equivalence, and Prony series expansions were utilized to model the material's relaxation behavior. For both sets of experimental input data, the Prony pairs and shift factors were determined, and the master curves at the reference temperature were shifted to other temperatures for comparing with experimental data. Finally, the developed viscoelastic models were used to both predict the rate dependent stress-strain behavior and the creep behavior of the material. The model predictions were correlated with additional experimental data not used to establish the viscoelastic model, and good correlations were obtained. The developed viscoelastic model for underfill was then used in finite element models of underfilled ball grid array packages (Ultra CSP) subjected to thermal cycling from -40 to 125 ^{o}C. Separate simulations were also performed using temperature dependent elastic properties for the underfill material. In both cases, the solder joint fatigue life was estimated, and the effects of using viscoelastic properties for

the underfill in solder joint fatigue life simulation were investigated. Using elastic properties of the underfill material overestimates the failure life by calculating lower plastic work.

In the third part of this work, the mechanical behavior of a typical UV curable solder mask material has also been explored as a function of ultra violet (UV) curing time, testing temperature, and isothermal aging exposure. In this study, a unique sample preparation technique has been developed to make 80 x 3 mm uniaxial tension test samples with a defined thickness (e.g. 0.30 mm), and both stress-strain and creep tests were performed. The mechanical behavior changes of the solder mask material were recorded for different curing profiles including various durations of UV exposure and subsequent isothermal curing. The results showed that an optimum UV exposure time was critical to provide acceptable mechanical properties. In addition, the stress-strain and creep behavior of the solder mask were recorded for various temperatures from 25 to 125 ^{o}C, and the mechanical properties were found to degrade significantly at elevated temperatures. The experimental results showed that variations of thermal curing profile (curing temperature and time) also change the mechanical properties significantly, so that solder masks have a very small optimum processing window. Finally, the effects of isothermal aging at 100 ^{o}C on the material behavior were characterized for different aging times. Using the recorded data, the changes in the elastic modulus, strength, and creep rate were characterized as a function of aging time. Significant variations were observed in the elastic modulus and ultimate strength of the aged samples.

Acknowledgments

I would like to express my sincere gratitude to my advisor Dr. Jeffrey C. Suhling for the continuous support and guidance of my research work. Also, I would like to thank the rest of my dissertation committee: Dr. Hareesh V. Tippur, Dr. Peter Schwartz, and Dr. Edward Davis, for their encouragement and insightful discussions. I would also like to thank Dr. Sa'd Hamasha for serving as the university reader of this dissertation.

I also appreciate the cooperation, discussions and friendship that from all my co-workers and friends, especially Jordan Roberts, Nusrat Chhanda. Special thanks are also extended to all my co-workers and friends, Mohammad Motalab, Safina Hussain, Munshi Basit, Md. Hasnine, Sudan Ahmed, Quang Nguyen, Mohammad Alam, Abdullah Fahim, Md. Mahmudur Chowdhury, KM Rafidh Hasan, Jing Wu, Jun Chen, Mohd Aminul Hoque, Kamrul Hasan, Mohammad Ashraful Haq, Mr. Jason Smith and Mr. John Marcell for their support.

I would also like to take this opportunity to gratefully thankful to my parents, Prabir Roy Chowdhury and Sukla Roy Chowdhury for their unconditional support. I would also like to thank my brother, Pronob Roy Chowdhury for his encouragement.

Finally, I would like to acknowledge my wife Priyanka Pinky for her understanding and love during the study period. Her support and encouragement was in the end what made this dissertation possible.

Table of Contents

Abstract ii

Acknowledgments v

Table of Contents vi

List of Tables ii

List of Figures iii

CHAPTER 1 1

INTRODUCTION 1

1.1 Electronic Packaging 1

1.1.1 First-Level Packaging: 2
1.1.2 Second-Level Packaging 4

1.2 Polymeric Material in Microelectronic Packaging: 6

1.2.1 Underfill 6
1.2.2 Solder Mask 9

1.3 Packaging Related Issues in Mechanical Engineering: 10

1.3.1 Thermomechanical Reliability 11
1.3.2 Moisture Related Problems 11
1.3.3 Electromigration 13
1.3.4 Thermal Management 13
1.3.5 Reliability under Shock or Vibration 13
1.3.6 Combined Loading Conditions 14

1.4 Objective of This Research: 14

1.5 Organization of the Dissertation: 15

CHAPTER 2 17

LITERATURE REVIEW 17

2.1 Introduction 17

2.2 Fabrication and Characterization of Polymer 18

2.3 Effects of Moisture on Material Properties 19

2.4 Viscoelastic Modeling of Underfill Materials 22

2.5 Effect of Viscoelastic Response on Thermal cycling Solder Joint Reliability....26
2.6 Mechanical Behavior of Solder Mask....28
2.7 Summary....30
CHAPTER 3 32
SPECIMEN PREPARATION AND EXPERIMENTAL SETUP.... 32
3.1 Introduction....32
3.2 Specimen Preparation Procedure....33
3.2.1 Underfill.... 33
3.2.2 Solder Mask 36
3.3 Mechanical Testing System....38
3.4 Typical Testing Data and Data Processing....41
3.4.1 Stress-Strain Curve 41
3.4.2 Creep Test 43
3.4.3 Stress Relaxation Test.... 45
3.5 Dynamic Mechanical Analysis (DMA) 48
3.6 Environmental Test Chamber 52
3.7 Electronic Balance 53
3.8 Microstructural Study 53
3.9 Summary....55
CHAPTER 4 56
EXPERIMENTAL CHARACTERIZATION OF UNDERFILL MATERIALS EXPOSED TO DIFFERENT MOISTURE CONDITIONS.... 56
4.1 Introduction....56
4.2 Theoretical Background....57
4.3 Filler Morphology....60
4.4 Stress – Strain Study....60
4.4.1 Moisture Exposure at 85 ^{o}C/85 % RH including Preconditioning 63
4.4.2 Several Moisture Exposure.... 67
4.5 Creep Study....70
4.6 Moisture Absorption Study....74
4.7 Material Property Variation with Moisture Concentration....78
4.8 Summary and Discussion....81
CHAPTER 5 83

CHARACTERIZATION OF VISCOELASTIC RESPONSE OF UNDERFILL MATERIALS 83
5.1 Introduction 83
5.2 Generalized Maxwell Model 83
5.3 Time-Temperature Superposition and Shift Functions 88
5.3.1 Master Curve 89
5.3.2 Shift Functions 90
5.4 Experimental Procedure 92
5.5 Poisson's Ratio Tests 105
5.6 Stress Relaxation Tests 109
5.7 Summary and Discussion 125
CHAPTER 6 127
MODELING OF UNDERFILLED BGA ASSEMBLIES USING BOTH VISCOELASTIC AND ELASTIC MATERIAL PROPERTIES 127
6.1 Introduction 127
6.2 Finite Element Modeling 128
6.3 Loads and Boundary Conditions 133
6.4 Package Design 137
6.5 FEA Results 143
6.6 Summary and Discussion 149
CHAPTER 7 150
THE EFFECTS OF CURING PROFILE, TEMPERATURE, AND AGING OF THE MECHANICAL BEHAVIOR OF SOLDER MASK MATERIALS 150
7.1 Introduction 150
7.2 Test Specimen Preparation 153
7.3 Variation with UV Curing Time 156
7.4 Variation with Temperature 163
7.5 Thermal Curing Time Variation 167
7.6 Aging Study 173
7.7 Creep Study 178
7.8 Summary and Discussion 180
CHAPTER 8 181
CONCLUSIONS 181
8.1 Literature Review 181

8.2 Specimen Preparation and Experimental Setup 181
8.3 Effect of Moisture on the Mechanical Properties of Underfill 181
8.4 Viscoelastic Modeling of Underfill 183
8.5 Thermal Cycling Reliability Prediction using Finite Element Analysis for Underfill BGA Assemblies with Viscoelastic Underfill 183
8.6 Effects of Curing Profile, Temperature, and Aging of the Mechanical Behavior of Solder Mask Materials 184
8.7 Future Work 185
REFERENCES 186
APPENDIX 194

List of Tables

Table 1-1 Key properties of Underfill Materials [13] 9
Table 4-1 Material Property Variation (No Preconditioning) 65
Table 4-2 Material Property Variation (Preconditioning for 24 Hours at 85 ^{o}C) 65
Table 4-3 Material Property Variation with Moisture Exposure Conditions 68
Table 4-4 Creep Strain Rate Variation at MSL 1 73
Table 4-5 Creep Strain Rate Variation at MSL 2 73
Table 4-6 Creep Strain Rate Variation at MSL 3 74
Table 4-7 Measured Diffusivity Values 76
Table 5-1 Calculated shift factor for a reference temperature of T0 = 120 °C 99
Table 5-2 Calculated Prony constants for Shear and Bulk Response 108
Table 5-3 Calculated shift factor 113
Table 5-4 Calculated Prony pairs at a reference temperature of 120 °C 115
Table 5-5 Calculated 13 Prony pairs from Stress relaxation test 122
Table 5-6 Calculated 17 Prony pairs from Stress relaxation tests 123
Table 5-7 Calculated 17 Prony pairs from Stress relaxation tests 123
Table 6-1 SAC 305 Anand Viscoplastic Coefficient 135
Table 6-2 Material Properties of Different Components 135
Table 6-3 Temperature Dependent Underfill Elastic 136
Table 6-4 Prony Coefficients for Shear Response 136
Table 6-5 Prony Coefficients for Bulk Response 137
Table 6-6 Darveaux Constants [102] 147
Table 6-7 Plastic Work per Cycle and Time to Failure 148

List of Figures

Figure 1-1 Microelectronic Packaging [1] 2
Figure 1-2 Conventional versus no-flow underfilling process flow [5] 7
Figure 1-3 Schematic diagram of flip-chip underfill encapsulation [8] 8
Figure 1-4 Solder Mask 10
Figure 1-5 Popcorn Failure Caused by Moisture [13] 12
Figure 2-1 Fracture toughness for a Si/UF/Si assembly under different enviromental condition [34] 21
Figure 2-2 Flowchart for viscoelasticity modeling [58] 23
Figure 2-3 Master Curve Generated by Shifting the Relaxation moduli [71] 25
Figure 2-4 Master Curve Generation from DMA [72] 26
Figure 2-5 Modeling methods to calculate solder fatigue life [77] 28
Figure 3-1 (a) Mold Assembly for Underfill (b) Underfill Test Specimens 34
Figure 3-2 Specimen Preparation Machine and Mold Assembly 34
Figure 3-3 Box Oven for Curing 35
Figure 3-4 Mold Assembly for Sample Preparation 36
Figure 3-5 Typical UV Flood-Lamp System 37
Figure 3-6 UV exposed Sample 37
Figure 3-7 Test Specimens 38
Figure 3-8 Testing System 40
Figure 3-9 Chamber for Elevated Temperature Testing (+25 to +300 ^{o}C) 40
Figure 3-10 Chamber for Low Temperature Testing (-185 to +25 ^{o}C) 40
Figure 3-11 Typical Polymer Stress-Strain Curve and Material Properties 41
Figure 3-12 Typical Creep Curves 43
Figure 3-13 Creep Curve and Log Hyperbolic Tangent Model Fit 45
Figure 3-14 Difference between Creep test and Stress relaxation test 46
Figure 3-15 Stress Relaxation Test (Stress vs Time) 47
Figure 3-16 Relaxation Modulus vs Time 47

Figure 3-17 Fitted Experimental data 47
Figure 3-18 Average Curve for Relaxation Modulus 48
Figure 3-19 TA Instruments RSA3 DMA System..... 49
Figure 3-20 Test Specimens..... 49
Figure 3-21 Frequency Sweep / Temperature Step Test..... 50
Figure 3-22 Testing Performed at frequency 1 Hz 51
Figure 3-23 Humidity Chambers Used for Moisture Exposure..... 52
Figure 3-24 High Precision Electronic Scale..... 53
Figure 3-25 JEOL JSM-7000F Field Emission SEM 54
Figure 3-26 Various Signals at Different Depths within the Sample [91]..... 54
Figure 4-1 SEM Micrograph of Underfill Encapsulant 60
Figure 4-2 Experimental Stress- Strain Curve 61
Figure 4-3 No Moisture Exposure, No Preconditioning..... 61
Figure 4-4 Experimental Stress- Strain Curve 62
Figure 4-5 Stress-Strain Curves for Underfill (No Moisture Exposure, Preconditioned at 24 Hours at 85 oC)..... 63
Figure 4-6 No preconditioning, 60 days of at MSL 1..... 64
Figure 4-7 Preconditioned, 60 days of at MSL 1..... 64
Figure 4-8 Variation of Initial Elastic Modulus with duration of Moisture Exposure 65
Figure 4-9 Variation of Ultimate Tensile Strength with duration of Moisture Exposure 66
Figure 4-10 Stress Strain Curves for 60 Days of Moisture Exposure..... 67
Figure 4-11 Elastic Modulus Variation with Moisture Exposure Time (85/85, 85/60, 30/60) 69
Figure 4-12 Ultimate Tensile Strength variation with Moisture Exposure Time (85/85, 85/60, 30/60)..... 70
Figure 4-13 Typical Creep Curves..... 71
Figure 4-14 No Moisture Exposure 72
Figure 4-15 60 Days of Moisture Exposure at 85 ^{o}C /85 % RH..... 72
Figure 4-16 60 Days of Moisture Exposure at 85 ^{o}C /60 % RH..... 73
Figure 4-17 Secondary Creep Rate Variations with Moisture Exposure Time 74
Figure 4-18 Moisture Mass vs. Exposure Time and Fit of Fickian Model (MSL 1)..... 76
Figure 4-19 Moisture Mass vs. Exposure Time for Different MSL Exposure Conditions 76
Figure 4-20 Moisture Content vs. Exposure Time for Various MSL Levels 77

Figure 4-21 Moisture Concentration vs. Exposure Time for Various MSL Levels 78
Figure 4-22 Elastic Modulus vs. Concentration for Different MSL Exposure Conditions 79
Figure 4-23 Ultimate Tensile Strength vs. Concentration for Different MSL Exposure Conditions 79
Figure 4-24 Elastic Modulus vs. Concentration for Different MSL Exposure Conditions (Single Linear Fit) 80
Figure 4-25 Ultimate Tensile Strength vs. Concentration for Different MSL Exposure Conditions (Single Linear Fit) 80
Figure 4-26 Creep Rate vs. Concentration 81
Figure 5-1 Maxwell Model 84
Figure 5-2 Generalized Maxwell Model 85
Figure 5-3 Schematic of a Flip Chip on Laminate Assembly 91
Figure 5-4 TA Instruments RSA3 DMA System 93
Figure 5-5 Test Specimens 94
Figure 5-6 Frequency Sweep / Temperature Step Test 94
Figure 5-7 Testing Performed at frequency 1 Hz 95
Figure 5-8 Testing Performed at frequency: 0.1, 0.5, 1, 1.5, 2, 3, 5, 10 Hz 96
Figure 5-9 Testing Performed at frequency: 0.1, 0.5, 1, 1.5, 2, 3, 5, 10 Hz 96
Figure 5-10 Frequency dependence of the storage modulus of a cured underfill at different isothermal temperatures. 97
Figure 5-11 Master curves generated by shifting the storage (E´) using the TTS principle with respect to a reference temperature of 120 °C 98
Figure 5-12 Horizontal shift factor vs temperature for a reference temperature of T_0 = 120 °C 99
Figure 5-13 Master curve generated by shifting the storage (E´) using the TTS principle with respect to a reference temperature of 120 °C 100
Figure 5-14 Master curves generated by shifting the storage modulus (E´), the loss modulus (E´´), and the loss tangent curves using the TTS principle with respect to a reference temperature of 120 °C 101
Figure 5-15 Conversion from frequency to time domain 103
Figure 5-16 Relaxation Modulus vs Time 104
Figure 5-17 Poisson's ratio test 105
Figure 5-18 Poisson's ratio test data 106
Figure 5-19 Shear Modulus vs Time 107
Figure 5-20 Bulk Modulus vs Time 108

Figure 5-21 Stress Relaxation Test (Stress vs Time) 109
Figure 5-22 Relaxation Modulus vs Time 110
Figure 5-23 Fitted Experimental data 110
Figure 5-24 Average Curve for Relaxation Modulus 111
Figure 5-25 Relaxation Modulus vs Time at different temperatures 111
Figure 5-26 Horizontally shifted the curve for generating master curve at a reference temperature of 120 °C 112
Figure 5-27 Shifted curve to reference temperature of 120 °C 113
Figure 5-28 Master curve generated at a reference temperature of 120 °C 114
Figure 5-29 Comparison between generated master curve using DMA and stress relaxation test 114
Figure 5-30 Calculated Shift factor 115
Figure 5-31 Stress Strain test at different temperatures between -55 °C to 125 °C 116
Figure 5-32 Finite element modeling for stress strain and creep test 117
Figure 5-33 Boundary conditions for Tensile and Creep test 117
Figure 5-34 Comparison between experimental and finite element modeling using 7 Prony pairs for shear and bulk modulus from DMA experiment 118
Figure 5-35 Comparison between experimental and finite element modeling using 13 Prony pairs for shear and bulk modulus from stress relaxation test data 119
Figure 5-36 Comparison between experimental and finite element modeling using 17 Prony pairs for shear and bulk modulus from stress relaxation test data 119
Figure 5-37 Comparison between experimental and finite element modeling using 17 Prony pairs from stress relaxation test data at -55 °C 120
Figure 5-38 Comparison between experimental and finite element modeling using 17 Prony pairs from stress relaxation test data at 25 °C 120
Figure 5-39 Comparison between experimental and finite element modeling using 17 Prony pairs from stress relaxation test data at 85 °C 121
Figure 5-40 Comparison between experimental and finite element modeling using 17 Prony pairs from stress relaxation test data at 100 °C 121
Figure 5-41 Stress Relaxation master curve fitting using 7 Prony Pair 124
Figure 5-42 Stress Relaxation master curve fitting using 13 Prony Pair 124
Figure 5-43 Stress Relaxation master curve fitting using 17 Prony Pair 125
Figure 6-1 Deformation due to CTE mismatch 128
Figure 6-2 Interfacial Failure in Solder Joint 129
Figure 6-3 Plastic Work 130

Figure 6-4 Possible failure regions. Volume Averaging done within this to Predict Time to Failure 131
Figure 6-5 Solder joint fatigue life prediction method 133
Figure 6-6 Temperature Profile of Thermal Cycling 134
Figure 6-7 Package 138
Figure 6-8 Cross section of Chip Scale Package (Ultra CSP) 138
Figure 6-9 Chip Scale Package cross-section 139
Figure 6-10 Chip Scale Package cross-section 140
Figure 6-11 FEA Mesh for Quarter Model (without Underfill) 141
Figure 6-12 FEA Mesh for the Solder Balls 142
Figure 6-13 FEA Mesh for the Solder Balls 142
Figure 6-14 Contours of Accumulated Plastic Work (MPa) without underfill 143
Figure 6-15 Quarter Model with Underfill 144
Figure 6-16 Contours of Accumulated Plastic Work (MPa) (Underfill elastic Property) 145
Figure 6-17 Contours of Accumulated Plastic Work (MPa) Underfill Viscoelastic Property 146
Figure 6-18 Volume Averaged Accumulated Plastic Work Vs Time up to Third Thermal Cycle 147
Figure 6-19 Variation of Failure Life for Different Model 148
Figure 7-1 Solder Mask 151
Figure 7-2 Solder Mask Cross-Section 151
Figure 7-3 Mold Assembly for Sample Preparation 154
Figure 7-4 Typical UV Flood-Lamp System 154
Figure 7-5 UV exposed Sample 155
Figure 7-6 Test Specimens 156
Figure 7-7 Stress Strain Tests at T = 25 ^{o}C 157
Figure 7-8 UV curing Time 30 sec 157
Figure 7-9 UV curing Time 60 sec 158
Figure 7-10 UV curing Time 90 sec 158
Figure 7-11 UV curing Time 110 sec 159
Figure 7-12 UV curing Time 115 sec 159
Figure 7-13 UV curing Time 120 sec 160
Figure 7-14 UV curing Time 130 sec 160

Figure 7-15 UV curing Time 30 minutes 161
Figure 7-16 Stress vs. Strain Test Results for exposure times from 0-110 sec 161
Figure 7-17 Stress vs. Strain (Exposure time 110-1800 sec) 162
Figure 7-18 Elastic Modulus vs. UV exposure time 162
Figure 7-19 UTS vs. UV exposure time 163
Figure 7-20 Stress Strain test at T = 50 ^{o}C 164
Figure 7-21 Stress Strain test at T = 75 ^{o}C 164
Figure 7-22 Stress Strain test at T = 100 ^{o}C 165
Figure 7-23 Stress Strain test at T = 125 ^{o}C 165
Figure 7-24 Stress-Strain Curve at Different Temperatures 166
Figure 7-25 Elastic Modulus vs. Temperature 166
Figure 7-26 Ultimate Tensile Strength vs. Temperature 167
Figure 7-27 Stress Strain test at T = 25 ^{o}C (no thermal curing) 168
Figure 7-28 Thermal curing 50 ^{o}C for 1 hour 168
Figure 7-29 Thermal curing 75 ^{o}C for 1 hour 169
Figure 7-30 Thermal curing 100 ^{o}C for 1 hour 169
Figure 7-31 Thermal curing 125 ^{o}C for 1 hour 170
Figure 7-32 Thermal curing 140 ^{o}C for 1 hour 170
Figure 7-33 Thermal curing 150 ^{o}C for 1 hour 171
Figure 7-34 Thermal curing 175 ^{o}C for 1 hour 171
Figure 7-35 Average Stress-Strain Curve at different Thermal Curing 172
Figure 7-36 Elastic Modulus vs. Curing Temperature 172
Figure 7-37 Ultimate Tensile Strength vs. Curing Temperature 173
Figure 7-38 Stress Strain Curve (Aging for 1 hour at 100 ^{o}C) 174
Figure 7-39 Stress Strain Curve (Aging for 2 hours at 100 ^{o}C) 174
Figure 7-40 Stress Strain Curve (Aging for 5 hours at 100 oC) 175
Figure 7-41 Stress Strain Curve (Aging for 10 hours at 100 ^{o}C) 175
Figure 7-42 Stress Strain Curve (Aging for 15 hours at 100 ^{o}C) 176
Figure 7-43 Average Stress-Strain Curves for Different Aging Time 176
Figure 7-44 Elastic Modulus vs. Aging Time 177
Figure 7-45 Ultimate Tensile Strength vs. Aging Time 177
Figure 7-46 Empirical Model Fit 179
Figure 7-47 Creep Data at Different Stress Level 179

CHAPTER 1

INTRODUCTION

1.1 Electronic Packaging

Electronic packaging technology is the science of establishing interconnections between various levels of electronic devices, components, modules, and system. Electronic packaging refers to the placement and connection of many electronic and electromechanical components in an enclosure that protects the system from the environment and provides easy access for routine maintenance. It determines the cost, performance and reliability of almost all future commercial and military electronics equipment. The most compact and high density electronic packaging is flip chip technology. Most flip chip assemblies require underfill to improve their reliability to acceptable levels. Otherwise, the small solder joints are subjected to high shear strains due to the thermos-mechanical mismatch between die and substrate. The four major functions of an electronic package include

a. Signal Distribution

b. Power Distribution

c. Heat Dissipation

d. Protection of the Components and Interconnections

Generally the packaging system can be divided into several interconnect levels. At the first level, the integrated circuit (IC) chip and a substrate or chip carried are connected by one of three methods: wire bonding, tape-automated bonding (TAB), and flip chip technology. At second level, the substrate or chip carried is connected to a printed wiring board (PWB). This attachment can be achieved by using plated through hole (PTH)

technology or surface mount technology (SMT). At third level, the PWB is connected to a motherboard. Figure 1-1 [1] illustrates a typical configuration for electronic packaging technology.

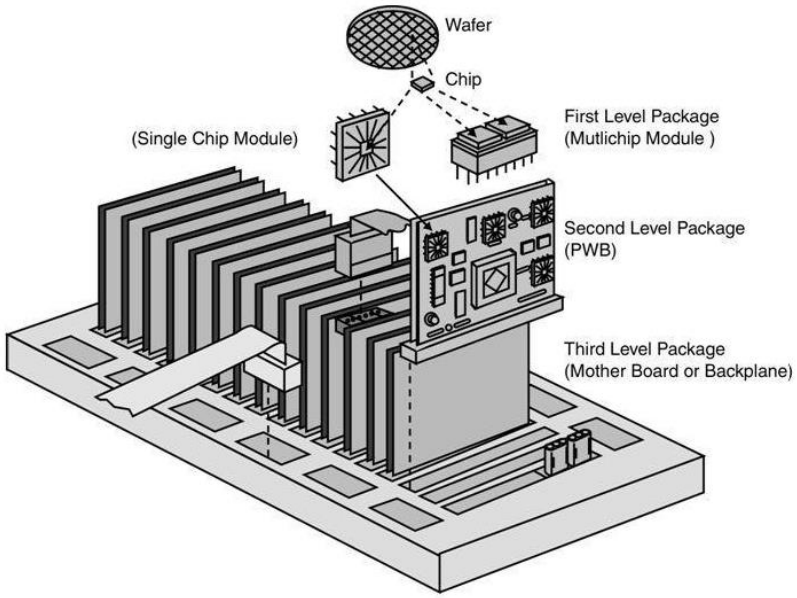

Figure 1-1 Microelectronic Packaging [1]

1.1.1 First-Level Packaging:

First-level packages can be classified into several categories based on the type of chip–substrate interconnect, substrate material, type of chip coverage, method of connection to the circuit board, and the shape and location of connections.

The connection of the chip to the substrate is a key technology for first-level packaging. For this key step, the three common bonding technologies are as follows: wire bonding, flip-chip bonding, and tape-automated bonding (TAB). In wire bonding, the silicon die is placed on the top of the substrate with a chip pad facing upwards, and metal wires are used to form the electrical connection between the chip and substrate by forming

a ball or wedge bond. The most common combination of materials involves the bonding of a gold wire to an aluminum pad, while copper and aluminum wires are also widely used. Thermosonic, thermocompression, and ultrasonic methods can be employed for forming a bond. Wire bonding is widely used in packaging IC, MEMS, and light-emitting diodes (LEDs) [2], [3].

In the 1960s, IBM developed the flip-chip technology [4], [5], which is a method involving the connection of the chip to the substrate by conductive bumps. In this technology, the bumps are formed on the chip pads, and then chip is "flipped" and connected to the substrate. The conductive bumps serve as both mechanical and electrical connections. Flip-chip bonding not only significantly decreases the size of the package, but also leads to an increased number of inputs/outputs (I/Os) and better performance than wire bonding. Typically, flip-chip bumps are made by solder material by a reflow process, known as controlled collapse chip connection (C4), while other bumping (such as conductive adhesive and stub bond) and bonding methods (such as thermocompression) are also employed. For alleviating the mechanical stress induced by the coefficient of thermal expansion (CTE) mismatch and enhancing the reliability under temperature-cycling conditions, underfill material is typically dispensed in the gap between the chip and substrate.

For TAB, the chip is first placed onto a flexible tape, and connected to the inner leads, creating interconnections, followed by testing. Then, the tape is moved to the target location, and the outer leads are cut and connected to the PCB substrate; finally, the package is encapsulated, and final testing is performed [2], [6].

1.1.2 Second-Level Packaging

The first-level packages have to be further connected to the board for serving their functions, and the assembly of chip modules and other components on the PCBs is referred to as second-level packaging. Two common mounting schemes are as follows: pin-in-hole (PIH) and surface mount (SMT). The interconnections may be located in one or two lines on the periphery or on the bottom of the package as an array. SMT packages may have several different interconnected structures, such as ball grid array (BGA), land grid array (LGA), column grid array (CGA), J-lead, and gull wing. The connection can be designed to be pluggable if customization or replacement is often needed.

Electronic packaging serves as an important relation between the silicon and the electronic system. A variety of electronic packaging technologies have been developed to achieve the aims of lower cost, better reliability and higher density/performance. Flip chip technology, also referred to as direct chip attach (DCA) technology, is potentially attractive for a large variety of microelectronics packaging application, because it provides fast clock frequency and large package pin counts.

In order to perpetuate this trend and be able to meet future market growth prediction, technologies associated with the flip chip package are currently being improved with plans for further developments in the future. Developments include improvements in the C4 interconnect technology, the underfill technique, and the substrate technology. Higher interconnect density is a driving force for research and development of the flip chip package. To meet this need, research is being done to increase reliability issues of the C4 bump and underfill technique.

The original flip chip did not contain underfill and corner solder joint failure due to CTE mismatch between the chip and substrate was the main concern. Great effort was

made to improve the flip chip design. The introduction of underfill [7] encapsulated between the chip and the PCB has considerably enhanced the solder fatigue life. The epoxy-based underfill reduces the global thermal expansion mismatch between the silicon chip and the low-cost organic substrate. Since the chip, underfill and substrate deform together as a unit, the relative deformation between the chip and the substrate is minimized and the corresponding shear deformation of the solder joint is small [2].

Although the use of the underfill encapsulant eliminates, to a large extent, the problem of low-cycle solder fatigue, a number of reliability issues remain. The underfill layer shifts the local shear strain from the solder balls to the underfill/die and the underfill/substrate interfaces, causing delamination of these interfaces [7]. Once delamination occurs, crack will propagate along the interfaces and quickly sever the solder joints, leading to the eventual failure of the whole package.

Another problem is that the underfill, which is epoxy-based, is susceptible to moisture. Moisture may cause hydroxylation and swelling of epoxy and thus degrade the adhesive strength of the underfill. Especially, when the temperature is high (e.g., during reflow process), moisture in the underfill will vaporize and turn into high-pressure steam, which could be sufficient to cause delamination within the package, or even worse, an internal or external crack in the plastic package. Cracks in the plastic package would allow easy moisture penetration, inducing transport of ionic contaminants to the die surface and increasing the potential for early device failure. Even at the relatively low temperatures, e.g., 85 °C, the moisture swelling and plasticization will greatly change the material properties as well as residual stress in sandwich specimen, which can consequently menace package reliability issues.

1.2 Polymeric Material in Microelectronic Packaging:

1.2.1 Underfill

Underfill materials are critical for achieving reliability of several packaging architectures. These materials are added to provide a stronger mechanical connection and reduce the solder joint strains occurring with temperature changes due to the mismatches of coefficients of thermal expansion (CTE) of the various assembly materials. Underfill can lessen the influence of the global thermal expansion mismatch between the silicon chip and the substrate. It can lower the stresses and strains in the solder bumps and rearrange them over the whole chip area; otherwise they would be increasingly focused near the corner solder bumps of the chip. Since its origins at IBM in the 1970s, underfill technology has been part of the electronics manufacturing landscape [4]. There are three types of underfill systems currently in use: capillary underfills, fluxing (no-flow) underfills, and 4-corner or corner-dot underfill systems. While all have their advantages and limitations, capillary underfills are the most widely used of these materials. Capillary underfills provide reliability enhancement by equally distributing stress across the chip's surface. In this process, the chip is attached to the substrate onto deposited solder paste attachment sites. When it is reflowed, a metallic interconnection is formed. Material flows underneath the package and gaps between the CSP and substrate are encapsulated. Figure 1-2 compares the processing steps of capillary underfill and no-flow underfill

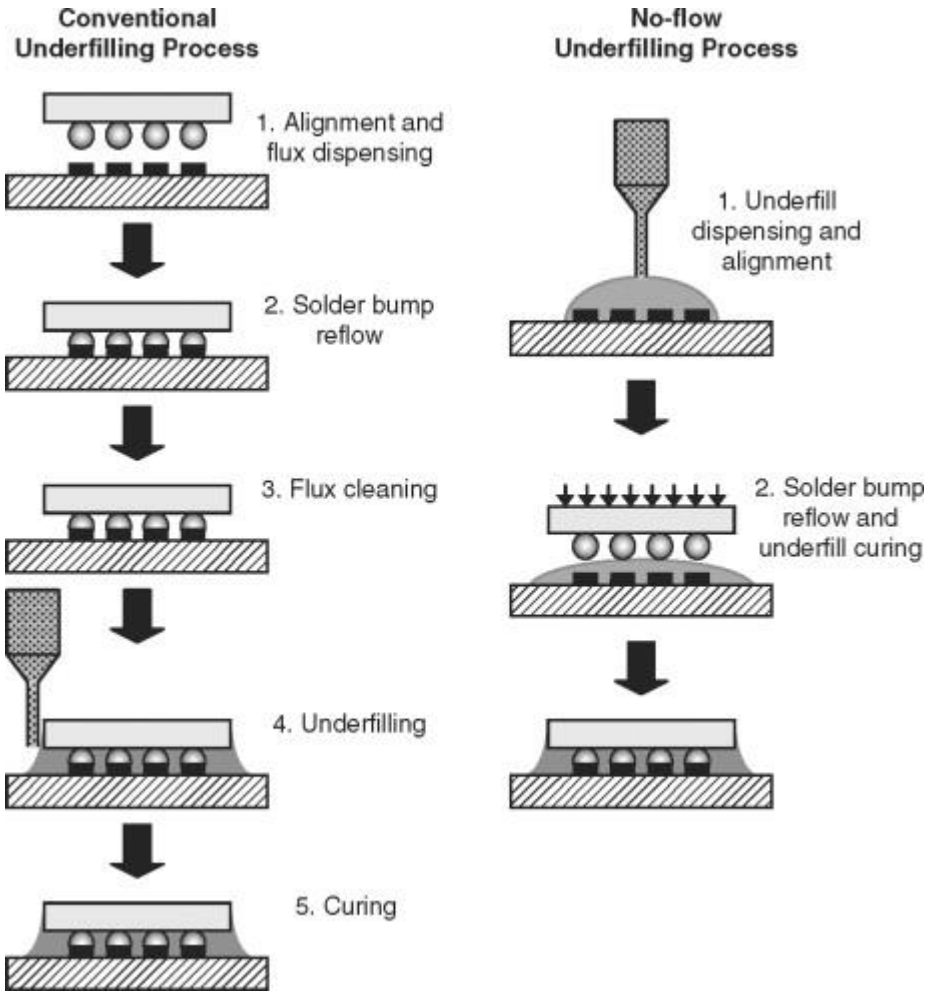

Figure 1-2 Conventional versus no-flow underfilling process flow [5]

Underfill material acts as cushion layer during thermal cycling and effectively protects the solder joints from being damaged. The underfilling process involves dispensing a controlled amount of material into a gap between a chip and substrate as shown in Figure 1-3. The underfill material is dispensed along a line adjacent to the edge of the die where capillary action wicks the material beneath the die, filling the spaces between the die, substrate, and interconnect bumps. It is critical that the gap between the die and the substrate is completely filled with underfill material, as the life of the chip

assembly is dependent on it. To ensure that the material flows correctly, the substrate needs to be uniformly heated. If the temperature is too high, the dispensed underfill may not run completely and may result in lengthy flow time or incomplete filling.

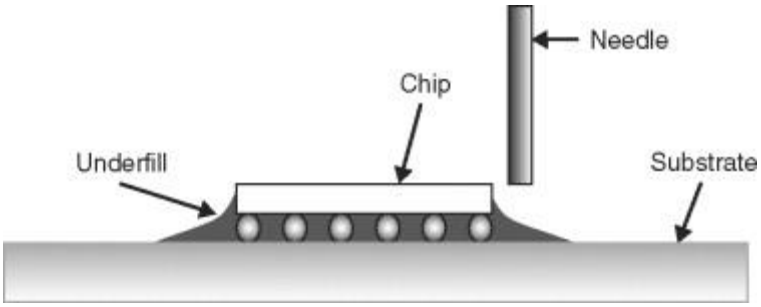

Figure 1-3 Schematic diagram of flip-chip underfill encapsulation [8]

The flow of the capillary underfill has been extensively and the flow is usually slow and can be incomplete, resulting in voids in the packages and non-homogeneity in the resin/filler system. When the chip size increases, the filling problem becomes more critical. The flow modeling of flip chip underfill is often approximated as viscous flow of the underfill adhesive between two parallel plates. Hele-Shaw model can be used to simulate the underfill flow. The time required to fill a chip of length L can be calculated as [8]–[12].

$$t_{fill} = \frac{3\eta L^2}{\sigma h \cos\theta} \tag{1.1}$$

Where η is the underfill viscosity; σ is the coefficient of the surface tension; θ is the contact angle; and h is the gap distance. It is easily predict that a larger chip with a smaller gap distance would require longer time to fill.

Table 1-1 Key properties of Underfill Materials [13]

Property	**Comments**
Viscosity, flow properties	Want low viscosity and good flow so that underfill can completely fill the small gaps (50–100 μm high) between chip and substrate
Silica filler content	Filler is needed to lower the polymer's CTE to match that of the solder bumps
Filler size, distribution, and shape	Filler size, distribution, and shape affect flow properties
Thermoset polymer chemistry	Want polymer system with high glass transition temperature (Tg) for stable mechanical properties
Young's modulus	Want modulus as high as possible to enable good mechanical coupling between chip and substrate
Cure cycle	Cure cycle must be relatively short and appropriate for manufacturing
Adhesion	Want excellent adhesion to chip and ceramic surfaces when cured
Moisture sensitivity	Want excellent moisture resistance
Ionic contamination	Want low ionic contamination for semiconductor applications
Quality control	Need tight quality control on underfi ll materials
Cost	Need to produce high quality material at reasonable cost

1.2.2 Solder Mask

Solder mask is a lacquer-like layer of polymer that delivers everlasting protective coating for the copper traces of a printed circuit board. It prevents solder from connecting between conductors, in that way stopping short circuits. Solder mask was produced mainly

to expedite wave soldering used in mass assembly. Solder mask is usually green but is now offered in many colors.

Solder mask or solder resist becomes increasingly important for circuit boards as density of boards increased and SMT (Surface Mount Technology) become the key aspect due to market demand. As its name specifies, solder mask purposes to halt soldering bridges from taking place on covered area. Reflow soldering plays a vital role in SMT assembly as it makes electronic components completely and precisely mounted on circuit boards through solder paste. If solder mask isn't used, copper traces tend to be coupled with solder paste which will possibly create short cuts. As a result, the assembled PCBs' reliability and performance will be comprised. Apart from its main duty, solder mask is also able to stop copper traces from corrosion, oxidation, and dirt.

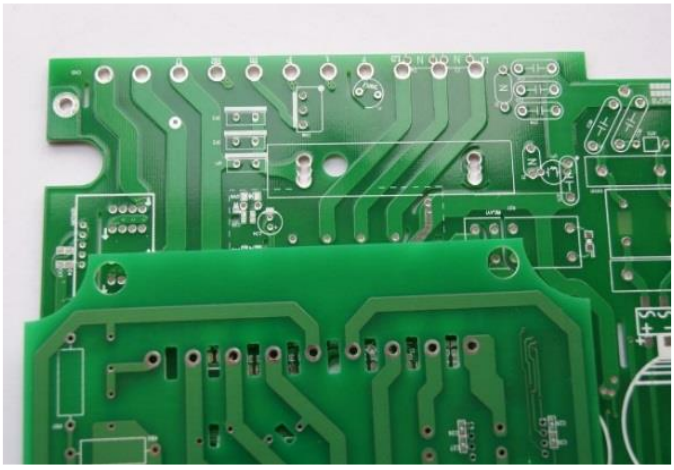

Figure 1-4 Solder Mask

1.3 Packaging Related Issues in Mechanical Engineering:

Electronic packaging is an interdisciplinary area involving material science, electrical engineering, mechanical engineering, supply chain, and logistics. Within the

domain of mechanical engineering, issues are predominantly divided into two categories: thermal management and stresses induced by temperature and other environmental effects such as vibration and moisture.

1.3.1 Thermomechanical Reliability

An electronic package is composed of different materials, and each material has its own CTE. Thermomechanical stresses are caused by the CTE mismatch between different materials. The electronic packaging process consists of multiple process steps, and the process temperature of each step can significantly vary. Hence, thermomechanical stresses exist in almost any electronic package. In addition, these packages experience temperature loading from internal heat sources and the environment. Thermomechanical stress can adversely affect the reliability and performance of electronic components. The electronic components may fail because of over-stress failure; however, fatigue failure is more prevalent. For example, the temperature of the components increases when the devices are powered on and decreases when they are powered off. Thus, the components experience temperature cycles in their usage life. Solder joint reliability (SJR) under thermal loading is an important topic for electronic packaging. Besides, for some products such as MEMS sensors, stress also leads to the shift in the output signals, leading to less satisfactory performance.

1.3.2 Moisture Related Problems

Moisture exhibits not only chemical but also mechanical effects on electronic packages. From the mechanical aspect, moisture can reduce the strength of some materials. Besides, volumetric expansion is associated with the absorption of moisture, which is referred to as hygroscopic swelling, resulting in stresses if different materials within the

structure exhibit different extents of expansion. The situation is worse when moisture is vaporized at high temperature. If an electronic package is to be soldered to the board by reflow soldering, which is common for SMT components, moisture sensitivity might be crucial. In a worst-case scenario, vapor pressure causes cracks and/or delamination with an audible sound. This phenomenon is referred to as popcorning (Figure 1-5).

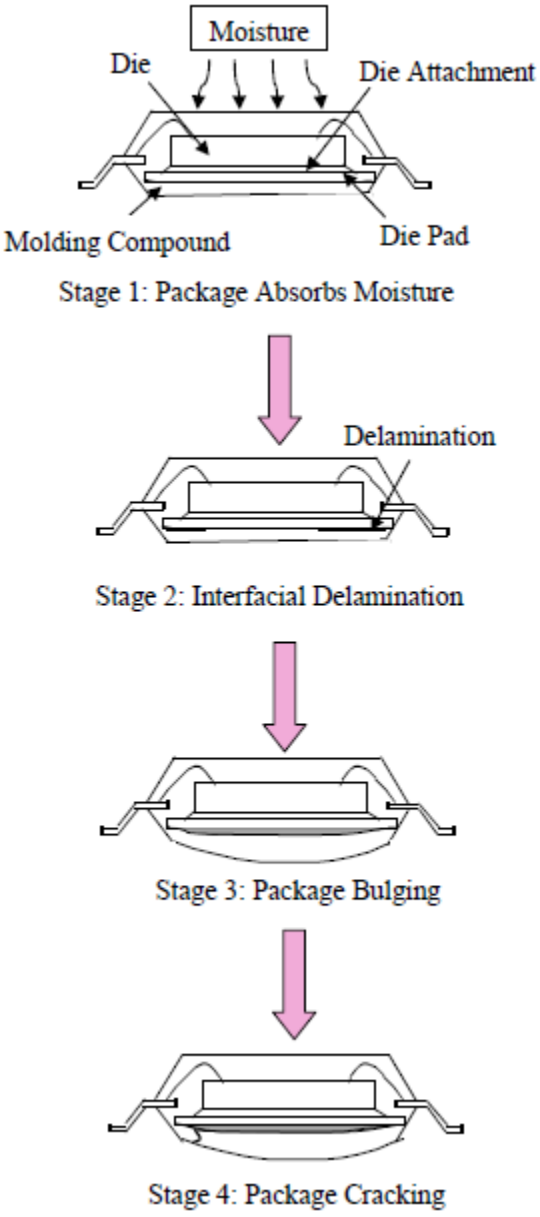

Figure 1-5 Popcorn Failure Caused by Moisture [13]

1.3.3 Electromigration

Electromigration is the transport of materials driven by the momentum transfer between the moving electrons and metal ions [14]. It can cause two failures: open circuit failure, caused by void formation, and short circuit failure, caused by unintended connection attributed to the piling up of conductive materials (i.e., whisker). Electromigration is mainly driven by the "electron wind force," which is the product of atomic density and the drift velocity of moving ions; however, it is also significantly related to the temperature gradient and mechanical stress gradient [15]. Therefore, modeling electromigration using numerical methods can be very complicated.

1.3.4 Thermal Management

The generation of heat is inevitable for electronic products. For ensuring device operation at desired temperatures and preventing failures caused by thermal issues, the heat has to be dissipated. Thermal performance can be improved by the design of chip, package, PCB, or system, selection of materials, and choice of appropriate heat dissipation techniques. Heat dissipation approaches such as heat sinks, fans, and liquid cooling methods have been widely employed. Currently, several commercial software packages, such as Flotherm and Icepak (part of ANSYS), can be utilized to perform thermal analysis of electronic components and systems. With the continuous increase in the density of electronic devices, the challenges in thermal management will be more critical.

1.3.5 Reliability under Shock or Vibration

Electronic components are exposed to vibration during manufacturing, transportation, and operation. Besides, these components may also be subjected to shock

impact caused by either harsh usage conditions or accidental drop. Impact and vibration reliability have become crucial requirements as automotive electronics and portable consumer electronics are widely utilized [16].

1.3.6 Combined Loading Conditions

Under real usage conditions, an electronic package simultaneously experiences thermal, mechanical, and moisture conditions. Therefore, it is necessary to investigate the effect of combined loadings on the stress and/or life of the components and assemblies. Such combinations include:

1) Vibration at different frequencies;

2) Thermal cycling with power cycling;

3) Thermal cycling with static mechanical loading;

4) Thermal cycling with vibration; and

5) Thermal and hygroscopic swelling.

Miner's damage rule has often been employed for predicting fatigue life; however, some researchers have found that for some cases, Miner's rule does not accurately predict fatigue life because the mechanism of failure under the combined loading condition becomes different [17], [18]. Some prediction models based on damage mechanics have been proposed for predicting fatigue life under such conditions [18]. Besides, prognostication techniques have also been developed [19].

1.4 Objective of This Research:

The objective of this study is to explore the behavior of underfill viscoelastic material exposed to several moisture exposure and characterize the viscoelastic parameter using dynamic mechanical analyzer and stress relaxation test. After that, determine the

effects of viscoelastic parameters on reliability prediction using finite element analysis (FEA). Another polymeric solder mask material mechanical properties has been explored through UV and thermal curing. The following objectives will be achieved in this research:

1. Mechanical characterization of underfill material exposed to different moisture conditions based on JEDEC standard. Stress–strain and creep behavior were investigated in 3 different moisture level for up to 60 days of moisture exposure.
2. Developed correlation between mechanical properties change with moisture content absorbed by underfill material
3. Viscoelastic Prony series parameters were measured through DMA and Stress relaxation test. Based on the Prony parameter stress-strain and creep data were predicted and correlated with experimental result.
4. Prony parameters were used in BGA packages and predicted the thermal cycling reliability of solder joint using finite element analysis.
5. Investigated the mechanical properties of commercially available solder mask material by changing UV and thermal curing. A optimum UV curing time has been determined for better properties and variation of mechanical properties changes were measured.

1.5 Organization of the Dissertation:

This dissertation focuses on understanding the polymeric material behavior based on thermal and moisture effects and is presented in the following chapters:

Chapter 1: Introduction to microelectronic packaging polymers, flip chip packaging.

Chapter 2: Literature review on moisture effects on underfill, viscoelastic constitutive models and solder mask curing effects on microelectronic packaging polymers.

Chapter 3: Specimen preparation and Experimental setup

Chapter 4: Mechanical characterization of underfill material exposed to different moisture conditions.

Chapter 5: Characterization of Viscoelastic Response of Underfill.

Chapter 6: Thermal cycling analysis of underfilled BGA assemblies using FEA simulation.

Chapter 7: Mechanical characterization of solder mask material.

Chapter 8: Summary and conclusions of the dissertation

CHAPTER 2

LITERATURE REVIEW

2.1 Introduction

Various polymeric materials are used in electronic packaging. Underfill materials are applied to redistribute the residual stress in the solder layer of the flip-chip package, epoxy molding compounds (EMC) are used as a protection layer for the IC and die; solder mask are used to resist the solder bridges between copper pads. Electrical behaviors must be correlated with other performance necessities, such as protection from environment, resistance to drop, shock, vibration and temperature effects. To become ideal candidates for microelectronics packaging, polymers need to have excellent adhesion to many surfaces, low dielectric constant, thermal property, ease of processing. Most polymers are epoxy based and they exhibit time and temperature dependent mechanical response (viscoelasticity). Several failures take place in the polymeric material. As epoxy based material prone to absorb moisture, moisture induced failures are common in microelectronic packaging. Also, to predict the correct modeling approach using finite element analysis (FEA), determine the correct viscoelastic parameter is very important. Unfortunately, these material property data are not available from vendor datasheets. These parameters can be determined several ways and it is important to correctly estimate these parameters. Also curing behavior of polymers also important to get the better mechanical property. UV curing and thermal curing are important for getting the better behavior.

2.2 Fabrication and Characterization of Polymer

To perform experiment on polymers, representative uniaxial test samples need to prepare. Feustal et al [11] prepared large bulk strip samples using a molding procedure, however, due to large size, it is obvious that curing will be non-uniform. In that way, it won't provide same mechanical response as of actual flip chip underfill layers. A new technique shown by Qian et al [20] in which 0.5 mm thick samples were prepared in a metal mold which was cured according to vendor recommended profile. In this a release agent was used which changed the surface of the underfill samples. Dynamic mechanical analyzer (DMA) was used to characterize stress-strain curves, storage and loss moduli determination in a dogbone shaped underfill sample [21]. Islam and co-workers [22]–[24] developed a unique procedure to prepare 90 x 3 mm samples. In the processing method, the liquid underfill was dispensed between Teflon coated plates and cured using production equipment. Same processing conditions were also used in actual flip chip assemblies. The extracted tensile samples (region between the specimen grips) was 60 x 3 mm, which providing a highly desirable aspect ratio of 20. Due to the capillary action of underfill, it can evenly distributed between the Teflon molds. To observe the nonlinear stress strain behavior over a range of temperatures and strain rates, a three parameter hyperbolic tangent empirical model had been shown.

The mechanical characterization of polymer materials are very important to get higher reliable product. Curing of an underfill has strong effect on mechanical behavior. A through study have been performed using DSC (Differential Scanning Calorimeter), DMA, TMA (Temperature Mechanical Analyzer) and TGA (Thermal Gravimetric

Analyzer) to get information on kinetics and viscoelasticity of underfill [25]. Residual stresses in underfilled plastic packages were studied by Sham and Kim [26].

2.3 Effects of Moisture on Material Properties

Many failures in microelectronics packages can be drawn back to moisture [27], [28]. The mechanical behavior of polymer material is affected significantly by the absorption of moisture [29]–[34]. Normally, three types of failure mechanisms take place when an electronic package is exposed to humidity conditions [34]. The first type failure is referred as "popcorn failure"[30]–[33]. Microelectronic devices are exposed to moisture after opening up from protective dry bag for surface mounting to printed circuit board (PCB). Environmental moisture enters into the polymeric materials and it condenses in free volumes or micro/ nano pores in the bulk materials and along interfaces. During the surface mount process, condensed moisture will vaporize and produce high pressure. In the reflow oven, the peak temperature ranges typically between 220 ^{o}C to 260 ^{o}C and reflow process is completed within a few minutes. Polymeric materials are extremely affected when temperature goes beyond glass transition temperature. As interfacial adhesion strength drops, delamination occur due to the combined effects of hygroscopic stresses, thermo mechanical stresses, vapor pressure, material softening and adhesion degradation. An audible sound may be created due to suddenly release of water vapor in times of package cracking. Second type of moisture induced failure mechanism concerns the package reliability during long term service in various field environmental conditions. After absorbing moisture polymeric materials in package will swell. This is called hygroscopic swelling. Due to swelling, dimensional changes take place which create hygroscopic stresses. For a long period of humid environment, delamination may take

place along the weaker interfaces. There are a number of experimental techniques for the characterization of hygroscopic swelling of polymers [35]–[41]. To address this issue, a silicon/underfill/FR-4 assembly was tested [39]. Through this study, the hygroscopic swelling behavior of underfill material in a flip chip assembly was investigated. The third type of moisture induced failure is electrochemical migration (corrosion) in the presence of both electrical bias and moisture. Two kinds of corrosion take place in electronic packages. One kind of corrosion is metal dendritic growth at the cathode side on the substrate surface (e.g. copper trace). The second kind of corrosion is called conductive anodic filament (CAF) growth which occurs at the sub surface associated with glass fibers/epoxy resin interface. During the moisture exposure, the CAF grows from anode to cathode along the interfaces.

The physical and chemical interactions of humidity with polymers lead to physical, mechanical and, in many times, chemical changes of the polymers. Cure kinetics of underfill, thermal and mechanical analysis were reported in this work [25]. Several state of the art underfills flow and cure behavior were studied [42], future progress, process capability, advantages and disadvantages were also discussed. Several researchers have been investigated on environmental exposures e.g. molding compounds (encapsulants) and underfills. Adsorption of moisture in polymers can create major failures for plastic packaging as it. Differential Scanning calorimetry (DSC) was used to characterize the moisture uptake and related cure kinetics [43]. Moisture preconditioning strongly influenced the interfacial adhesion, reduce strength by 50% for underfill/solder mask interfaces after 725 hours of 85 ^{o}C and 85% RH moisture exposure [44]. They have also showed the elastic modulus variation at different moisture conditions for short period of

time (168 hours of exposure). Moisture related degradation for long term exposure is not available in literature. Chhanda et al.[45], [46], showed the moisture exposure variation at 85 C and 85 % RH. The changes in mechanical behavior were recorded for various durations of hygrothermal exposure.

Moisture has influence on fracture toughness/adhesion strength. To measure the behavior, a double cantilever beam specimen structure has been used to determine the interfacial fracture toughness [34]. Fracture toughness decreases after moisture preconditioning at 85ºC/85% RH for 5 days. The result is showed in the Figure 2-1

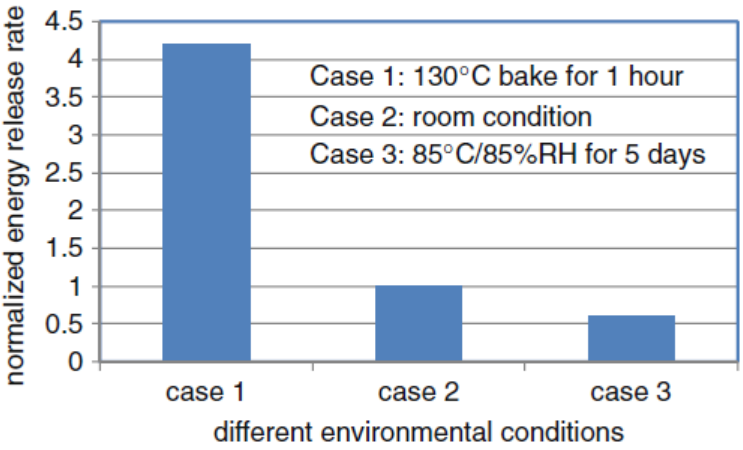

Figure 2-1 Fracture toughness for a Si/UF/Si assembly under different enviromental condition [34]

Moisture also has strong influence on die shear adhesion strength at an elevated temperature. Ferguson and Qu studied on the effect of moisture on the interfacial toughness of no-flow underfills. Four point bending testing was performed between bilayer underfill-solder mask/PCB specimens with prefabricated interface cracks to measure the interfacial fracture toughness [44]. There were dramatic reductions in the interfacial strength of the underfill/solder mask interface in lap shear specimens exposed to a combined humidity-temperature exposure were studied by Kuo et al [47]. Long term

exposure to humidity-temperature exposures (85 ^{o}C and 85% RH for 168 hours) were shown to have long term effects on the elastic modulus of the samples once the existing conditions of the specimens were all equilibrated by dry baking. However, interfacial toughness was lowered with duration and severity of the moisture exposure, including exposure to 85C with no moisture [48]–[50]. Luo and Wong found that interfacial strength in mechanical test specimens degraded with duration of combine thermal/humidity aging at 85 ^{o}C and 85% RH [51]. Crack opening displacements to quantity the deviations in stress intensity factors at an interfacial crack along an underfill and silicon chip passivation interface was characterized by Zhang in both dry and moisture aging [39].

Hygroscopic properties are necessary to perform moisture related simulation. A real time characterization of moisture absorption and desorption was done by Yi He [52]. A number of study has been performed to find moisture diffusivity (D), saturated concentration (C_{sat}) and Coefficient of Moisture Expansion (β) [32], [52]–[57]. Moisture behavior is dominated by diffusion of water which is believed to be constant (Fickian diffusion).

2.4 Viscoelastic Modeling of Underfill Materials

The viscoelasticity modeling of polymeric material is given in the Figure 2-2 [58]. The flowchart for viscoelasticity modeling are given in the following:

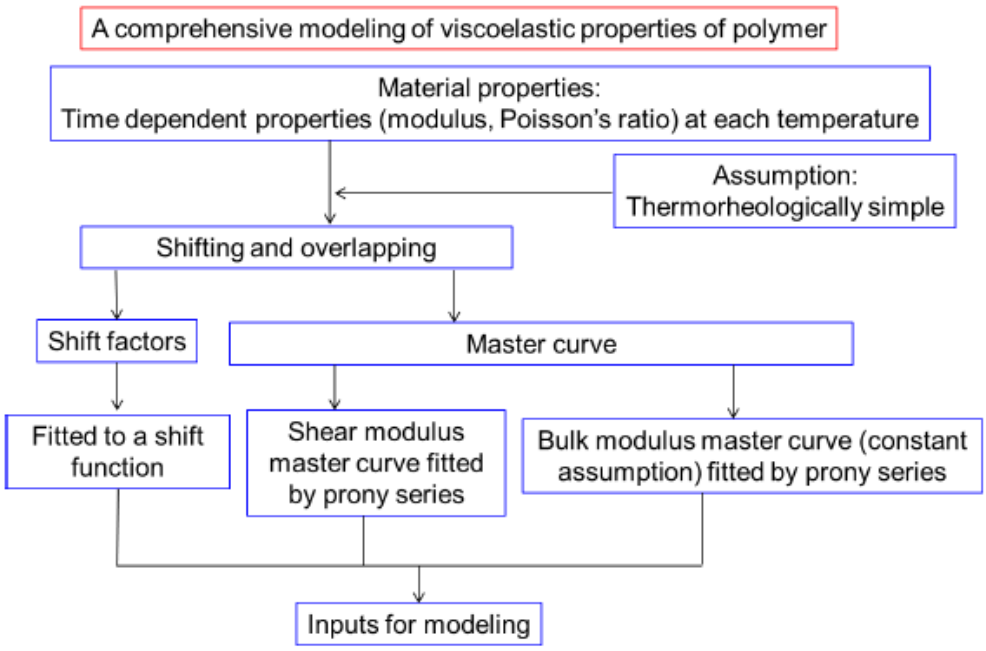

Figure 2-2 Flowchart for viscoelasticity modeling [58]

By adopting the assumption of thermorheologically simple (TRS) [59], which denoted that all relaxation times have the same temperature dependence. Due to the molecular transitions, each of them shows a temperature dependence. Relaxation times happened due to specific move all depend in the same way on temperature. Therefore it leads to an equal acceleration for each relaxation time for the particular move. By assuming material shows only one active move or transition, it became like thermorheologically simple. According to that, the spectrum of times will only shift along the time-axis. The shape of the spectrum, and the deformation characteristics related to the spectrum are unaffected. Another important assumption is the linear viscoelastic. This means that the model should be in the small strain range and the time dependent modulus should be independent of the applied stress. If the stress level is large enough, the linear viscoelastic assumption will no longer be valid [60], [61]

Several studies have been performed toward viscoelastic characterization of polymers. A series of experiments was performed by Popelar and Liechti [62] to evaluated and characterize the nonlinear behavior of epoxy. They determined 12^{th} order expansion for shear modulus function, and 9^{th} order expansion for the bulk modulus function. The developed linear viscoelastic model was extended to account for the nonlinear behavior of adhesive. The proposed model could capture nonlinear response in pure shear, and for shear with various amounts of superimposed tension and compression. Chen et al [63] investigated the thermal cycling of the package using both experimental testing and 2D finite element simulations. They considered 3 different material models to describe the mechanical response of the underfill. These included: (a) constant elastic model; (b) elastic model with temperature dependent modulus; and CTE (c) viscoelastic model. The results showed that the use of underfill encapsulant increased the thermal fatigue lifetime of solder joints. Using the finite element analysis, reliability and mechanical performance of the electronic package were studied [63][64]. According to the findings, an elastic model for the underfill caused thermal stress and strain level in the solder joints to be miscalculated significantly. Additionally, the stress concentrations in the underfill fillet in the die corner were provided overestimated value relative the viscoelastic model. So, it is essential to consider the viscoelastic nature of the underfill to accurately predict the failure of solder joints and lifetime of the package. Thompson, et al. built a finite element model of flip chip and applied viscoelastic model incorporated in ANSYS to see the mechanical behavior of underfill polymers [65].

Liu et al. [66] described that the viscoelasticity of PCB materials affects the dynamic nature of the board. Mottahedi et al. [67] investigated that the unknown Prony

coefficients can be measured by performing relaxation test and they conducted numerical analysis of relaxation test based on Prony series material. Fernanda et al.[68] has determined viscoelastic parameters directly from frequency domain experimental data and they also described to characterized the intrinsic evolution of storage modulus, loss modulus by using DMA with frequency. A dynamic frequency sweep test can be performed which contains two parts of the storage modulus and the loss modulus. Hongging et al. [69] performed test to find Prony coefficients using the generalized Maxwell model with the help of dynamic modulus time curves. Park et al. [70] have stated an efficient method of fitting Prony series models to viscoelastic experimental data with power law pre-smoothing which is important when the data have significant variance.

Stress relaxation experiments were performed on molding compound to find the master curve and a Prony series expansion of 21st order was used to express the material's relaxation behavior [71] (Figure 2-3.)

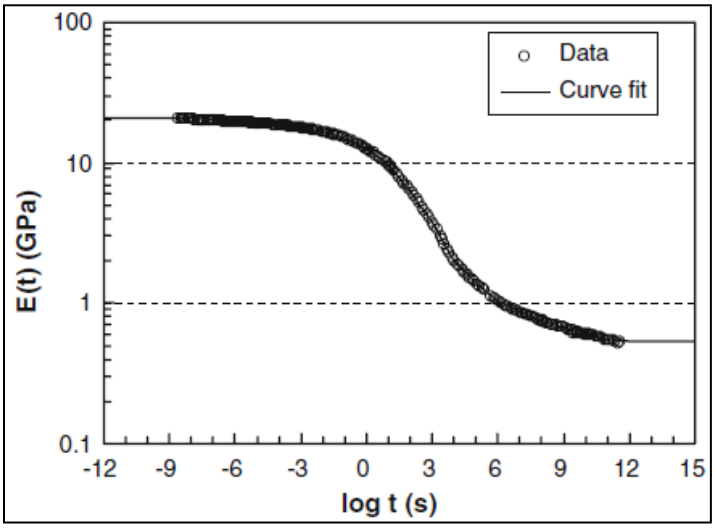

Figure 2-3 Master Curve Generated by Shifting the Relaxation moduli [71]

The Prony coefficients were determined for two reference temperatures and two methods were used to carry out the curve fitting to determine the Prony pairs and shift factors. Yi he [72] performed Dynamic mechanical analyzer (DMA) time-temperature superposition (TTS) experiment between 30 ^{o}C and 150 ^{o}C with the frequency scanned between 0.05 and 50 Hz. A horizontal and vertical shift factors were determined based on the TTS results. Chhanda et al [73], [74] performed rate dependent stress strain testing over a wide temperature range and creep testing for a large range of applied stress levels and temperatures. They measured Prony series viscoelastic model which has been found to represent both stress strain and creep data well at all temperatures.

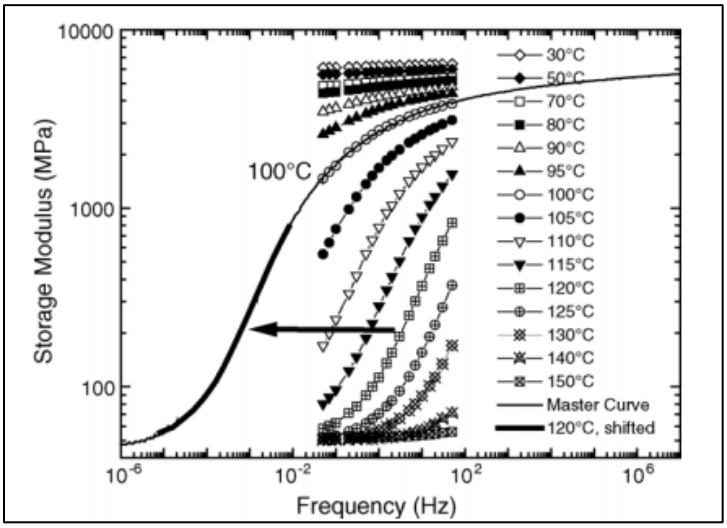

Figure 2-4 Master Curve Generation from DMA [72]

2.5 Effect of Viscoelastic Response on Thermal cycling Solder Joint Reliability

To evaluate the package reliability at early design stages, it is important to use simulation tools which provides faster, cheaper and more reliable electronic products. Based on the actual test data, proper constitutive modeling, dominant damage mechanism,

and appropriate simulation, solder joint life can be calculated. Most electronic packages undergo thermal and power cycling conditions throughout their service life. The root cause of most solder joints failures is CTE mismatch induced stresses/strains. Researchers have proposed several approaches to predict the life.

Syed [75] has used double power law and hyperbolic sine creep equations to predict the reliability of solder joints in BGA assemblies. He presented that failure criterial based on accumulated strains and dissipated energy density per cycle can provide good predictions of the measure life of solder joints. A volume average energy density method to predict the life of lead solder (63Sn37Pb) and SAC 405 solder joints was shown by Zahn [76]. Ridout et al [77] wrote a review where the methods of calculating solder cycles to failure were divided by three categories, analytical methods, combined constitutive law and fatigue methods, and damage mechanics methods.

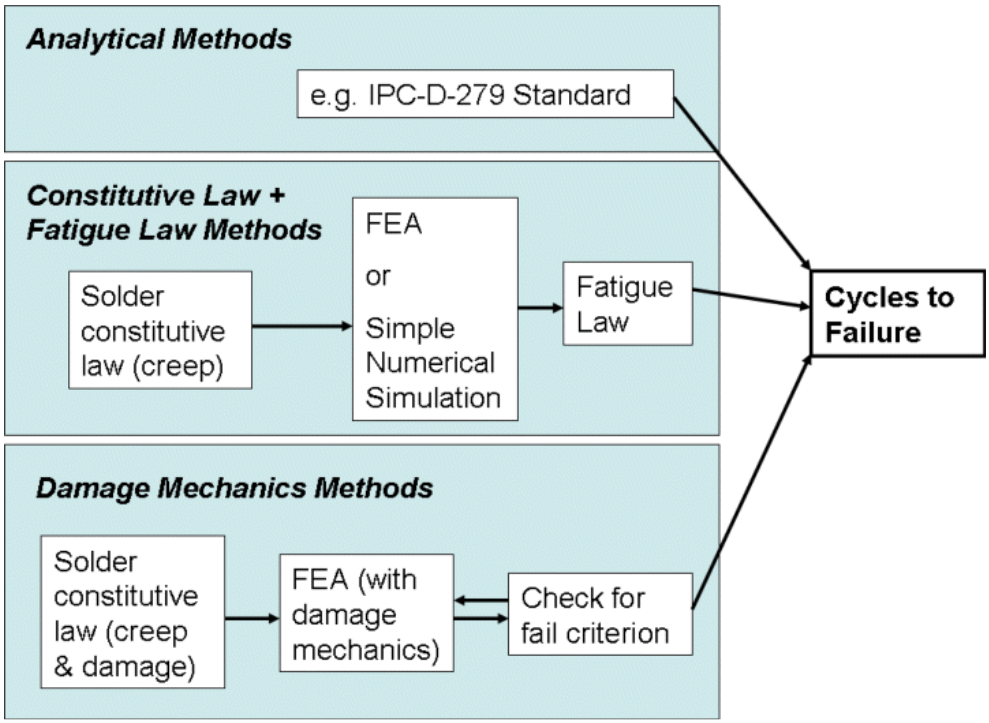

Figure 2-5 Modeling methods to calculate solder fatigue life [77]

Darveaux [78] has showed energy dissipation based models for crack initiation and crack growth rate in solder joints. These types of models have been subsequently used by many researchers for life prediction of the SnPb and SAC solders. Darveaux introduced four constants which can be found by curve fitting using the experimental failure data and energy dissipation per cycle can be found from FEA simulations.

2.6 Mechanical Behavior of Solder Mask

The mechanical behaviors of solder masks are poorly understood and can be critical factors for reliability of high density electronic assemblies. Michaelides and Sitaraman [79] introduced the reliability models that are based on the solder stiffness and other parameters. An integrated numerical and experimental approach in studying the effect of solder mask on the thermal fatigue life of solder joints can be found in the work of Schubert,

et al. [80]. The dependence of mechanical behavior on the temperature of solder masks and plastic packaging materials is investigated by Darveaux, Norton, and Carney [81].

It is also noted that FEM has been employed to analyze the warpage of solder masks (Ume, Martin, and Gatro) [82]. Zhu, et al. worked on several solder masks and showed the mechanical properties, creep response [83]. To produce reliable products, mechanical properties of solder mask are critically important. Among the all mechanical properties of solder mask, tensile properties and creep response are of particular concern.

Based on study, high temperature aging and moisture exposure to interconnect polymers has negative effect on their mechanical properties. Lin, et al. [84]–[86] showed that effective elastic modulus (E), ultimate tensile strength (UTS) increased with the amount of the isothermal aging or aging temperature, regardless of whether the aging temperature is below, at or above the T_g for viscoelastic material. Typically, E and UTS were increased in the range of 10-40% of the non-aged values. Aging was also found to dramatically decrease (100X) the secondary creep rate up to 6 months of aging before testing. Also, humidity exposure affects the property of this interconnect material and their property variation at different moisture condition was explored in detail [87], [88]. Moisture caused detrimental effect on mechanical properties, e.g. elastic modulus and creep behavior, and the overall property degradation is depending on amount of moisture absorbed by that material.

UV curing is a photochemical process in which high-intensity ultraviolet light is used to instantly cure adhesives. In this process, a certain percent of photoinitiators are mixed with adhesive resin. The photoinitiator reacts with adhesive resin when certain amount of UV light is delivered, and a chemical reaction take place and make the adhesive

harden better. Wavelength and intensity are two important characteristics for UV light exposure. Correct light and intensity is required for the photoinitiators to react properly, otherwise chemical reaction may not happen completely and outcome will be poor or inconsistent [89]. Ramli, et al. showed that UV curing time has optimum value in which better tensile strength can be obtained. Two other adhesives also showed similar behaviors [90].

Based on the above discussion, prior researchers have worked on the moisture effects on underfill, glass transition temperature and elastic modulus changes; viscoelastic modeling for underfill and polymers. In this work, underfill material was characterized based on several moisture exposure for longer period of time and evaluate the change of mechanical response based on the experimental test. Also, viscoelastic modeling was performed based on several experimental way and determined the coefficients needed for FEA simulation. After that, these coefficients were added as an input parameter for flip chip packages and determine the effect of viscoelastic response. Solder mask material was characterized based on several UV and thermal curing changes and also performed aging study. The Changes in mechanical property due to UV and thermal exposure were calculated and an optimum curing criteria was suggested based on the experimental test.

2.7 Summary

As discussed above, prior researchers have performed work on effects of moisture exposures on underfill viscoelastic materials. But, long term moisture exposure at several moisture sensitivity level data was not available. During the simulation process, these moisture degraded material properties data are very important to get the correct behavior.

In this work, long term moisture exposure mechanical degradation data was incorporated with moisture uptake in the samples. A correlation was trying to obtain in this study.

Viscoelastic material property data are not available from vendor datasheet. But, to perform a reliable study on semiconductor packaging, correct material modeling data needs to determine. A detailed step by step processing were performed for characterizing underfill viscoelastic behavior and Prony series material constants are evaluated. Based on the Prony pairs, a thermal cycling analysis was performed using Ansys to predict failure life time of solder joint.

Solder mask property data with various curing and aging result are not available in the literature. UV curing and thermal curing was needed in the processing of solder mask which have important effects on the material mechanical strength and reliability. A detailed study has been performed on commercially available solder mask material with varying UV and thermal curing condition. High temperature aging study was also performed.

CHAPTER 3

SPECIMEN PREPARATION AND EXPERIMENTAL SETUP

3.1 Introduction

Consistent and wide-ranging material property data are needed for microelectronics encapsulants for the determination of mechanical design, reliability assessment, and process optimization of electronic packages. Since, the vast majority of contemporary underfills used are epoxy based, they have the propensity to absorb moisture, which can lead to undesirable reductions in their mechanical and adhesion properties.

In this chapter, a unique preparation procedure of specimen is presented. This approach can produce micro-scale uniaxial specimens without further modification and machining. The polymers include commercially available BGA/CSP underfill material from Namics Corporation (Namics U8410-73A). For dynamic mechanical analyzer (DMA) test, Namics U8410-99 was used.

The preparation procedure for tensile testing and DMA testing is quite different. For tensile and creep testing, the final dimension has been maintained as 90 x 3 x 0.125 mm. Uniaxial tensile and creep tests were then carried out by using a micro tension torsion testing system. Stress relaxation tests also performed at different temperature using the same testing system. DMA has been used to study viscoelastic modeling for underfill. For moisture exposure experiments, the specimens were exposed to controlled humidity using programmable Tenney temperature/humidity chambers. An electronics scale has been used to monitor weight gain of specimen after moisture absorption. JEOL JSM-7000F Field Emission SEM machine was used to determine the filler particle size in the underfill samples.

3.2 Specimen Preparation Procedure

3.2.1 Underfill

In this study, free standing underfill samples for mechanical testing were prepared using the procedure discussed in references [87], [88]. A stacked assembly view of the "mold assembly" utilized in this investigation is pictured in Figure 3-1 (a), and Figure 3-1 (b) shows example uniaxial specimens after curing. The various parts of the assembly are clamped together by removable end clips (not shown). The middle layer consists of precision shims with a thickness (usually of 0.5 mm (20 mils) or 125 μm (5 mils)) defines the sample thickness. Usually the thickness is chosen depending on the typical thickness for BGA underfills in application. The molds are made from stainless steel and are coated with a thin Teflon® layer on all surfaces. The top portion of the mold assembly has been machined to contain 9 rectangular crossbars (80 x 3 mm) with a constant separation via the remaining steel material at the ends of the crossbars. The shims separating the two plates are only present under the front and rear "connecting regions" of the steel sheet, and not under the crossbars themselves. The mold assemblies were preheated to 112 ^{o}C, and underfill encapsulant was dispensed along one side of each steel crossbar via a production line programmable dispense system (CAM/ALOT 3700 shown in Figure 3-2).

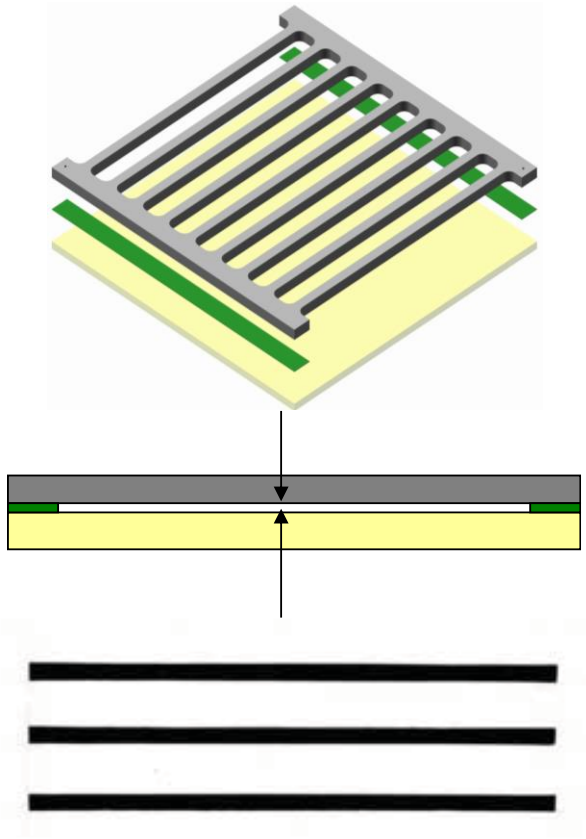

Figure 3-1 (a) Mold Assembly for Underfill (b) Underfill Test Specimens

Figure 3-2 Specimen Preparation Machine and Mold Assembly

Fuducial markings are included on the top of the steel sheet to aid in the programmability and repeatability of the dispense procedure. After dispensing, the underfill encapsulant quickly ran under the gap under each crossbar via capillary flow. This procedure produced a set of constant thickness 80 x 3 mm rectangular underfill regions, which were sandwiched between the Teflon® coated top and bottom "mold plates". The uncured mold assemblies were then cured in a box oven (Figure 3-3) using the vendor recommended underfill cure profile. Due to the Teflon® coatings, the uniform thickness cured rectangular samples were easily separated from the mold. A razor blade and fine SiC paper were used to trim any unevenness from the ends of the samples. In the described method, the samples have a controllable constant thickness, and are easily removed from the mold assembly without the aid of chemical release agents. The lengths of the final trimmed samples (see Figure 3-1 (b)) were typically in the range of 70-90 mm, giving a specimen length to width aspect ratio of more than 20.

Figure 3-3 Box Oven for Curing

3.2.2 Solder Mask

The solder mask samples were made using both UV curing and thermal curing. The commercially available solder mask utilized in this work with a glass transition temperature of 104.8 ^{o}C. For making a tensile sample, at first 100 parts weight of PSR-4000-AUS5 is mixed with 43 parts CA-40 AUS2. After thoroughly mixing of both substances, the solution was poured into a Teflon-coated mold assembly which was covered with foam tape. The tape was circulated on four sides of the mold such way that a 0.30 mm thickness was achieved. The figure is shown in below.

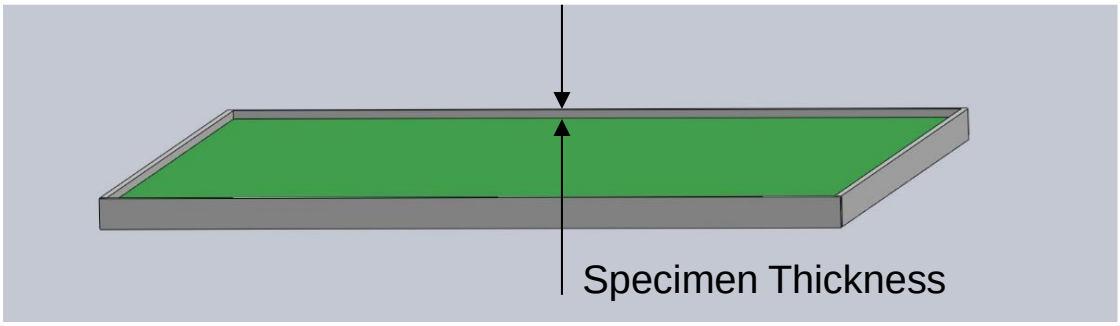

Figure 3-4 Mold Assembly for Sample Preparation

After that, solder mask poured into the cavity and it took the space with maintaining the desired thickness. Then, the whole assembly put into an UV oven. The UV oven used in this case is Dymax ECE 5000 (Figure 3-5).

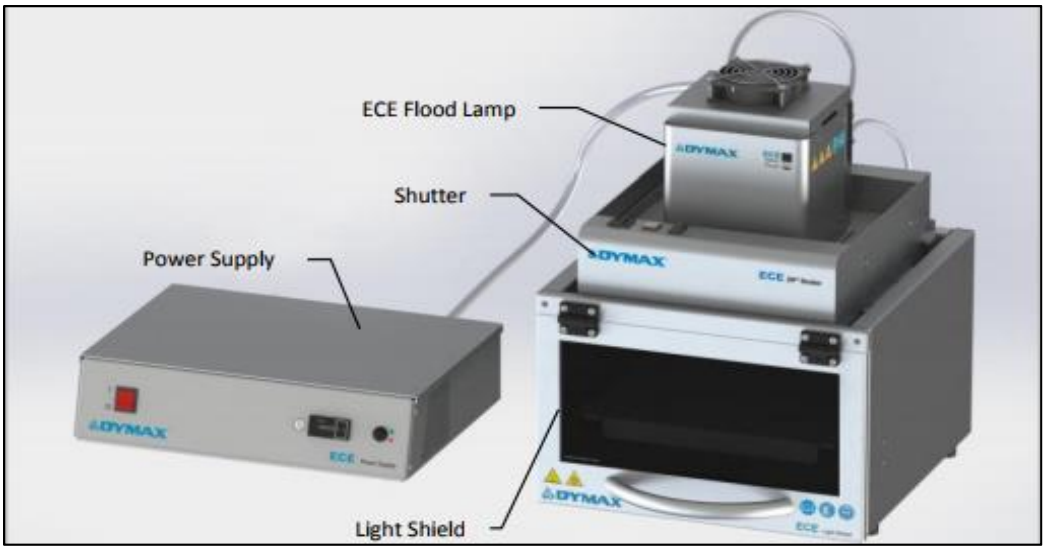

Figure 3-5 Typical UV Flood-Lamp System

Dymax UV light curing flood lamps are general purpose units for the curing of UV light curable adhesives, coating, and inks. They are extensively used for bonding, potting, sealing and encapsulating. This unit provides an effective curing area of approximately 5'' x 5'' (12.7 cm x 12.7 cm). In that way, it is ideal for small batch processing of UV adhesives and potting compounds. Typical initial output intensity at UV-A range is 225 mW/cm^2. UV exposed sample is shown in the Figure 3-6.

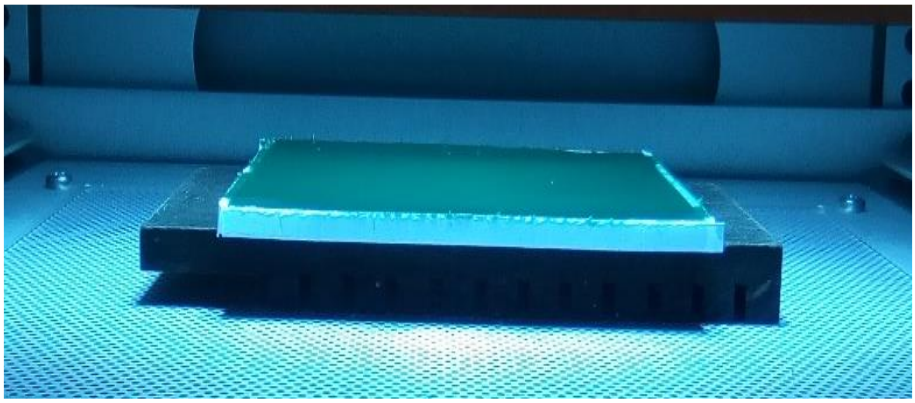

Figure 3-6 UV exposed Sample

After UV curing, solder mask was cured in a box oven at 140 ^{o}C for 60 minutes. Due to the Teflon coatings, the uniform thickness cured rectangular samples were easily separated from the mold. A sharp razor blade was used for cutting the samples to desired dimensions. In the described method, the samples have a controllable constant thickness and are easily removed from the mold assembly without the aid of chemical release agents. The lengths of the final trimmed samples (see Figure 3-7) were typically in the range of 70-90 mm, while the width was all 3 mm, giving a specimen length to width aspect ratio of more than 20. After having the desired dimension, the test specimens were ready for mechanical testing.

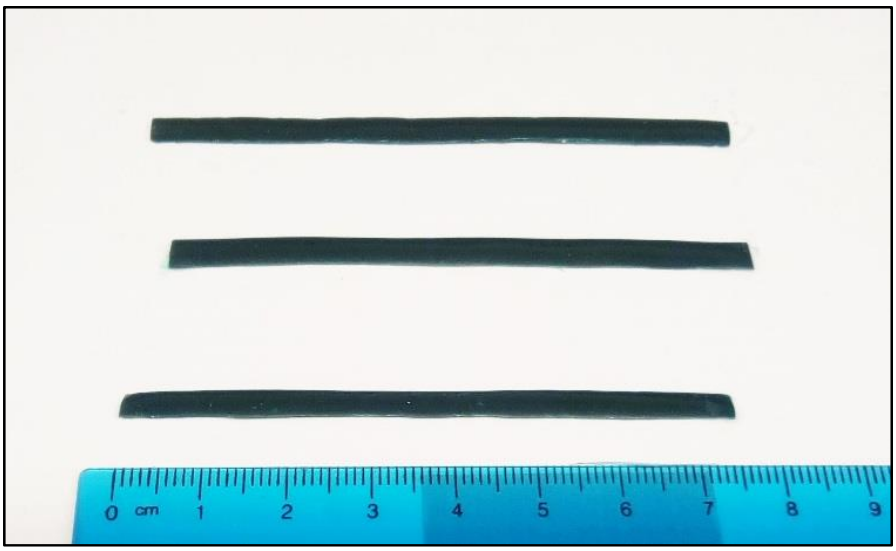

Figure 3-7 Test Specimens

3.3 Mechanical Testing System

In this study, a microscale tension/torsion thermo-mechanical test system from Wisdom Technology, Inc., as shown in Figure 3-8 has been utilized to load the samples.

The associated environmental chambers are shown in Figure 3-9 and Figure 3-10. The computer-controlled actuators provide an axial displacement resolution of 0.1 micron and a rotation resolution of 0.001 A^o. A universal 6-axis load cell was utilized to simultaneously monitor three forces and three moments/torques during sample mounting and testing. Testing can be performed in tension, shear, torsion, bending, and in combinations of these loadings, on small specimens such as thin films, solder joints, gold wire, fibers, etc. The hot and cold environmental chambers employ a resistance heater and liquid nitrogen diffuser to provide testing temperature ranges of +25 to +300 ^oC and -185 to +25 ^oC and, respectively.

During uniaxial testing, forces and displacements were measured. The axial stress and axial strain were calculated from the applied force and measured crosshead displacement using

$$\sigma = \frac{F}{A} \qquad \varepsilon = \frac{\Delta L}{L} = \frac{\delta}{L} \tag{3.1}$$

Where σ is the uniaxial stress, ε is the uniaxial strain, F is the measured uniaxial force, A is the original cross-sectional area, δ is the measured crosshead displacement, and L is the specimen gage length (initial length between the grips). For the tests in this study, stroke (displacement) control was utilized.

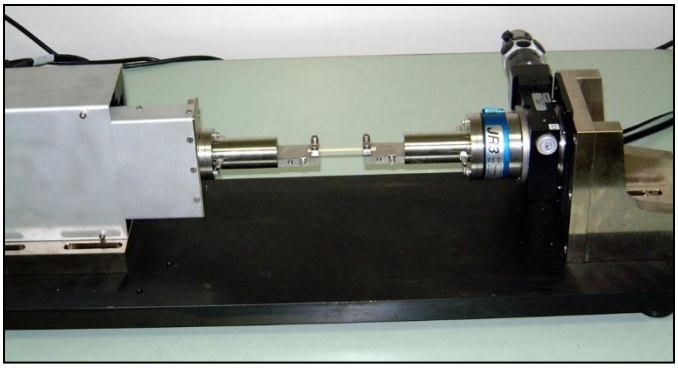

Figure 3-8 Testing System

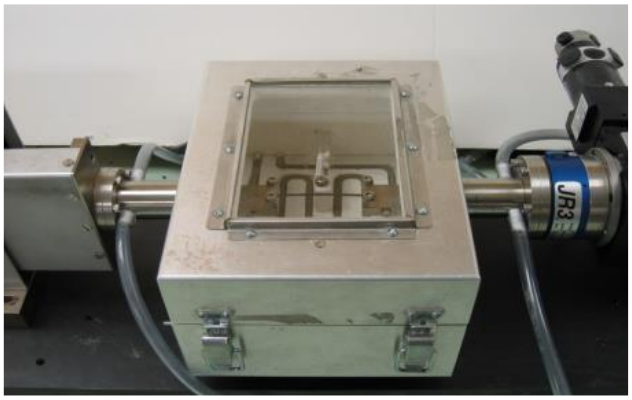

Figure 3-9 Chamber for Elevated Temperature Testing (+25 to +300 ^{o}C)

Figure 3-10 Chamber for Low Temperature Testing (-185 to +25 ^{o}C)

3.4 Typical Testing Data and Data Processing

3.4.1 Stress-Strain Curve

A typical recorded tensile stress strain curve for polymer with labeled standard material properties is shown in Figure 3-11. The notation "E" is taken to be the effective modulus, which is the initial slope of the stress-strain curve. The ultimate stress, σ_u is the maximum stress attained before failure and ε_f is the corresponding strain of ultimate stress.

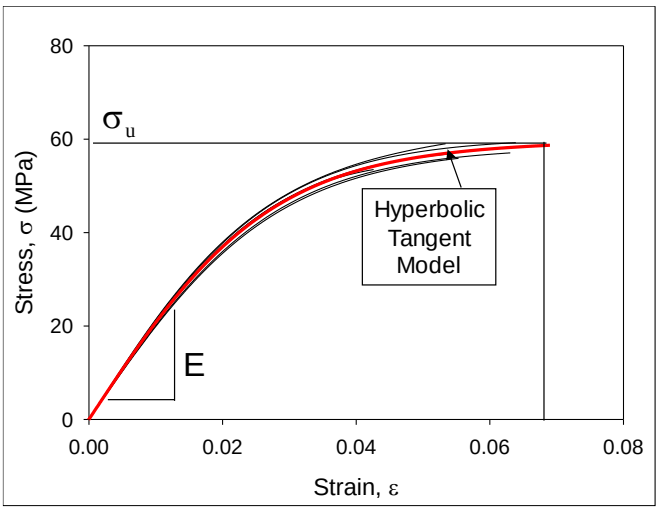

Figure 3-11 Typical Polymer Stress-Strain Curve and Material Properties

An empirical three-parameter hyperbolic tangent model has been used to accurately model the observed nonlinear stress-strain data at any temperature. The general representation of this relation is

$$\sigma(\varepsilon) = C_1 \tanh(C_2\varepsilon) + C_3\varepsilon \tag{3.2}$$

Here, C_1 and C_3 are in MPa but C_2 is unit less. All three are material constants. These are determined using a nonlinear regression fit of Equation 3.2 for a given set of experimental data. For example, the Figure 3-11 shows all hyperbolic tangent model fit to all experimental stress strain data at a fixed temperature. The variation in the data is very common for polymeric materials. Here, the red curve which is the hyperbolic tangent model fit gives a very nice representation of the experimental data. This data also lies in the middle of the curve which also shows a very excellent fit of the data. The accurate representation obtained using the hyperbolic tangent empirical model suggests that it provides a mathematical depiction of an appropriate average stress-strain curve for a set of experimental curves measured under fixed test conditions. Every data in this study is processed using this procedure. Total 6-10 experimental stress-stain curves were measured each time. After that, fit those curves using an average stress strain curve which gives the mathematical representation for all data.

When the strain is very small ($\varepsilon \rightarrow 0$), the effective modulus (E) can be estimated from the relation as:

$$\lim_{\varepsilon \to 0} \frac{d\sigma(\varepsilon)}{d\varepsilon} = \lim_{\varepsilon \to 0} C_1 C_2 \{(1 - \tanh^2(C_2 \varepsilon)) + C_3\}$$

$$= C_1 C_2 + C_3$$

Thus, the initial elastic modulus has been calculated from the three material constants which are shown as:

$$E = \sigma'(0) = C_1 C_2 + C_3 \tag{3.3}$$

3.4.2 Creep Test

In a typical creep curve (Figure 3-12), the initial "elastic" strain level is followed by regions of primary and secondary creep. A very long duration of nearly constant slope is referred as the secondary creep region. This steady creep rate is often used by engineers as one of the key material parameters in finite element simulations. The measured creep rates were taken to be the slope values at the end of the linear portion in the observed secondary creep regions.

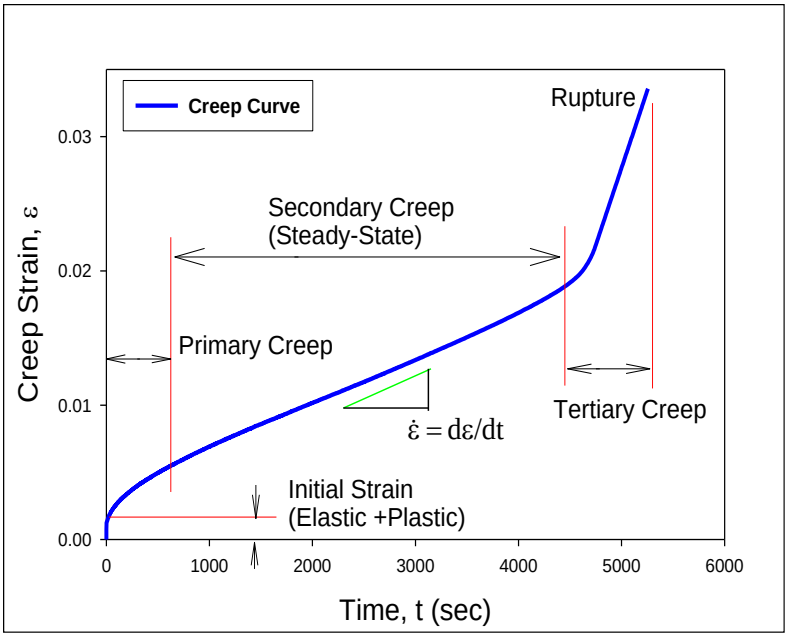

Figure 3-12 Typical Creep Curves

The load input of a creep test has been calculated as:

$$F = (\sigma \times w \times t \times 10^3) / g \tag{3.4}$$

where F is the input holding force in gram, σ is the applied stress level for the creep test in MPa, w is the specimen width in mm, t is the specimen thickness in mm, and g is the acceleration of gravity (9.8 m/sec^2).

In the creep experiments, constant stress levels on the order of 25-75% of the observed UTS have been applied. Due to the long testing time involved, only 3 specimens have been tested for each set of condition. The curves in each set were fitted with an empirical strain-time model to generate an "average" representation of the creep response for those conditions. For the range of test conditions considered in this work, the raw strain versus time data in the primary and secondary creep regions were found to be well fitted by an empirical Log Hyperbolic Tangent model (see Figure 3-13):

$$\varepsilon_{cr} = C_1 \ln(1+t) + C_2 \tanh(C_3 t) + C_4 t \tag{3.5}$$

Constant C_4 is the long-term (steady state) creep rate in the secondary creep region. Constants C_1 and C_2 are parameters used to describe the nonlinear response in the primary creep region. From the recorded strain vs. time curves under constant stress, the "steady state" creep strain rates have been extracted.

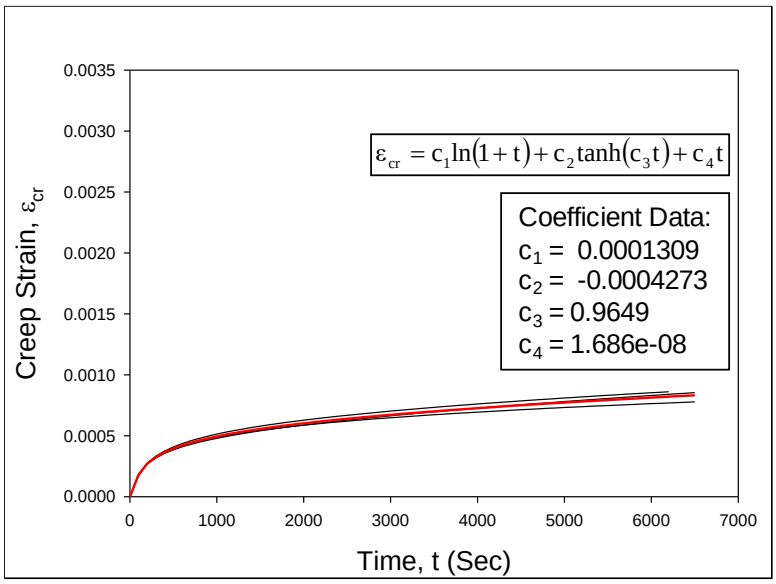

Figure 3-13 Creep Curve and Log Hyperbolic Tangent Model Fit

3.4.3 Stress Relaxation Test

Stress relaxation test was performed in a micro tension torsion tester machine which is shown in Figure 3-8. In the time of testing, force and displacements were measured and axial stress and axial strain were found out using the following equation

$$\sigma = \frac{F}{A} \qquad \varepsilon = \frac{\Delta L}{L} = \frac{\delta}{L} \tag{3.6}$$

where σ is the uniaxial stress, ε is the uniaxial strain, F is the measured uniaxial force, A is the original cross-sectional area, δ is the measured crosshead displacement, and L is the specimen gage length (initial length between the grips).

In this study, machine's stroke (displacement) was measured and using the uniaxial tensile samples, the stress-strain and creep responses for solder mask samples were measured at various temperature. 60 mm gage length was used between the machine grips.

The stress relaxation study has been conducted on underfill material specimens at 100, 110, 120, 130, and 140 ^{o}C. Stress relaxation experiment has been performed at ε = 0.01 i.e. 1%. The stress relaxation test data were shown below (Figure 3-15 - Figure 3-18).

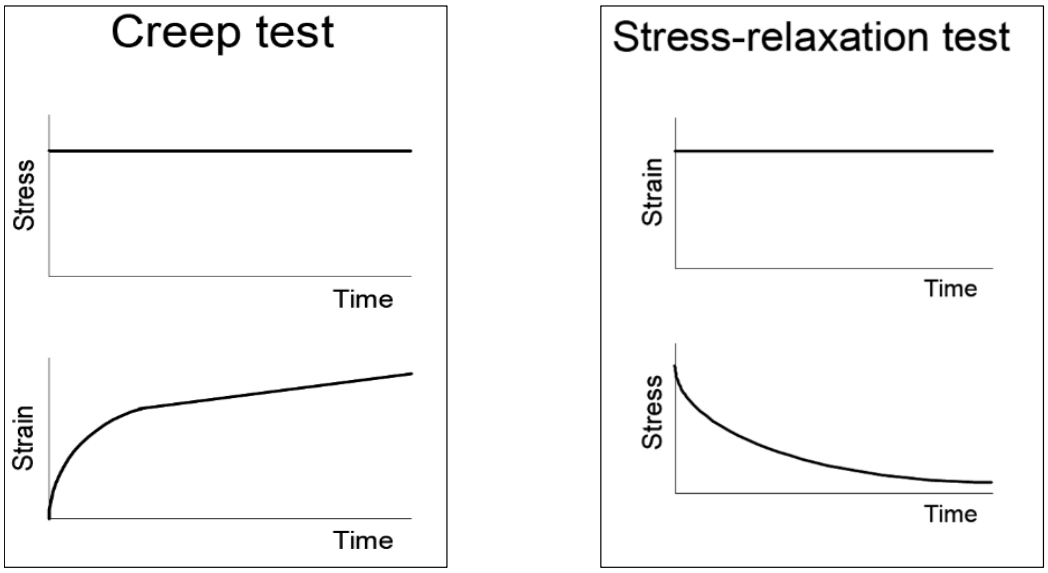

Figure 3-14 Difference between Creep test and Stress relaxation test

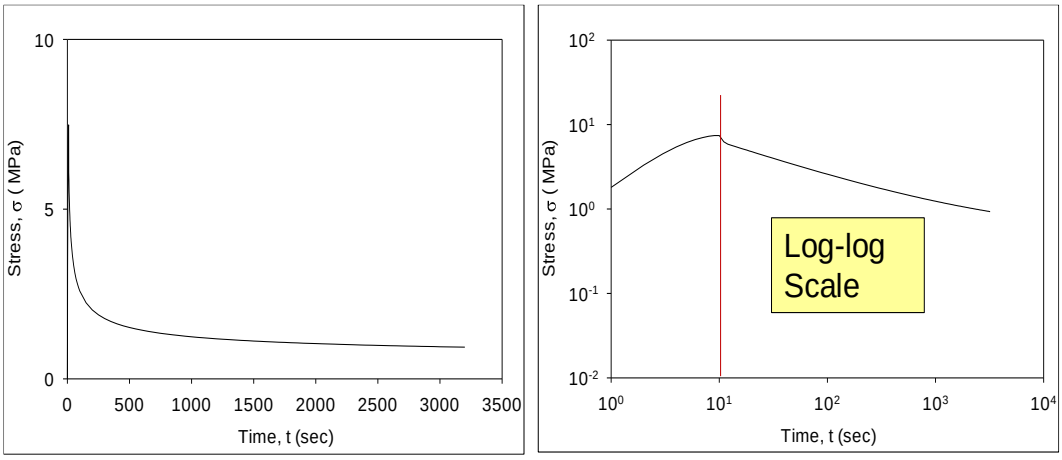

Figure 3-15 Stress Relaxation Test (Stress vs Time)

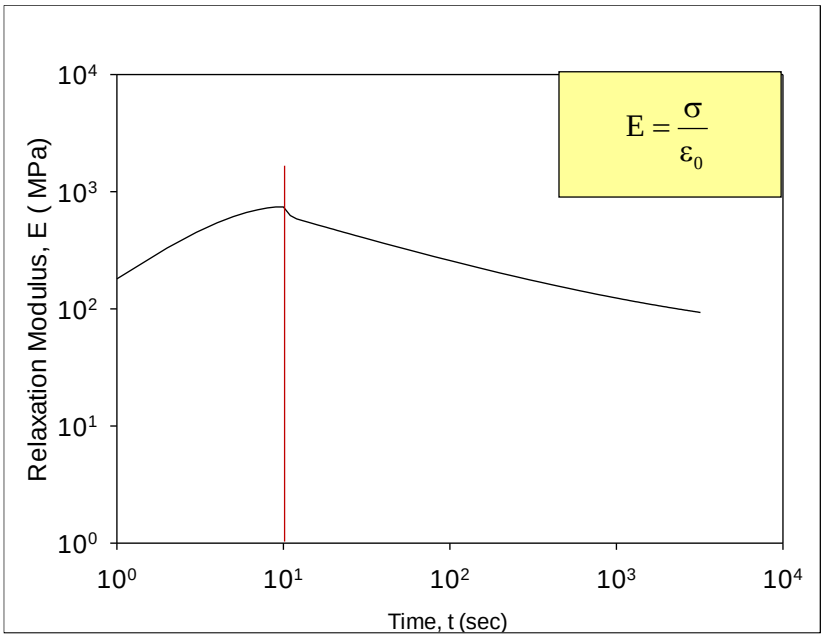

Figure 3-16 Relaxation Modulus vs Time

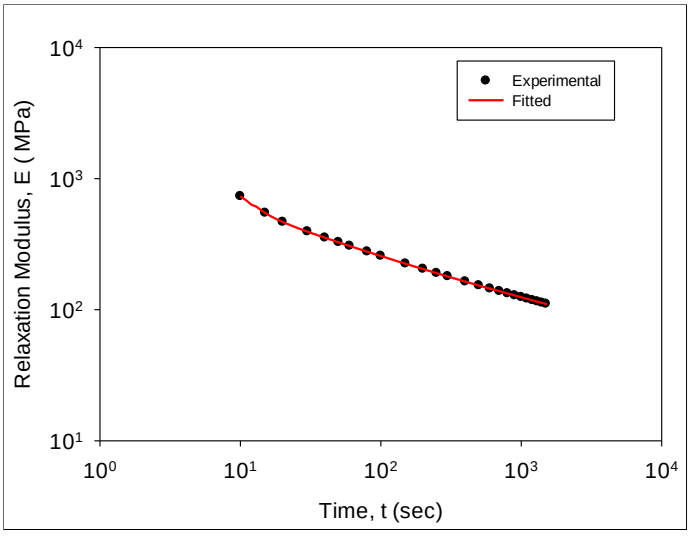

Figure 3-17 Fitted Experimental data

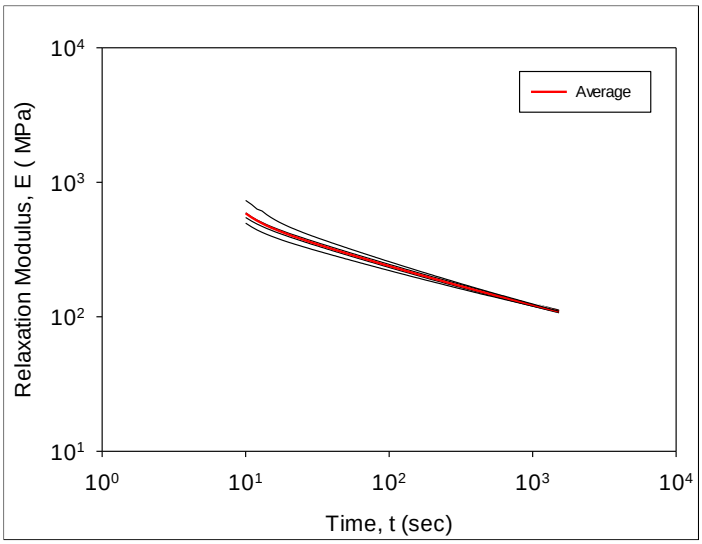

Figure 3-18 Average Curve for Relaxation Modulus

3.5 Dynamic Mechanical Analysis (DMA)

In this experiment a commercially available underfill material has been used to perform the dynamic mechanical analysis (DMA), stress-strain and creep experiments. Dynamic mechanical properties of the cured material were determined between 60 to 160 ^{o}C. The time-temperature superposition (TTS) experiments were performed using a TA Instruments RSA3 DMA system (Figure 3-19), which is operated in tensile mode. The sample were shown in Figure 3-20. The frequency sweep/temperature step test method was used which was shown in Figure 3-21. During the experiment, sample temperature was increased stepwise from 60 to 160 ^{o}C, with a step of 5 ^{o}C. A typical DMA test was shown in Figure 3-22. At each isothermal temperature, the frequency f was scanned over three decades between 0.1 and 10 Hz with a total of 8 discrete frequencies, which were: 0.1, 0.5, 1, 1.5, 2, 3, 5, 10 Hz. These frequencies were selected so that they were

approximately equally spaced on the logarithmic scale. The sample size was kept at 20 mm, and the typical sample width was 3 mm, with a thickness of 0.125 mm (5 mils).

Figure 3-19 TA Instruments RSA3 DMA System

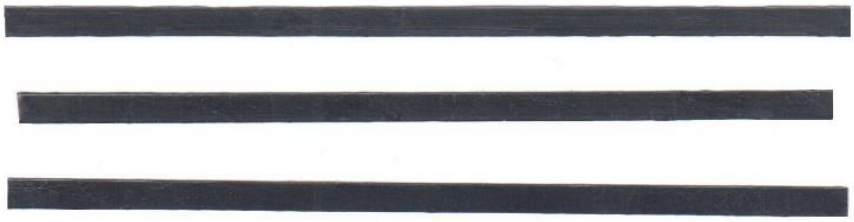

Figure 3-20 Test Specimens

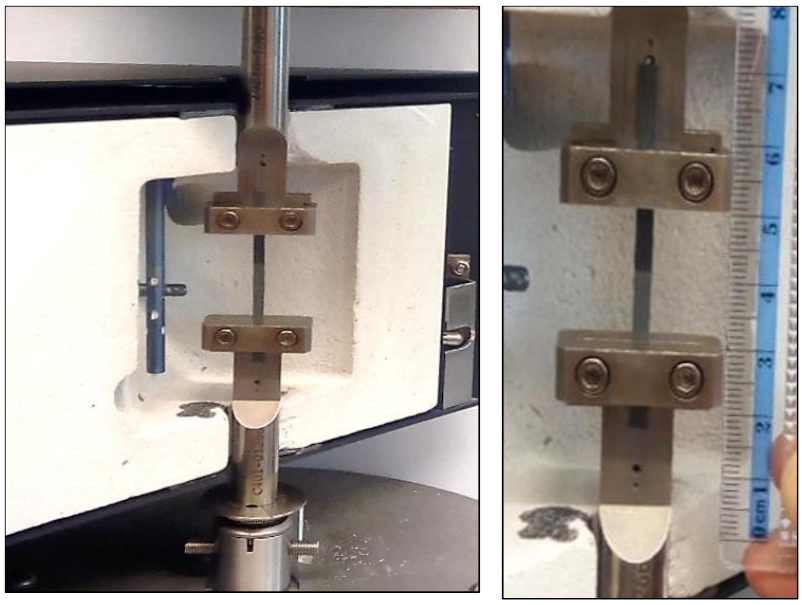

Figure 3-21 Frequency Sweep / Temperature Step Test

The DMA technique measures the stress strain relationship for a viscoelastic material. A real and imaginary component of modulus can be obtained by resolving the stress-strain components:

$$E^* = E' + iE'' \tag{3.7}$$

Where E* is complex dynamic modulus E' is storage modulus, E'' is loss modulus and i is the imaginary unit which satisfies the equation $i^2 = -1$.

Storage modulus refers to the energy stored elastically during deformation. It is related to elastic modulus of solids.

$$E' = \frac{\sigma_0}{\varepsilon_0}\cos\delta \tag{3.8}$$

Loss modulus is the energy converted to heat during deformation.

$$E'' = \frac{\sigma_0}{\varepsilon_0} \sin \delta \tag{3.9}$$

Loss tangent (tanδ)

$$\tan \delta = \frac{E''}{E'} \tag{3.10}$$

σ_0 and ε_0 are the amplitudes of stress and strain and δ is phase lag between applied stress and measured strain.

From the measured spectra of the moduli, the master curves were constructed by shifting the isothermal curves horizontally with respect to an arbitrarily selected reference temperature along the frequency axis.

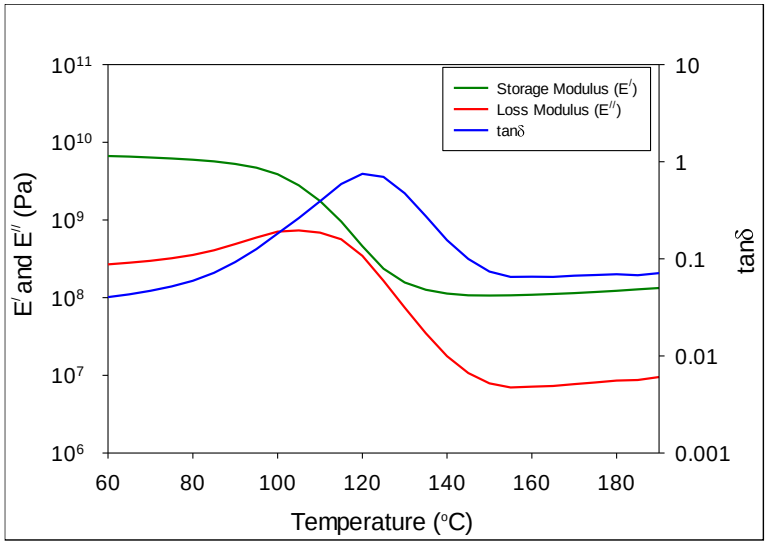

Figure 3-22 Testing Performed at frequency 1 Hz

3.6 Environmental Test Chamber

To study the effect of moisture uptake on the mechanical properties of microelectronic packaging polymers, the specimens have been exposed to controlled humidly. For this purpose, programmable Tenney (shown in Figure 3-23) were utilized. Besides having a wide range of controllable temperature, these chambers have humidification capabilities. The uniaxial test specimens have been exposed in these adjustable chambers to combined hygrothermal exposures for various durations and the effects of moisture adsorption on the stress-strain behavior were evaluated experimentally. The fabricated and preconditioned uniaxial test specimens were then exposed to moisture for various durations (0, 1, 3, 10, 20, 30, 60 days) in an environmental chamber using three different sets of hygrothermal conditions including 85 ^{o}C and 85 % RH (MSL 1, Moisture Sensitivity Level 1); 85 ^{o}C and 60 % RH (MSL 2); and 30 ^{o}C and 60 % RH (MSL 3).

Figure 3-23 Humidity Chambers Used for Moisture Exposure

3.7 Electronic Balance

The mass of the sample was measured by a high precision electronic sale that reads to the nearest 0.1 mg (Figure 3-24). The mass change during the time the samples were taken out of the humidity chamber was neglected.

Figure 3-24 High Precision Electronic Scale

3.8 Microstructural Study

Scanning Electron Microscope (SEM), as shown in Figure 3-25, has been applied to examine the filler particle size in the underfill samples. By scanning the sample with a focused beam of electrons, SEM can be used to produce images with high resolving power and high depth of focus. There are various signals that result from the interactions of the electron beam with the sample atoms, including secondary electrons (SE), back-scattered electrons (BSE), photons of characteristic X-rays, etc. Figure 3-26 shows the various depths of the produced signals within the sample [91] [92].

Figure 3-25 JEOL JSM-7000F Field Emission SEM

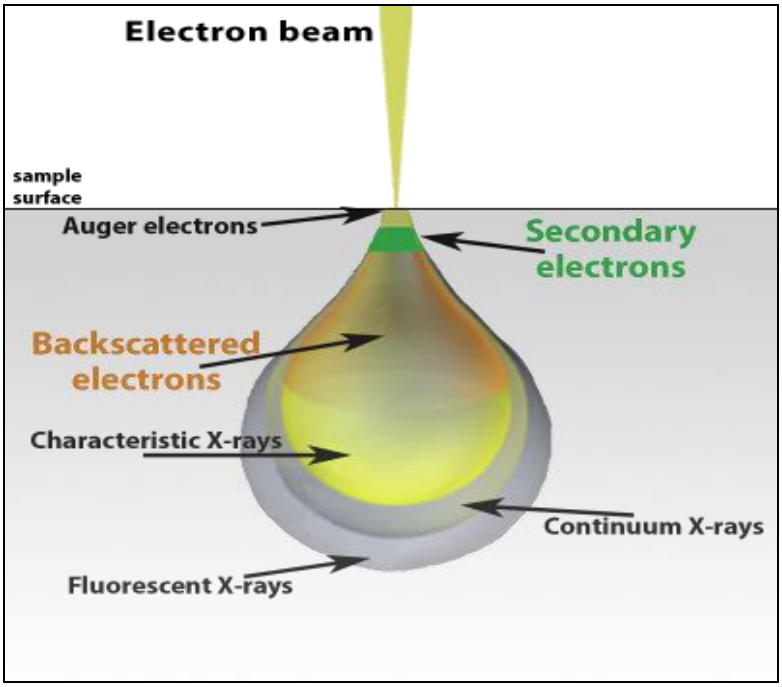

Figure 3-26 Various Signals at Different Depths within the Sample [91]

3.9 Summary

A unique specimen preparation procedure has been utilized in this study to prepare uniaxial tensile, creep and stress relaxation samples. Stainless steel molds which are coated with Teflon have been used to in this process. Using this technique, uniaxial samples with varying thickness samples can be made. By changing the shims, thickness can be controlled as required. Solder mask samples were made in the stainless steel mold by creating a cavity using a tape. A double-sided tape used in the four sides of the molds and thickness is maintained. In this process, significant number of samples can be made from each curing process.

CHAPTER 4

EXPERIMENTAL CHARACTERIZATION OF UNDERFILL MATERIALS EXPOSED TO DIFFERENT MOISTURE CONDITIONS

4.1 Introduction

Consistent and wide-ranging material property data are needed for microelectronics encapsulants for the determination of mechanical design, reliability assessment, and process optimization of electronic packages. Since, the vast majority of underfills used are epoxy based, they have the propensity to absorb moisture, which can lead to undesirable reductions in their mechanical and adhesion properties.

In this study, the effects of moisture absorption on the stress-strain and creep behavior of an underfill encapsulant were evaluated experimentally. The material behavior changes have been characterized using 60 x 3 x 0.5 mm uniaxial test specimens that were cured with production equipment using the same conditions as those used in actual flip chip assembly. After curing, the samples were separated into 2 groups and subjected to various preconditioning: (1) no preconditioning, (2) prebaking at 85 ^{o}C for 24 hours. The fabricated and preconditioned uniaxial test specimens were then exposed to moisture for various durations (0, 1, 3, 10, 20, 30, 60 days) in an environmental chamber using three different sets of hygrothermal conditions including 85 ^{o}C and 85 % RH (MSL 1, Moisture Sensitivity Level 1); 85 ^{o}C and 60 % RH (MSL 2); and 30 ^{o}C and 60 % RH (MSL 3).

After the moisture exposures, a microscale tension-torsion testing machine was used to measure the room temperature stress-strain behavior of the material. In addition, the viscoelastic mechanical responses of the underfill encapsulant after the moisture exposures were also characterized via creep testing for a large range of applied stress levels.

From the recorded results, it was found that the moisture exposures degrade the mechanical properties of the tested underfill including the effective elastic modulus, ultimate tensile stress, and tensile creep rate. Pre-baking was found to increase the initial material properties before moisture exposure, but the degradations due to subsequent moisture exposures occurred in an analogous manner. The moisture absorption into the underfill samples was also characterized by weight gain measurements for up to 60 days of exposure at the three different MSL conditions. From the results, it has been shown that maximum water weight gain in the material is about 1%. The results also showed that mechanical properties were only dependent on amount of water that has been absorbed by the material, regardless of how rapidly it was absorbed.

4.2 Theoretical Background

Fickian transport of moisture in polymers or polymer composites is defined by the following equation:

$$\frac{\partial C}{\partial t} = D\left(\frac{\partial^2 C}{\partial x^2} + \frac{\partial^2 C}{\partial y^2} + \frac{\partial^2 C}{\partial z^2}\right) \tag{4.1}$$

This equation is known as the general diffusion law or Fick's second law of diffusion (Fick's law), where C (kg/m^3) is the moisture concentration, t (s) is time, and D (m^2/s) is the diffusion coefficient or diffusivity (diffusion constant) of the moisture in the material. The temperature dependency of the diffusion constant can be defined by the Boltzmann–Arrhenius type of equation:

$$D = D_0 \exp\left(-\frac{E_d}{kT}\right) \tag{4.2}$$

where D_0 is a pre-factor, E_d is the activation energy, $k = 1.38 \times 10^{-23}$ J/K is the Boltzmann's constant, and T is the absolute temperature. Note that the pre-factor D_0 and the activation energy E_d are different below and above the glass transition temperature. In other words, there exist two sets of constants D_0 and E_d for a material to fully describe the moisture diffusivity in it as a function of temperature.

Consider a one-dimensional case of an infinite plate of thickness h. The common analytical solution, giving the temporal and spatial moisture concentration, C, at time t and the distance x from the mid-plane, can be achieved

$$\frac{C(x,t)-C_0}{C_i-C_0} = 1-\frac{4}{\pi}\sum_{n=0}^{\infty}\frac{(-1)^n}{(2n+1)}\exp\left[-\frac{(2n+1)^2\pi^2 D}{h^2}t\right].\cos\frac{(2n+1)\pi}{h}x \tag{4.3}$$

for the initial and boundary conditions,

$C = C_0$, $-h/2<x<h/c$, $t=0$,

$C = C_i$, $x= -h/2$, $x=h/c$, $t\geq 0$,

where C_i is the moisture concentration on the boundary, C_0 is the initial moisture concentration, D is the Fickian diffusion coefficient, and h is the thickness of the plate. Supposing the plate is originally dry and then located into a humid situation, $C_0 = 0$ and $C_i = C_{sat}$ (the saturated moisture concentration), and the equation above can be rewritten as

$$C(x,t) = C_{sat}\left[1 - \frac{4}{\pi}\sum_{n=0}^{\infty}\frac{(-1)^n}{(2n+1)}\exp\left[-\frac{(2n+1)^2\pi^2 D}{h^2}t\right].\cos\frac{(2n+1)\pi}{h}x\right] \tag{4.4}$$

and describes moisture absorption process as a function of time. With the time progressing, the plate will be fully saturated with a uniformly distributed moisture with the concentration C_{sat}. On the other hand, if $C_0 = C_{sat}$ and $C_i = 0$, the equation above yields

$$C(x,t) = C_{sat}\frac{4}{\pi}\sum_{n=0}^{\infty}\frac{(-1)^n}{(2n+1)}\exp\left[-\frac{(2n+1)^2\pi^2 D}{h^2}t\right].\cos\frac{(2n+1)\pi}{h}x \tag{4.5}$$

and describes a desorption process, in which an initially fully saturated plate releases moisture into the dry environment. The moisture in the plate will be driven out completely as time goes on.

Since it is not possible to measure the moisture concentration at an arbitrary inner point experimentally, the equation above should be incorporated over the thickness of the bulk plate so that it would be likely to measure at the plate exteriors the ratio of the transient moisture mass m(t) at a specified exposure time t to the moisture mass m_{sat} obtained in the completely saturated state as $t\rightarrow\infty$. The entire moisture mass in the sample can be acquired as a function of time as follows:

$$\frac{m(t)}{m_{sat}} = 1 - \frac{8}{\pi^2}\sum_{n=0}^{\infty}\frac{1}{(2n+1)^2}\exp\left[-\frac{(2n+1)^2\pi^2 D}{h^2}t\right] \tag{4.6}$$

4.3 Filler Morphology

The size distribution and filler morphology of this silica fillers were analyzed using by SEM. Figure 4-1 shows the SEM micrograph of filler distribution. SEM images clearly depict that all fillers are spherical in shape and largest filler particles are approximately 2.5 μm in diameter without any segregation which means small and larger fillers are randomly distributed throughout the sample. The smallest fillers are about 0.5 μm in diameter.

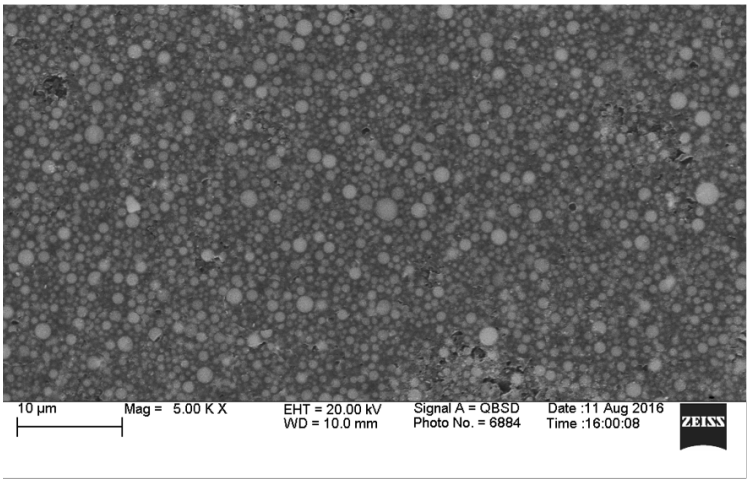

Figure 4-1 SEM Micrograph of Underfill Encapsulant

4.4 Stress – Strain Study

In our study [87], stress strain tests were done on normal underfill samples which were cured and cooled to room temperature. Experimental stress strain tests are shown in Figure 4-2. The average test results are shown in Figure 4-3. The second set of experiments were done on underfill samples that were prebaked for 85 ^{o}C for 24 hours after being prepared to remove all the ambient moisture in that sample. These results are shown in Figure 4-4 and Figure 4-5.

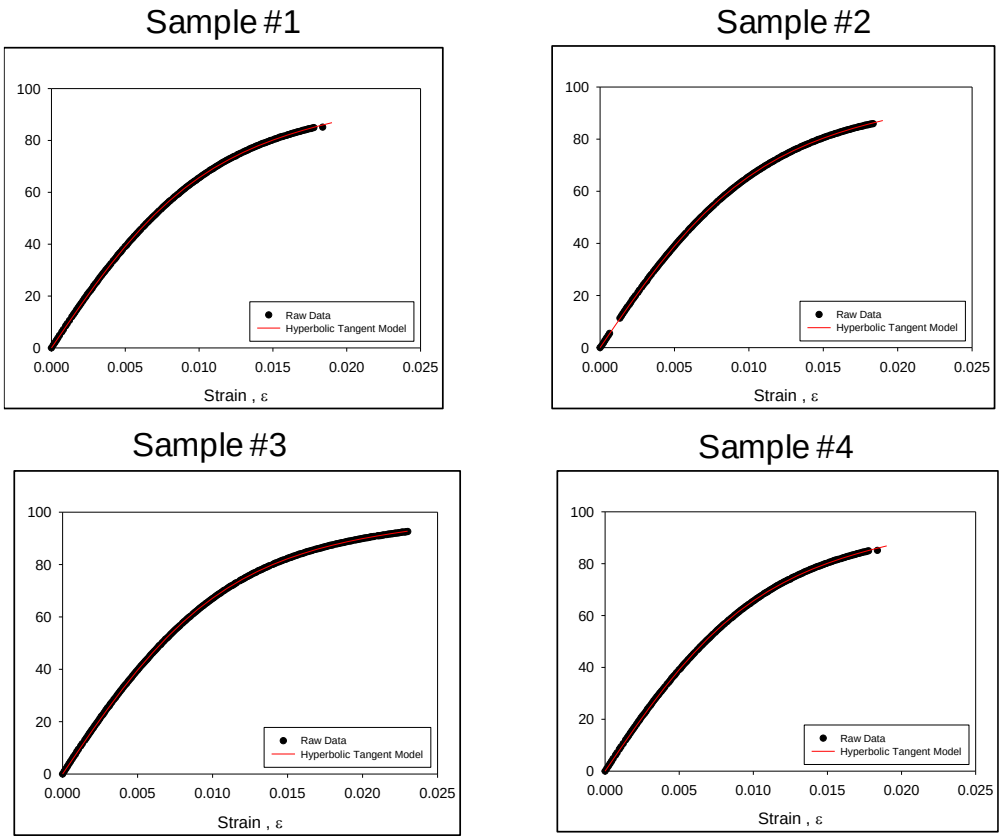

Figure 4-2 Experimental Stress- Strain Curve

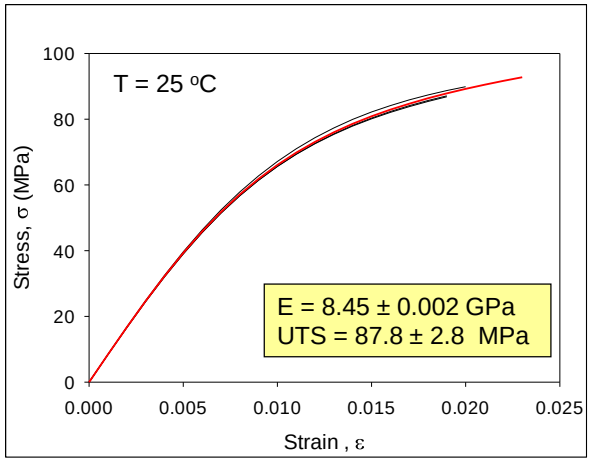

Figure 4-3 No Moisture Exposure, No Preconditioning

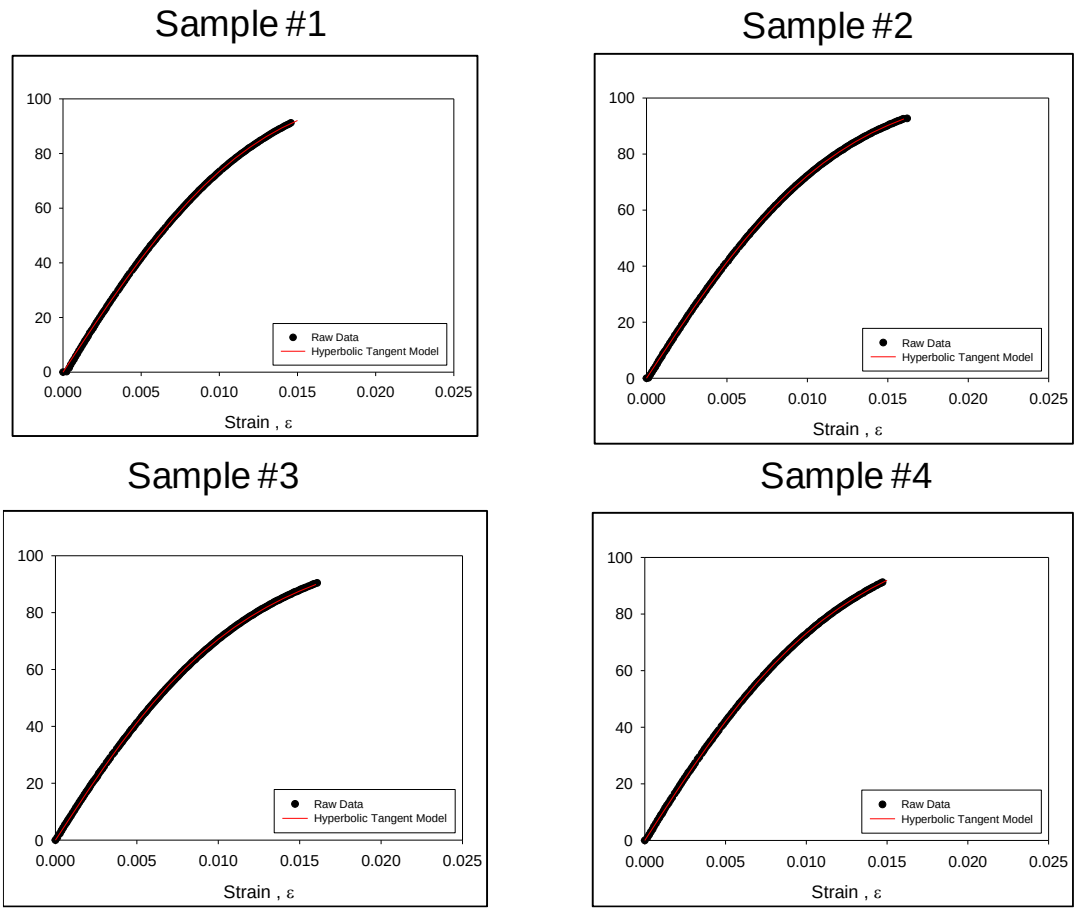

Figure 4-4 Experimental Stress- Strain Curve

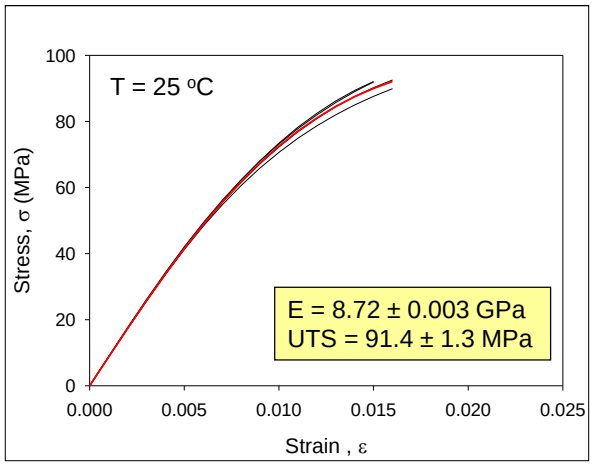

Figure 4-5 Stress-Strain Curves for Underfill (No Moisture Exposure, Preconditioned at 24 Hours at 85 oC)

The results showed the variations in the elastic modulus and Ultimate tensile strength (UTS). The initial elastic modulus increases from 8.45 GPa to 8.72 GPa which is about 3.2 % increase. The UTS also increased accordingly from 87.9 MPa to 91.4 MPa. Both results validate the thermal aging studies reported by Lin, et al. [85].

4.4.1 Moisture Exposure at 85 °C/85 % RH including Preconditioning

Underfill samples were tested at 85 °C and 85 % RH i.e. MSL 1 moisture condition after various durations of exposure. The no preconditioned samples were kept at MSL 1 conditions and tested after 0, 1, 3, 10, 30, 60 days of moisture exposure. No preconditioned 60 days moisture exposed stress strain results are given in the Figure 4-6. The prebaked samples also kept at MSL 1 condition and tested after the same exposure time. Example results for 60 days of moisture exposure are shown in Figure 4-7.

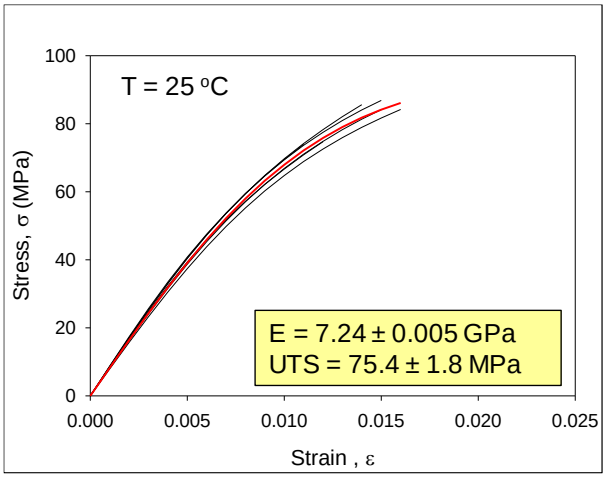

Figure 4-6 No preconditioning, 60 days of at MSL 1

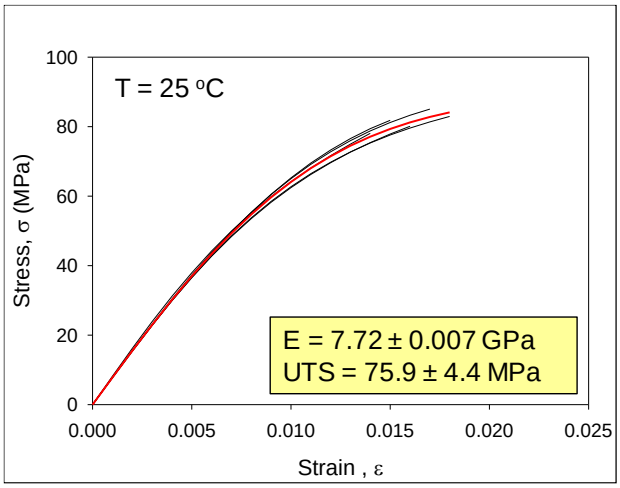

Figure 4-7 Preconditioned, 60 days of at MSL 1

Table 4-1 Material Property Variation (No Preconditioning)

Moisture Exposure (85 C, 85% RH)	Elastic Modulus E (GPa)	Ultimate Tensile Stress (MPa)	Ultimate Tensile Strain
None	8.45	87.9	0.0199
1 Day	7.90	78.2	0.0153
3 Days	7.49	77.7	0.0161
10 Days	7.31	77.2	0.0174
30 Days	7.29	76.9	0.0176
60 Days	7.24	75.4	0.0171

Table 4-2 Material Property Variation (Preconditioning for 24 Hours at 85 ^{o}C)

Moisture Exposure (85 C, 85% RH)	Elastic Modulus E (GPa)	Ultimate Tensile Stress (MPa)	Ultimate Tensile Strain
None	8.72	91.4	0.0154
1 Day	8.18	78.5	0.0143
3 Days	7.91	78.0	0.0144
10 Days	7.80	77.9	0.0159
30 Days	7.74	76.4	0.0151
60 Days	7.72	75.9	0.0155

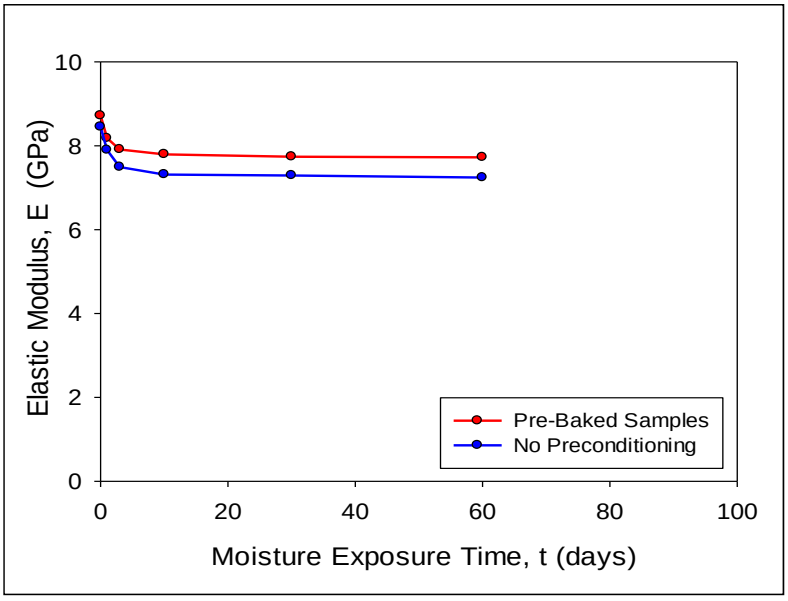

Figure 4-8 Variation of Initial Elastic Modulus with duration of Moisture Exposure

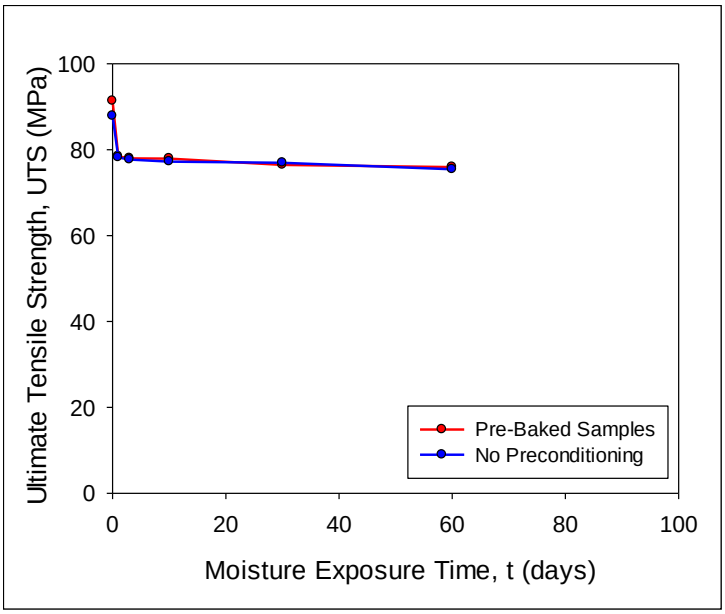

Figure 4-9 Variation of Ultimate Tensile Strength with duration of Moisture Exposure

The 0-day exposure results have already been presented in the last section (Figure 4-3 and Figure 4-5). Typical results for the samples experiencing moisture absorption are shown in Figure 4-6 and Figure 4-7 for the samples exposed to 85/85 conditions for the maximum duration of 60 days. Comparing the results, it can be observed that the mechanical properties degraded dramatically due to the moisture exposure. For the case of no preconditioning, the elastic modulus was reduced by 14.6% from 8.45 GPa to 7.25 GPa, and the UTS was reduced by 14.1% from 87.9 MPa to 75.5 MPa. Analogously, for the preconditioned (prebaked) case, the elastic modulus was reduced by 11.3% from 8.72 GPa to 7.73 GPa, and the UTS was reduced by 16.8% from 91.4 MPa to 76.0 MPa.

Analogous results were found for the other durations of moisture exposure. Table 4-1 and Table 4-2 contains a tabulation of the material properties as a function of the moisture exposure time and preconditioning. The variations of the initial elastic modulus and UTS with duration of moisture exposure are illustrated graphically in Figure 4-8 and Figure 4-9

respectively. Preconditioning had effects on the elastic modulus curves in Figure 4-8 for all durations of moisture exposure, while the UTS curves in Figure 4-9 were nearly identical after 1 day of moisture exposure.

4.4.2 Several Moisture Exposure

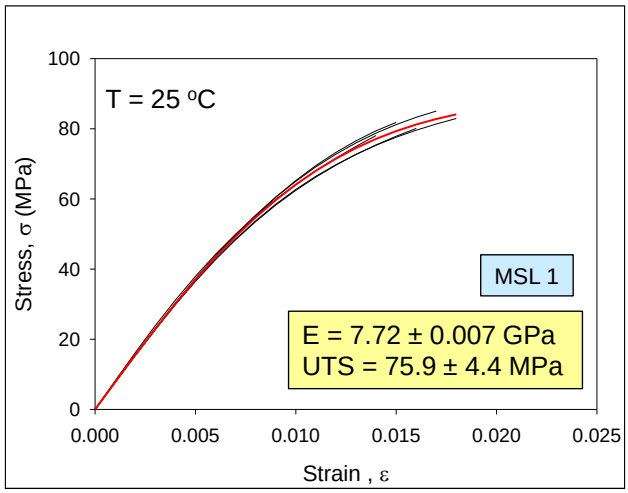

(a) Pre-Baked, Then 85 °C /85%RH (MSL 1) for 60 Days

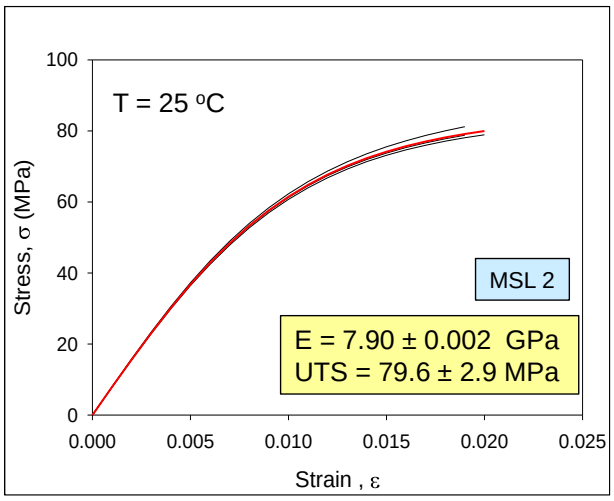

(b) Pre-Baked, Then 85 °C /60%RH (MSL 2) for 60 Days

Figure 4-10 Stress Strain Curves for 60 Days of Moisture Exposure

Tabulated results for the measured material properties as a function of moisture exposure level and exposure time are presented in Figures 8(a) and 8(b). The reductions in initial elastic modulus over the 60 day exposure were 12.8%, 9.4%, and 5.5% for MSL 1, MSL 2, and MSL 3 conditions, respectively. Similarly, the reductions in Ultimate Tensile Strength over the 60 day exposure were 16.9%, 12.9%, and 11.1% for MSL 1, MSL 2, and MSL 3 conditions, respectively. The initial elastic modulus and Ultimate Tensile Strength values tabulated in Table 4-3 are plotted versus exposure time in Figure 4-11 and Figure 4-12 respectively. As expected, the largest effects are seen for the MSL 1 exposures, and the results for MSL 2 and MSL 3 appear to parallel those for MSL 1.

Table 4-3 Material Property Variation with Moisture Exposure Conditions

(a) Elastic Modulus

Time	Elastic Modulus E (GPa) No Preconditioning MSL 1	Elastic Modulus E (GPa) Pre-Baked MSL 1	Elastic Modulus E (GPa) Pre-Baked MSL 2	Elastic Modulus E (GPa) Pre-Baked MSL 3
None	8.45	8.72	8.72	8.72
1 Day	7.90	8.18	8.41	8.53
3 Days	7.49	7.91	8.22	8.47
10 Days	7.31	7.80	8.14	8.29
30 Days	7.29	7.74	8.01	8.11
60 Days	7.24	7.72	7.90	8.09

(b) Ultimate Tensile Strength

Time	UTS (MPa) No Preconditioning MSL 1	UTS (MPa) Pre-Baked MSL 1	UTS (MPa) Pre-Baked MSL 2	UTS (MPa) Pre-Baked MSL 3
None	87.9	91.4	91.4	91.4
1 Day	78.2	78.5	85.3	87.1
3 Days	77.7	78.0	81.7	86.0
10 Days	77.2	77.9	80.9	84.3
30 Days	76.9	76.4	80.1	82.4
60 Days	75.4	75.9	79.6	81.3

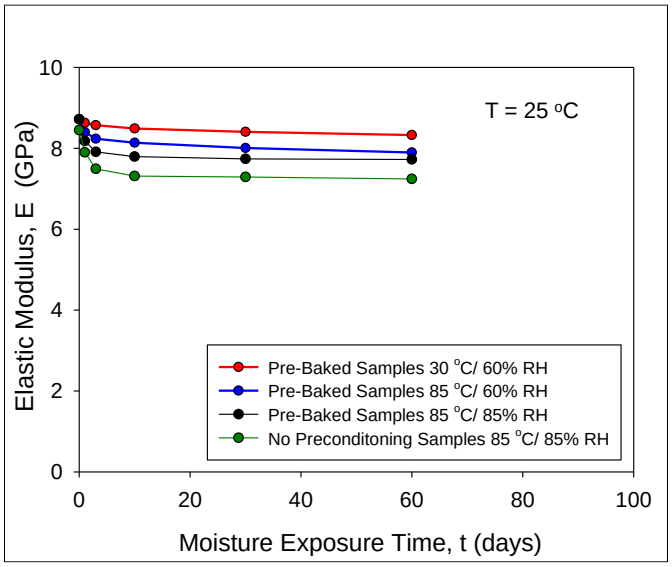

Figure 4-11 Elastic Modulus Variation with Moisture Exposure Time (85/85, 85/60, 30/60)

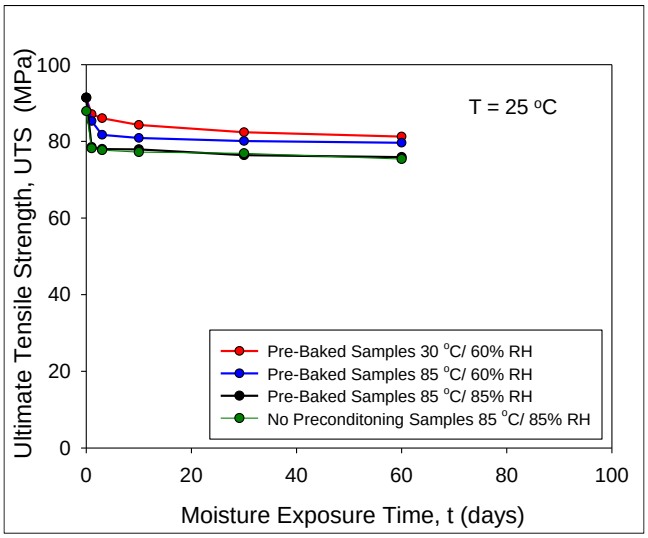

Figure 4-12 Ultimate Tensile Strength variation with Moisture Exposure Time (85/85, 85/60, 30/60)

4.5 Creep Study

The creep study has been conducted on underfill specimens with and without moisture exposure. For the creep experiments, we have tested the specimens after subjected to hygrothermal exposure at 85 °C / 85% RH (MSL 1), 85 °C / 60% RH (MSL 2) and 30 °C / 60% RH (MSL 3) for different time intervals (0, 1, 3, 10, 30, 60 days). All the tests have been performed at T = 25 °C, and at three stress levels including 20, 40 and 60 MPa. The stress levels were chosen from 25-75% of the Ultimate Tensile Strength.

In a typical creep curve (Figure 4-13), the initial "elastic" strain level is followed by regions of primary and secondary creep. A very long duration of nearly constant slope is referred as the secondary creep region. This steady creep rate is often used by engineers as one of the key material parameters in finite element simulations. The measured creep rates were taken to be the slope values at the end of the linear portion in the observed secondary creep regions.

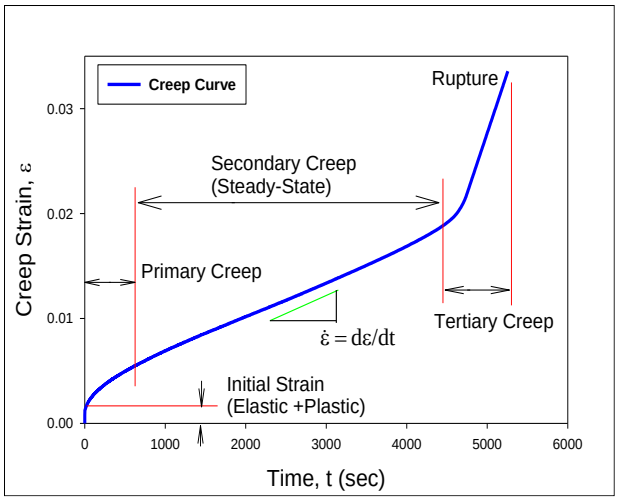

Figure 4-13 Typical Creep Curves

Due to long testing time, 3 specimens have been tested for each moisture exposure condition. The curves in each set were fitted with an empirical strain-time model to generate an "average" representation of the creep response for those circumstances. For the variety of test conditions considered in this work, the raw strain versus time data in the primary and secondary creep regions was found to be well fitted by an empirical Log Hyperbolic Tangent model:

Typical average creep data for no moisture exposure, and 60 days of moisture exposure at MSL 1 and MSL 2 are shown in Figure 4-14, Figure 4-15 and Figure 4-16 respectively. The extracted secondary creep rates for MSL 1 condition at different stress levels are shown in Table 4-4. MSL 2 and 3 conditions secondary creep rates are also given in Table 4-5 and Table 4-6 respectively.

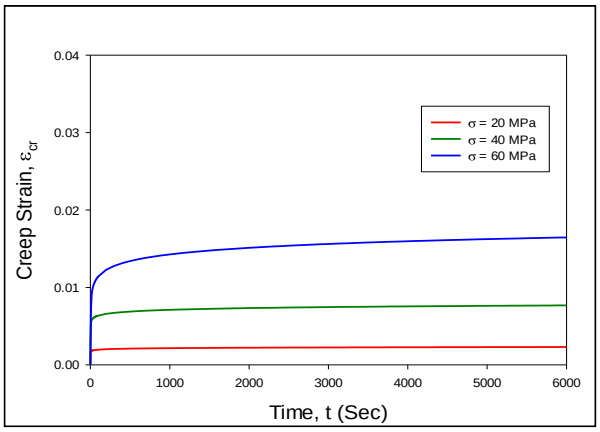

Figure 4-14 No Moisture Exposure

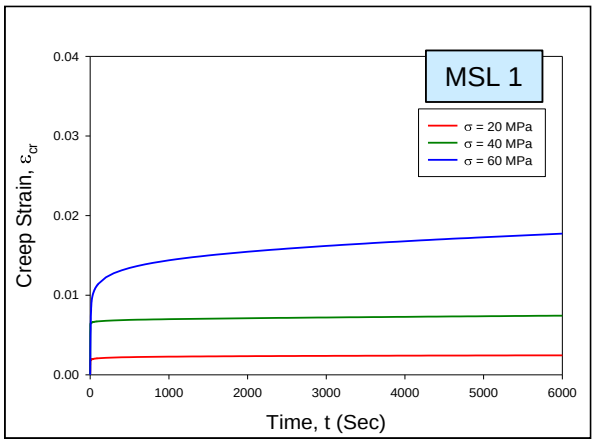

Figure 4-15 60 Days of Moisture Exposure at 85 ^{o}C /85 % RH

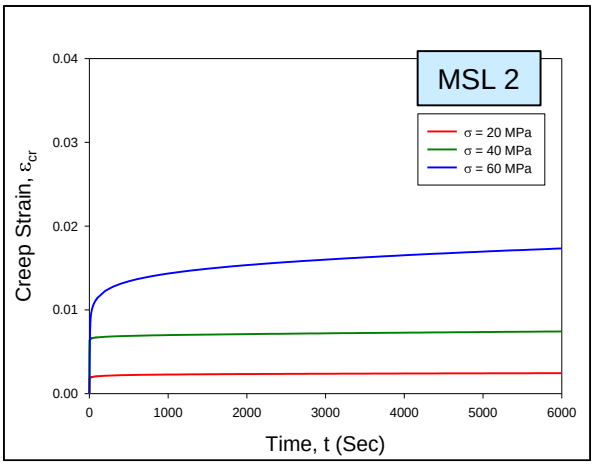

Figure 4-16 60 Days of Moisture Exposure at 85 ^{o}C /60 % RH

Table 4-4 Creep Strain Rate Variation at MSL 1

Moisture Exposure (85 ^{o}C, 85% RH)	σ = 20 MPa	σ = 40 MPa	σ = 60 MPa
None	1.67×10^{-8}	6.43×10^{-8}	25.06×10^{-8}
1 Day	1.72×10^{-8}	6.63×10^{-8}	27.79×10^{-8}
3 Days	1.79×10^{-8}	6.95×10^{-8}	30.39×10^{-8}
10 Days	1.85×10^{-8}	7.07×10^{-8}	33.64×10^{-8}
30 Days	1.95×10^{-8}	7.20×10^{-8}	38.57×10^{-8}
60 Days	2.03×10^{-8}	7.37×10^{-8}	42.69×10^{-8}

Table 4-5 Creep Strain Rate Variation at MSL 2

Moisture Exposure (85 ^{o}C, 60% RH)	σ = 20 MPa	σ = 40 MPa	σ = 60 MPa
None	1.67×10^{-8}	6.43×10^{-8}	25.06×10^{-8}
1 Day	1.70×10^{-8}	6.55×10^{-8}	26.80×10^{-8}
3 Days	1.77×10^{-8}	6.68×10^{-8}	28.66×10^{-8}
10 Days	1.83×10^{-8}	6.89×10^{-8}	31.59×10^{-8}
30 Days	1.90×10^{-8}	7.11×10^{-8}	35.27×10^{-8}
60 Days	1.95×10^{-8}	7.26×10^{-8}	39.27×10^{-8}

Table 4-6 Creep Strain Rate Variation at MSL 3

Moisture Exposure (30 °C, 60% RH)	σ = 20 MPa	σ = 40 MPa	σ = 60 MPa
None	1.67×10^{-8}	6.43×10^{-8}	25.06×10^{-8}
1 Day	1.67×10^{-8}	6.52×10^{-8}	25.89×10^{-8}
3 Days	1.68×10^{-8}	6.54×10^{-8}	26.91×10^{-8}
10 Days	1.71×10^{-8}	6.62×10^{-8}	28.42×10^{-8}
30 Days	1.72×10^{-8}	6.74×10^{-8}	30.11×10^{-8}
60 Days	1.74×10^{-8}	6.84×10^{-8}	33.24×10^{-8}

The secondary creep rate was seen to increase with increasing moisture exposure time. This effect was exacerbated at higher stress levels. For example, the increases in the secondary creep rate for σ = 60 MPa were 70.4%, 56.7%, and 32.6% for 60 days of moisture exposure at MSL 1, MSL 2, and MSL 3 conditions, respectively. Variations in secondary creep strain rate at different moisture conditions are shown in Figure 4-17.

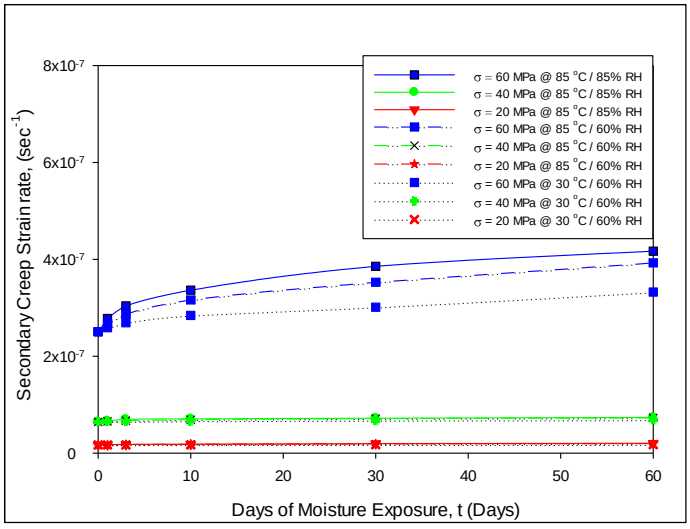

Figure 4-17 Secondary Creep Rate Variations with Moisture Exposure Time

4.6 Moisture Absorption Study

The objective of this section is to characterize the diffusion of moisture in underfill materials. Instead of the exposure time in the humidity chamber, the moisture

concentration or moisture content was used to characterize the moisture condition of the material. The test protocol is as follows:

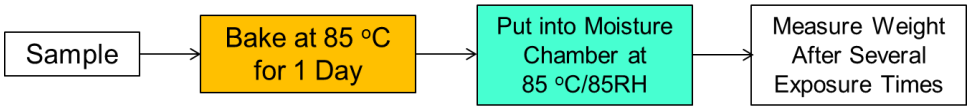

At first, test samples were prepared according to the curing condition. As these samples absorb moisture, they were baked first to reach the dry state. The bake out condition is believed to depend on the geometry and storage time of samples. In this study, bake out of the samples was done at 85 °C for 24 hours, and the weights of the dry samples were measured using an electronic balance. The samples were then placed in an environmental/humidity chamber and exposed to MSL 1, MSL 2, and MSL 3 conditions. For each MSL level, the weights of samples were measured after various exposure durations up to 1200 hours. Figure 4-18 shows a typical change in mass (moisture mass), or mass of water in the sample, as a function of exposure time for four samples exposed to MSL 1 conditions. Using the Fickian diffusion model, the diffusivity D was evaluated by fit of eq. (1) to the experimental data. Figure 4-19 shows the analogous experimental data for MSL 1, MSL 2, and MSL 3 exposure conditions, and the extracted values of diffusivity are tabulated in Table 4-7. As expected, the diffusivity decreases as the severity of the moisture exposure is reduced from MSL 1 to MSL 2 to MSL 3.

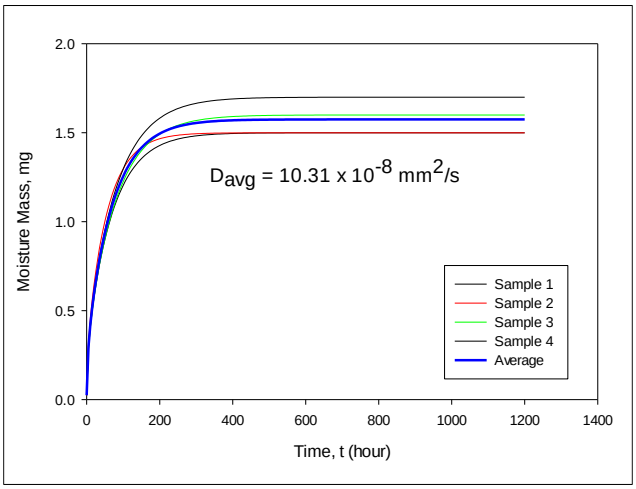

Figure 4-18 Moisture Mass vs. Exposure Time and Fit of Fickian Model (MSL 1)

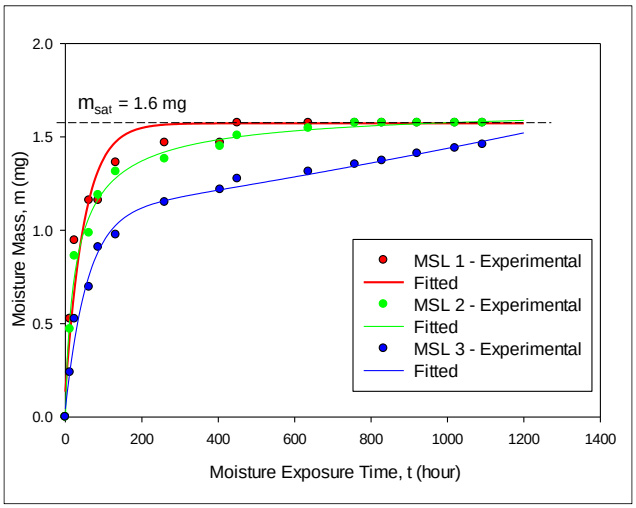

Figure 4-19 Moisture Mass vs. Exposure Time for Different MSL Exposure Conditions

Table 4-7 Measured Diffusivity Values

Condition	D (mm^2/s)
MSL 1	10.3 x 10^{-8}
MSL 2	8.7 x 10^{-8}
MSL 3	2.2 x 10^{-8}

The Moisture Content (MC) of a material referenced to the dry state is defined as

$$MC = \frac{M(t) - M_{Dry}}{M_{Dry}} \text{ x } 100 = \frac{m(t)}{M_{dry}} \text{ x } 100 \tag{4.7}$$

while the moisture concentration C of a material is defined as

$$C = \frac{m(t)}{V} \tag{4.8}$$

where m(t) is the moisture mass (mass of water) in the sample, M(t) is the total mass of the sample, M_{sat} is the saturated total mass of the sample, and V is the volume of the sample.

Using Equations 4.7 and 4.8, the moisture mass data in Figure 4-19 has been replotted as Moisture Content versus exposure time and Concentration versus exposure time, as shown in Figure 4-20 and Figure 4-21 respectively.

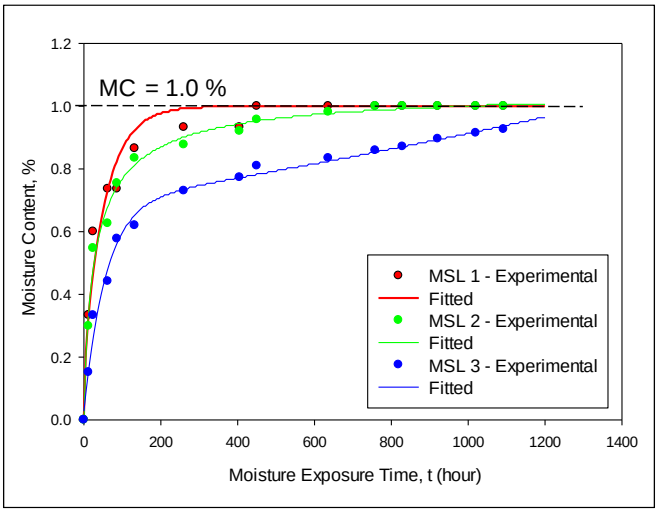

Figure 4-20 Moisture Content vs. Exposure Time for Various MSL Levels

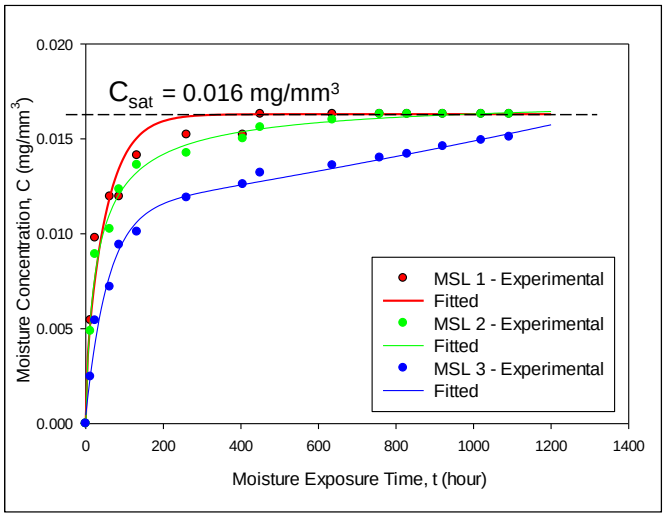

Figure 4-21 Moisture Concentration vs. Exposure Time for Various MSL Levels

4.7 Material Property Variation with Moisture Concentration

In Figure 4-11,Figure 4-12 and Figure 4-17, the material properties of the underfill were plotted versus the moisture exposure time in the humidity chamber, and different results were observed for the three different MSL levels considered (three different exposure severities considered). Using the results in Figure 4-21, these plots have been recast to illustrate the variation of material properties with the moisture concentration in the sample. The results for the initial elastic modulus and Ultimate Tensile Strength are shown in Figure 4-22 and Figure 4-23 respectively. It is observed that the data for the various MSL levels (various severities of exposure conditions) now lie on top of one another and show a linear variation with moisture concentration. This point can be further illustrated by using a single linear curve to fit the data from all the MSL conditions as shown in Figure 4-24 and Figure 4-25.

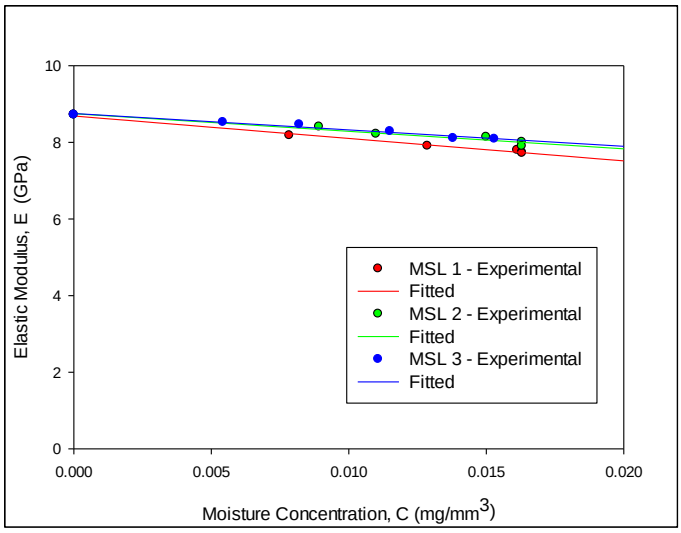

Figure 4-22 Elastic Modulus vs. Concentration for Different MSL Exposure Conditions

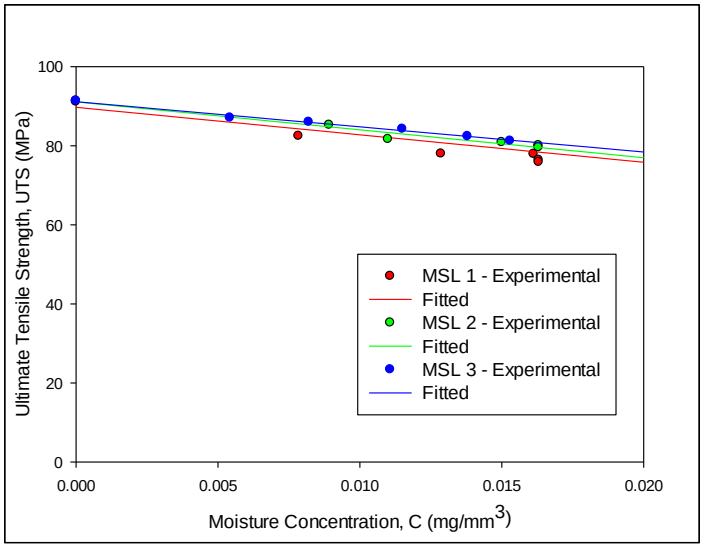

Figure 4-23 Ultimate Tensile Strength vs. Concentration for Different MSL Exposure Conditions

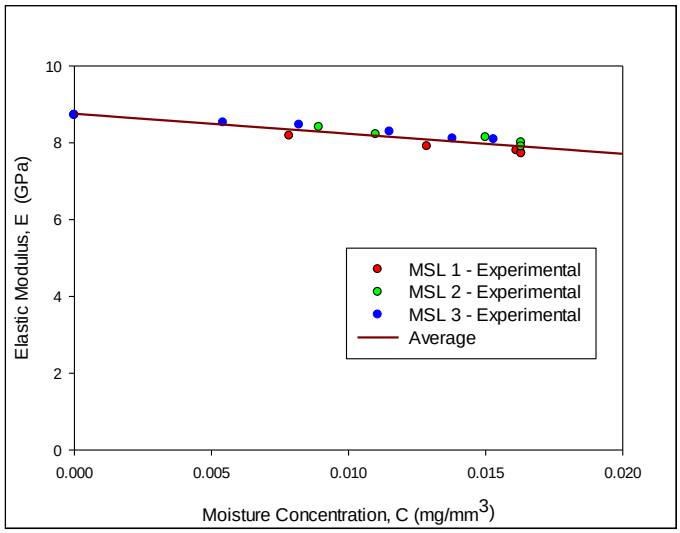

Figure 4-24 Elastic Modulus vs. Concentration for Different MSL Exposure Conditions (Single Linear Fit)

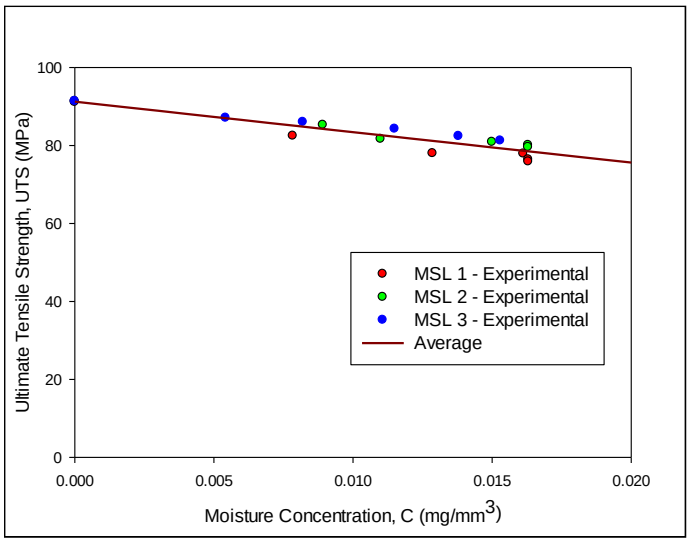

Figure 4-25 Ultimate Tensile Strength vs. Concentration for Different MSL Exposure Conditions (Single Linear Fit)

The results in Figure 4-24 and Figure 4-25 suggest that the dependence of the mechanical properties on moisture concentration is independent of the MSL level used to force the moisture into the sample. Thus, the mechanical properties are only dependent on

amount of water that has been absorbed by the material, regardless of how rapidly it was absorbed. Using the results in Figure 4-17 and Figure 4-21, a similar result was found for the variation of secondary creep rate with moisture concentration. For each applied stress level, the secondary creep rate data were found to lie right on top of one another for the various MSL exposure conditions, and a single model could be used to fit all of the data.

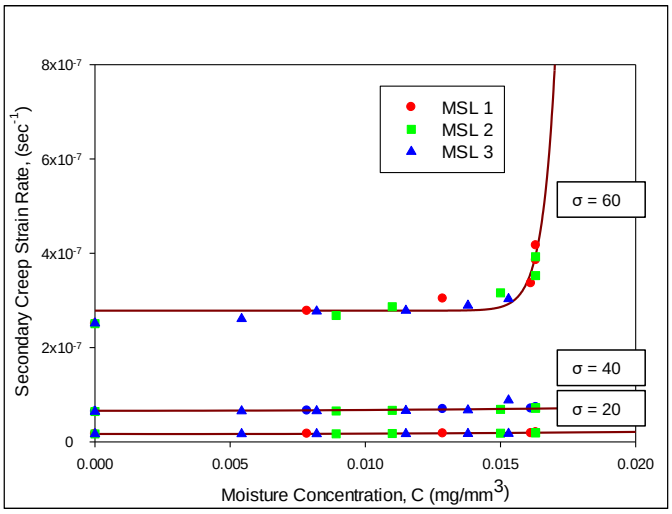

Figure 4-26 Creep Rate vs. Concentration

4.8 Summary and Discussion

A preliminary study was performed to determine effects of moisture exposure on the stress-strain and creep behaviors of a typical underfill material. In particular, new results detailing the effects of preconditioning on the stress-strain behavior and the effects of moisture on the creep behavior of underfills have been presented. The specimens were exposed in an adjustable thermal and humidity chamber at a particular controlled temperature and humidity condition for specific time duration. It is found that moisture diffuses into the underfill and degrades the mechanical properties of the encapsulant (initial

elastic modulus and ultimate tensile stress) up to 15%. We also found that moisture exposure slowly increases the secondary creep strain rate except at high stress levels.

Preconditioning by baking the samples for 24 hours at 85 ^{o}C was found to increase the initial material properties, but the degradations due to subsequent moisture exposures occurred in a similar manner. For 60 days of moisture exposure, the observed increases in the secondary creep rate ranged from 20-70% for applied stress levels between 20-60 MPa. MSL 1 condition degrade the material property more quickly than MSL 2 and MSL 3. Lower elastic modulus and ultimate tensile strength values were found for MSL 1 relative to the values found for MSL 2 and MSL 3.

The initial elastic modulus and Ultimate Tensile Strength were found to vary linearly with moisture concentration, and the response was not dependent on the MSL level used to force the moisture into the sample. Thus, the mechanical properties are only dependent on amount of water that has been absorbed by the material, regardless of how rapidly it was absorbed. Similar results were found for the variation of secondary creep rate with moisture concentration. For each applied stress level, the secondary creep rate data were found to lie right on top of one another for the various MSL exposure conditions, and a single model could be used to fit all of the data.

CHAPTER 5

CHARACTERIZATION OF VISCOELASTIC RESPONSE OF UNDERFILL MATERIALS

5.1 Introduction

In microelectronic packaging, different kinds of polymers are used to maintain a good balance with electrical properties and mechanical properties. They need to perform well for environmental protection, resistance to mechanical shock and temperature. Underfill materials are silica filled epoxy and its property is influenced by time and temperature. The underfill material shows time-dependent mechanical response which insists that for accurately model microelectronic packaging, the time and temperature dependent mechanical properties needs to be investigated. Constitutive models are needed to study and capture the rate dependent stress strain behavior of polymers. In this study, viscoelastic material models have been studies to represent the tensile and creep behavior of polymers. Using the model experimental data was fitted and optimum viscoelastic Prony coefficients was measured using DMA and stress relaxation experiments. Then these coefficients are used in correlate the experimental data and determine the best parameters for correctly represent viscoelastic behavior.

5.2 Generalized Maxwell Model

Viscoelastic materials could be modeled by different rheological models. One of these basic rheological models for modeling viscoelasticity was proposed by James Clerk

Maxwell in 1867. This model includes both elastic and viscous property of the material and consists of a linear ideally viscous Newtonian damper and linear ideally elastic hookian spring in series. If we put the elements in parallel, then the model would be named as Kelvin-Voigt. Figure 5-1 shows the Maxwell model. The force is equal in each of the parts due to the series connection of the elements. However, the total strain would be equal to the summation of strain in elastic and viscous elements. For relaxation test, viscous part needs some time to move, however, spring can move instantaneously. So, the whole displacement will be compensated by the spring at time zero. As the time goes on, the dashpot will have also enough time to move, and then the displacement would decrease from the spring and increase the damper. As the time goes infinity, the strain in elastic part would be zero and therefore its stress will be zero as well. Stress in the whole Maxwell branch is then zero. Simple Maxwell model in modeling complicated elastomers creates problem as stress in these materials for long time would not lead to zero. That's why a general Maxwell model is required.

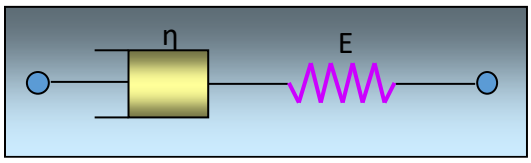

Figure 5-1 Maxwell Model

As Maxwell model has the problem of providing zero stress at time infinity in relaxation test, the general Maxwell model was proposed to solve the problem and to be used in appropriate modeling of complicated viscoelastic materials. It observes that relaxation does not occur at a single time, but at a distribution of times. Figure 5-2 shows the rheological model of "General Maxwell".

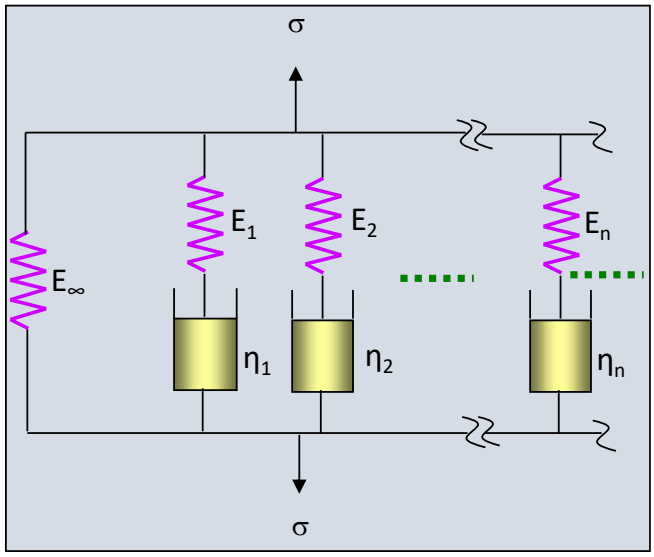

Figure 5-2 Generalized Maxwell Model

Viscoelastic behavior can be divided into large and small deformation. In large deformation modeling one of the hyperelastic models should also be added in order to get a hyperelastic material at the end. However, when the strain is small, initial shear and bulk modulus values would be enough as the starting values of the material properties over the

time. These shear and bulk modules are representative of deviatoric and volumetric parts of the stress respectively equation

$$\sigma = \sigma_{\text{devatoric}} + \sigma_{\text{volumetric}} \tag{5.1}$$

$$\sigma_{ij} = \int_0^t 2G\left(t-\tau\right)\frac{de_{ij}}{d\tau}\,d\tau + \delta_{ij}\int_0^t K\left(t-\tau\right)\frac{d\Delta}{d\tau}\,d\tau \tag{5.2}$$

Where σ_{ij} are the components of the Cauchy stress, e_{ij} are the deviatoric strain components, Δ is the volumetric part of the strain, G(t) and K(t) are the shear and bulk modulus functions, t and τ are current and past time, and δ_{ij} are the components of the unit tensor (Kronecker delta)

$$\text{Kronecker delta,}\quad \delta_{ij} = \begin{bmatrix} 1 & 0 & 0 \\ 0 & 1 & 0 \\ 0 & 0 & 1 \end{bmatrix}$$

For the Generalized Maxwell model, the shear and bulk modulus functions can be expressed in a Prony series format [93]

$$G = G_\infty + \sum_{i=1}^{n_G} G_i \exp\left(-t/\tau_i^G\right) \tag{5.3}$$

$$K = K_{\infty} + \sum_{i=1}^{n_K} K_i \exp\left(-t/\tau_i^K\right) \tag{5.4}$$

Where G and Gi are the shear elastic moduli, K and Ki are the bulk elastic moduli and are the relaxation for the various Prony series components.

Equations (5.3, 5.4) can be rewritten as

$$G = G_0 \left[\alpha_{\infty}^G + \sum_{i=1}^{n_G} \alpha_i^G \exp\left(-t/\tau_i^G\right) \right] \tag{5.5}$$

$$K = K_0 \left[\alpha_{\infty}^K + \sum_{i=1}^{n_K} \alpha_i^K \exp\left(-t/\tau_i^K\right) \right] \tag{5.6}$$

Where

$$G_0 = G_{\infty} + \sum_{i=1}^{n_G} G_i \tag{5.7}$$

$$K_0 = K_{\infty} + \sum_{i=1}^{n_G} K_i \tag{5.8}$$

G_0 and K_0 are referred to as the instantaneous shear and bulk moduli, and

$$\alpha_i^G = G_i / G_0 \tag{5.9}$$

$$\alpha_i^K = K_i / K_0 \tag{5.10}$$

α_i are referred to as the relative moduli.

$$K_0 = K_\infty + \sum_{i=1}^{n_G} K_i \tag{5.11}$$

5.3 Time-Temperature Superposition and Shift Functions

Unlike other well-known rate-dependent models, Prony series does not contain any temperature term. For describing the effect of temperature, two methods are available. One method is to use different Prony series for different temperatures; however, the other method, shift function, is typically employed for adjusting the Prony series to adapt to different temperatures.

Suppose at temperature T0 and time t0, the modulus can be expressed as

$$E(t_0^{(T_0)}) = E_\infty + \sum_{i=1}^{n} E_i \exp\left(-\frac{t_0^{(T_0)}}{\tau_i^{(T_0)}} \right) \tag{5.12}$$

At a higher temperature T_1, the same relaxation modulus value is found at time t_1

$$E(t_1^{(T_1)}) = E_\infty + \sum_{i=1}^{n} E_i \exp\left(-\frac{t_1^{(T_1)}}{\tau_i^{(T_1)}}\right) = E(t_0^{(T_0)}) \tag{5.13}$$

Hence, we may obtain

$$\tau_i^{(T_0)} = \frac{t_0^{(T_0)}}{t_1^{(T_1)}} \tau_i^{(T_1)} \tag{5.14}$$

By substituting $\frac{t_0^{(T_0)}}{t_1^{(T_1)}} = a_T$ and taking the logarithm, we get

$$\log\left(t_1^{(T_1)}\right) = \log\left(t_0^{(T_0)}\right) - \log a_T \tag{5.15}$$

Hence, we can extent a conclusion that if we set time axis in a logarithmic scale, we can plot the stress relaxation curve under one temperature by shifting the curve obtained under another temperature. This is known as the time–temperature superposition principle, and the material obeying this principle is denoted as a thermorheologically simple material. The logarithm of a_T is called the shift function.

5.3.1 Master Curve

Based on the assumption of thermorheologically simple material, DMA and stress relaxation experiments can be done at different temperatures, and the results can be fitted

into a “master curve,” and then Prony series can be determined from the master curve. The horizontal shift distance can be determined and then used to measure the constants in the shift function. This process can be performed by either using mathematical analysis tools or FEA software.

5.3.2 Shift Functions

In engineering, William-Landel-Ferry (WLF) function is most frequently used for polymers. The WLF function takes the following format:

$$\log_{10} a_T = \frac{-C_1 \left(T - T_{ref} \right)}{C_2 + \left(T - T_{ref} \right)} \tag{5.16}$$

Here, C_1 and C_2 are two dimensionless constants, and

T_{ref} is a reference temperature chose to construct the Mastercurve.

Another commonly used shift function, the Tool- Narayanaswamy (TN) function, takes the Arrhenius form

$$\ln a_T = -C_1 \left(\frac{1}{T} - \frac{1}{T_{ref}} \right) \quad \text{or} \quad \log_{10} a_T = -\frac{C_1}{2.303} \left(\frac{1}{T} - \frac{1}{T_{ref}} \right) \tag{5.17}$$

Where a_T is the shift factor, C_1 and C_2 are material constants, T = T (t) is the temperature at time t, and T_{ref} is the reference temperature at time t_r.

Figure 5-3 shows the typical flip chip on laminate assembly. The primary failure mode for underfill is delamination at the underfill/die or underfill/substrate interfaces. Such delamination happens when the interfacial stress between the underfill and silicon/substrate is greater than the interfacial adhesion strength of the underfill polymer. One of the critical issues in electrical packages is to stop the initiation and growth of delamination. But if the cracks start and propagate to solder bumps, the solder joints will be damaged badly, and fatigue cracking will be faster.

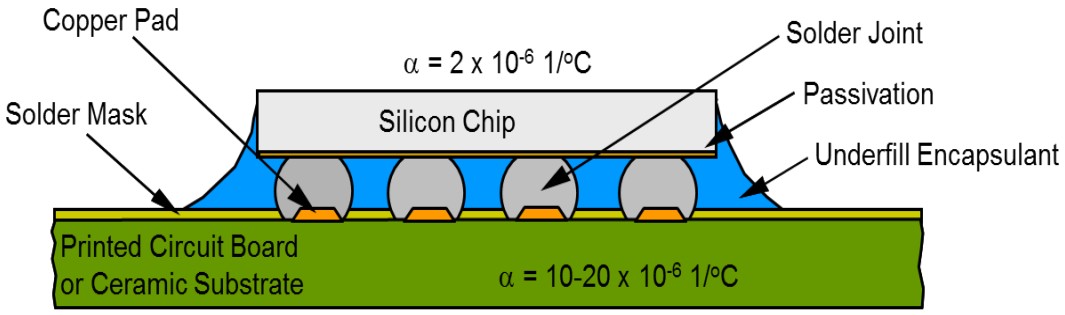

Figure 5-3 Schematic of a Flip Chip on Laminate Assembly

There are two ways to characterize viscoelastic properties [94]. One way is to measure by DMA, where dynamic responses of a material are measured at several oscillation frequencies over a wide range of isothermal temperatures. The complex modulus in the frequency domain can be transformed to relaxation modulus in the time domain by using an appropriate relationship. Another approach is using stress relaxation test at different isothermal temperatures. In this way relaxation modulus can be found directly without using approximation equation. Both cases a master curve can be

constructed using the time temperature equivalence which holds for thermorheologically simple materials (TSM) [71], [72], [95], [96].

In our previous study on underfill [87], [88], we didn't incorporate the viscoelastic behavior. But, underfills are usually silica filled epoxy polymers, so viscoelastic characterization is very important as this material shows time and temperature dependent properties. In this study, we want to explore more on characterizing viscoelastic behavior of underfill material and co related this result with finite element analysis to predict mechanical behavior. Master curve and shift factors were utilized to see the behavior in both DMA and stress relaxation test. In microelectronics packaging industry, polymer-based materials are used extensively. These polymers exhibit viscoelastic behavior when subject to time dependent loads or deformations. The viscoelastic behavior highly depends on both temperature and time. In many cases, these viscoelastic properties are often neglected due to saving computational cost, or unavailability of a full characterization of the viscoelastic properties. To make accurate predictions of packaging behavior, it is important to accurately characterize the viscoelastic behavior of mold compounds, underfill encapsulants, adhesives and other polymers used in electronic assemblies.

5.4 Experimental Procedure

In this experiment a commercially available underfill material has been used to perform the dynamic mechanical analysis (DMA), stress-strain and creep experiments. Dynamic mechanical properties of the cured material were determined between 60 to 160

^{o}C. The time-temperature superposition (TTS) experiments were performed using a TA Instruments RSA3 DMA system (Figure 5-4), which is operated in tensile mode. The sample were shown in Figure 5-5. The frequency sweep/temperature step test method was used which was shown in Figure 5-6. During the experiment, sample temperature was increased stepwise from 60 to 160 ^{o}C, with a step of 5 ^{o}C. A typical DMA test was shown in Figure 5-7. At each isothermal temperature, the frequency f was scanned over three decades between 0.1 and 10 Hz with a total of 8 discrete frequencies, which were: 0.1, 0.5, 1, 1.5, 2, 3, 5, 10 Hz (Figure 5-8 and Figure 5-9). These frequencies were selected so that they were approximately equally spaced on the logarithmic scale. The sample size was kept at 20 mm, and the typical sample width was 3 mm, with a thickness of 0.125 mm (5 mils).

Figure 5-4 TA Instruments RSA3 DMA System

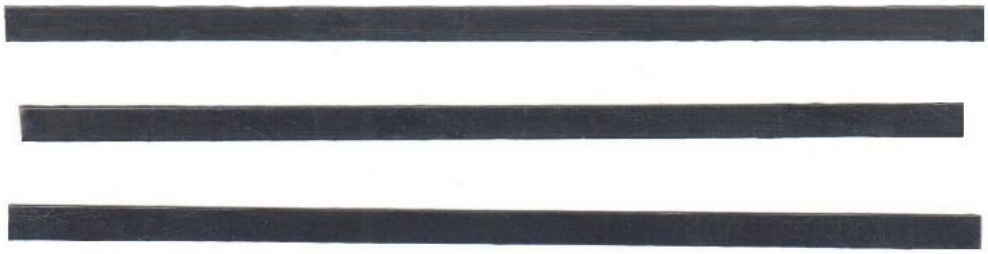

Figure 5-5 Test Specimens

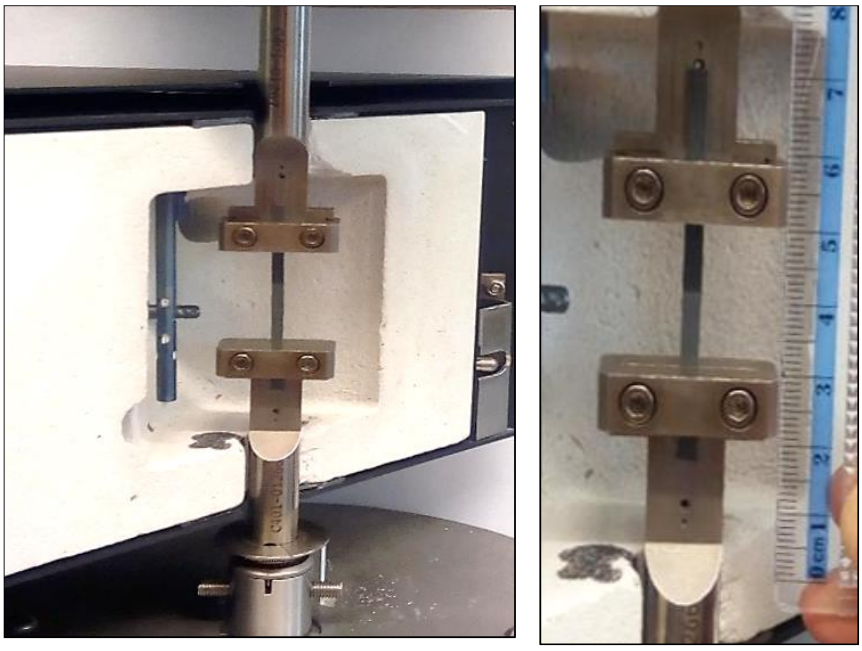

Figure 5-6 Frequency Sweep / Temperature Step Test

From the measured spectra of the moduli, the master curves were constructed by shifting the isothermal curves horizontally with respect to an arbitrarily selected reference temperature along the frequency axis.

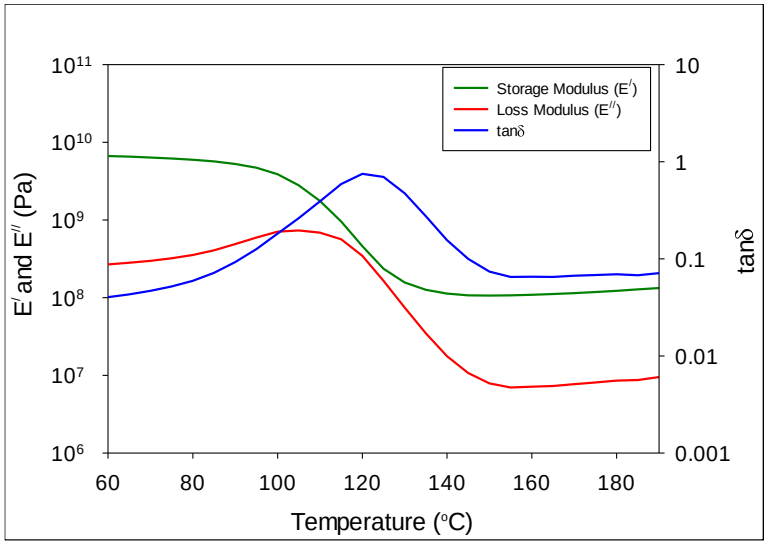

Figure 5-7 Testing Performed at frequency 1 Hz

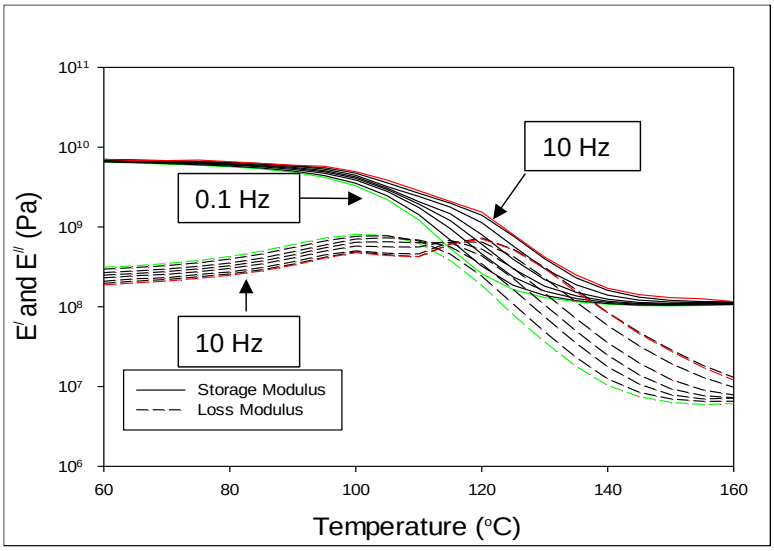

Figure 5-8 Testing Performed at frequency: 0.1, 0.5, 1, 1.5, 2, 3, 5, 10 Hz

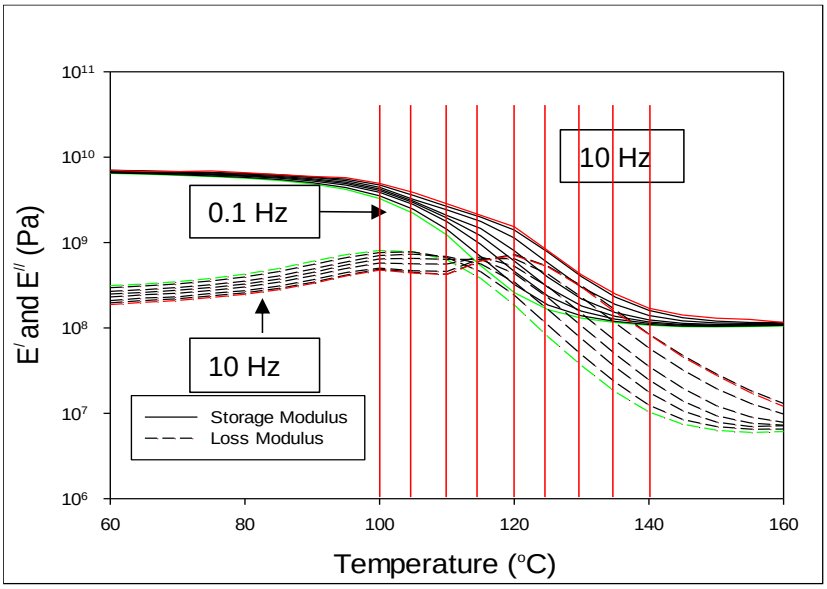

Figure 5-9 Testing Performed at frequency: 0.1, 0.5, 1, 1.5, 2, 3, 5, 10 Hz

Storage modulus vs frequency data were shown in Figure 5-10. A master curve has been generated by horizontally shifting the data in logarithmic scale where the reference temperature was used T_0 = 120 °C. Figure 5-11 showed the horizontally shifted data and Table 5-1 showed the calculated shift factors. By shifting the data, a master curve can be formed which was given in Figure 5-13.

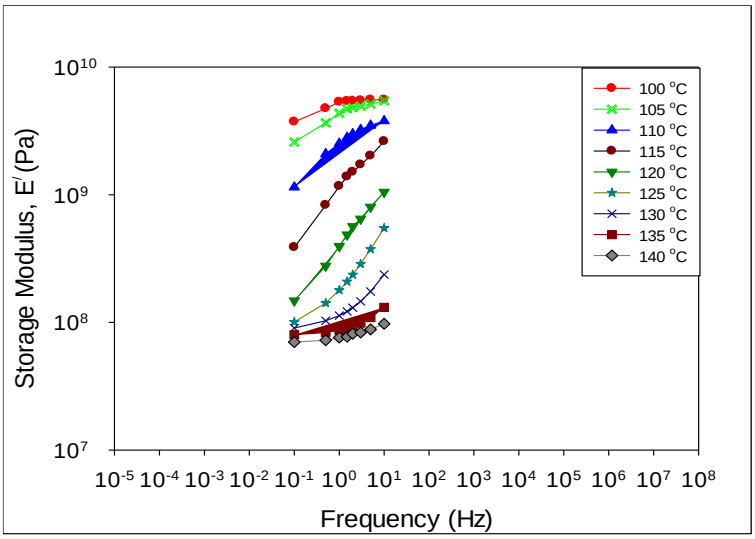

Figure 5-10 Frequency dependence of the storage modulus of a cured underfill at different isothermal temperatures.

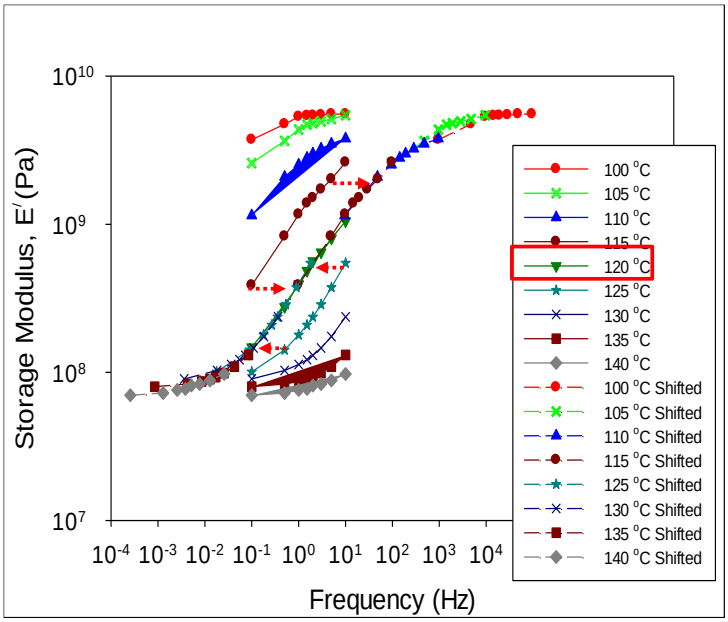

Figure 5-11 Master curves generated by shifting the storage (E´) using the TTS principle with respect to a reference temperature of 120 °C

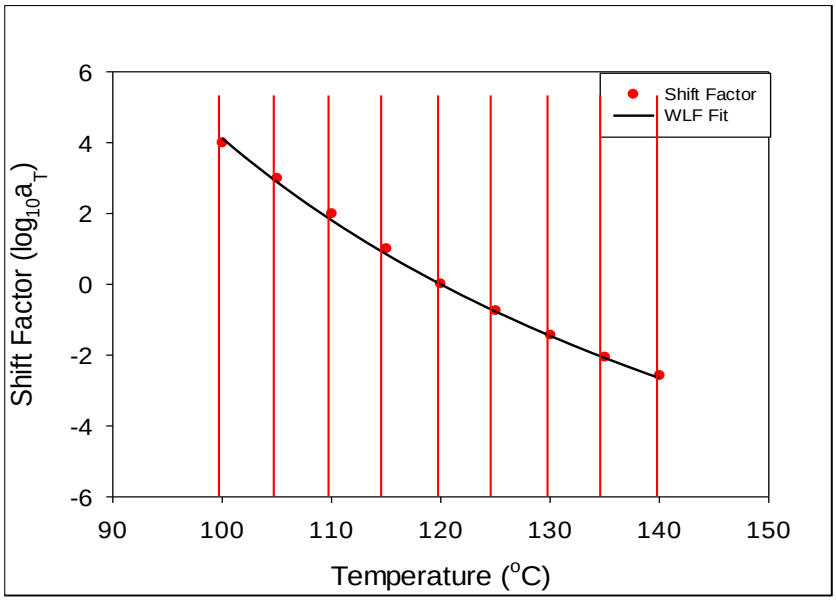

Figure 5-12 Horizontal shift factor vs temperature for a reference temperature of T_0 = 120 °C

Table 5-1 Calculated shift factor for a reference temperature of T0 = 120 °C

Shift Factors		
Temperature (°C)	a(T)	$Log_{10}a(T)$
100	9643.91	3.98
105	964.45	2.98
110	96.45	1.98
115	9.99	0.99
120	1	0
125	0.18	-0.75
130	0.036	-1.44
135	0.0085	-2.07
140	0.0025	-2.59

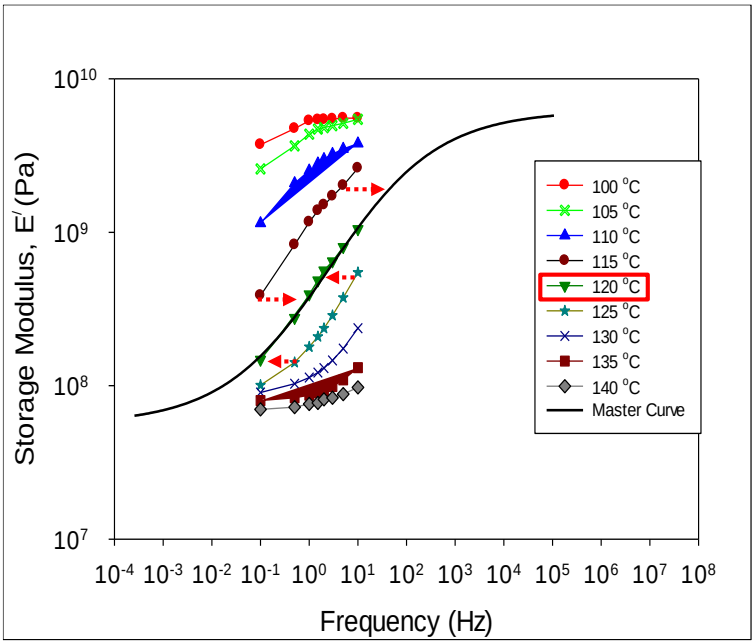

Figure 5-13 Master curve generated by shifting the storage (E´) using the TTS principle with respect to a reference temperature of 120 °C

A master curve can be generated for storage modulus, loss modulus and loss tangent using the TA orchestrator TTS (time temperature Superposition) software which was shown in Figure 5-14.

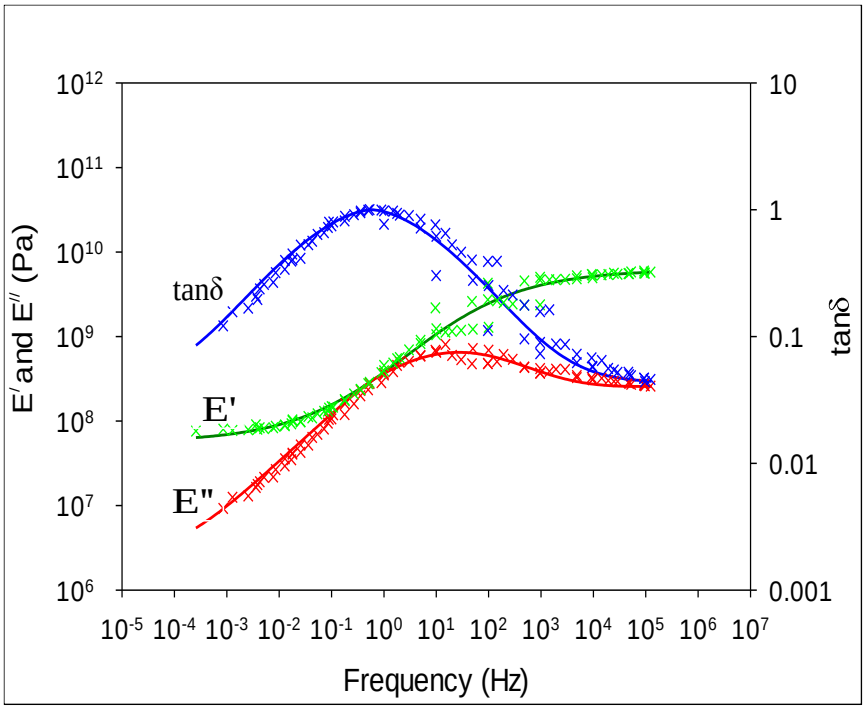

Figure 5-14 Master curves generated by shifting the storage modulus (E´), the loss modulus (E´´), and the loss tangent curves using the TTS principle with respect to a reference temperature of 120 °C

For modeling of package stress using finite element technique, relaxation modulus in the time domain need to know which is shown in Equation 5.18.

$$\sigma(t) = \int_{-\infty}^{t} E\left(t-\tau\right)\frac{\partial\varepsilon(\tau)}{\partial\tau}d\tau \tag{5.18}$$

Here, E is the relaxation modulus. This modulus also can be expressed in terms of the real and the imaginary part of the complex modulus, E′(ω) and E′′(ω). Then, the

relaxation modulus can be expressed in terms of E′(ω) and E′′(ω) which are shown respectively by Equation 5.19 and 5.20

$$E(t) = \frac{2}{\pi}\int_0^{\infty} \frac{E'(\omega)}{\omega} \sin \omega t \, d\omega \tag{5.19}$$

$$E(t) = \frac{2}{\pi}\int_0^{\infty} \frac{E''(\omega)}{\omega} \cos \omega t \, d\omega \tag{5.20}$$

After applying inverse Fourier transform several approximated equations can be estimated and using them frequency domain data can be converted to time domain (Figure 5-15). One expression is suggested by Schwarzl and Struik [97], [98]

$$E(1.25t) = E'(\omega) - 0.5303E''(0.5282\omega) - 0.021E''(0.085\omega) + 0.042E''(6.37\omega) \tag{5.21}$$

Another expression is proposed by Ninomiya and Ferry [99], [100]

$$E(t) = E'(\omega) - 0.4E''(0.4\omega) + 0.014E''(10\omega) \tag{5.22}$$

This conversion can be represented by graphically,

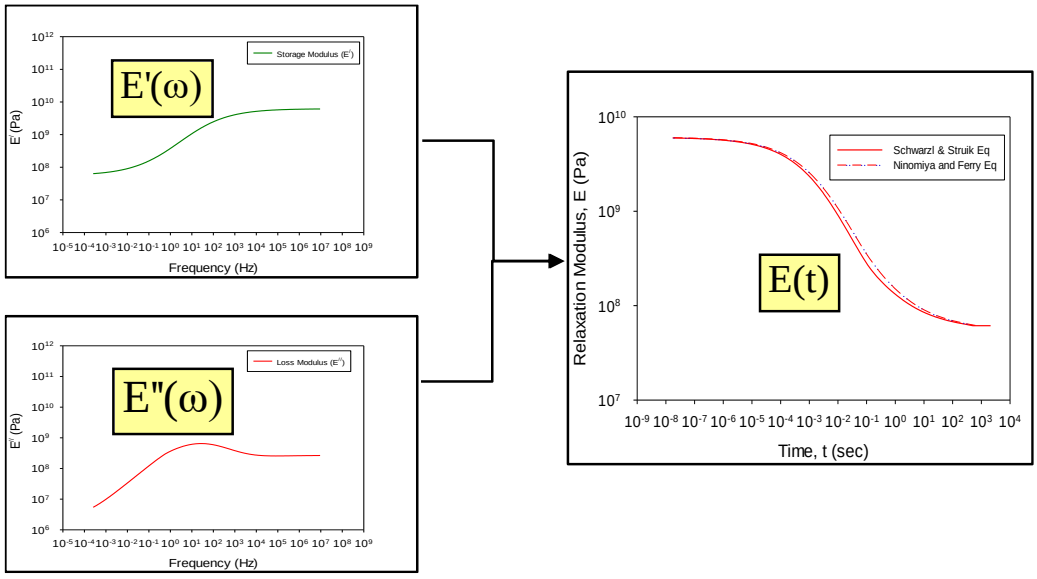

Figure 5-15 Conversion from frequency to time domain

A mathematical optimization method has been followed to solve nonlinear curve fitting problems in least square sense. Figure 5-16 showed the calculated time domain using equation 5.21 and fitted the curve using equation 5.23.

$$E = E_{\infty} + \sum_{i=1}^{n} E_i \exp\left(-t/\tau_i\right) \tag{5.23}$$

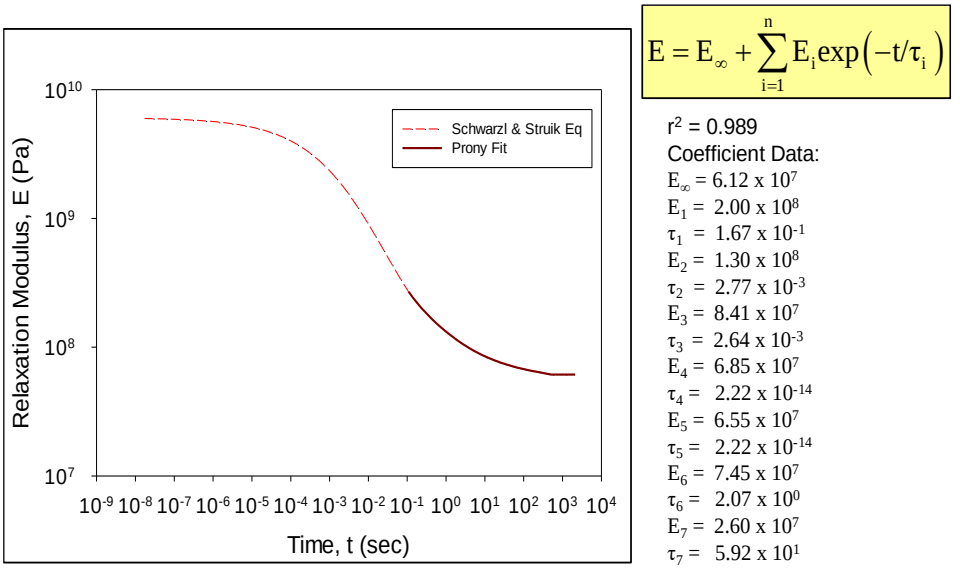

Figure 5-16 Relaxation Modulus vs Time

To convert the relaxation modulus into shear and bulk modulus Poisson's ratio is required. Shear modulus is defined by

$$G = \frac{E}{2(1+\upsilon)} \tag{5.24}$$

$$G = G_0\left[\alpha_\infty^G + \sum_{i=1}^{n_G} \alpha_i^G \exp\left(-t/\tau_i^G\right)\right] \tag{5.25}$$

Bulk modulus is defined by

$$K = \frac{E}{3(1-2\upsilon)} \tag{5.26}$$

$$K = K_0\left[\alpha_\infty^K + \sum_{i=1}^{n_K} \alpha_i^K \exp\left(-t/\tau_i^K\right)\right] \tag{5.27}$$

Where αi and τi are called the Prony pairs. Poisson's ratio is required to find shear and bulk modulus.

5.5 Poisson's Ratio Tests

Several specimens were tested at room temperature with a very small load with axial and transverse strain gages (Figure 5-17 and Figure 5-18). The typical sample size was 80 x 8 x 2 mm. The calculated Poisson's ratio was 0.2989 ~ 0.30.

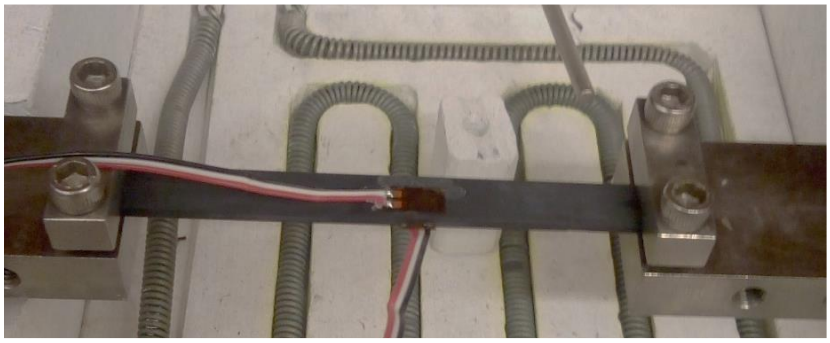

Figure 5-17 Poisson's ratio test

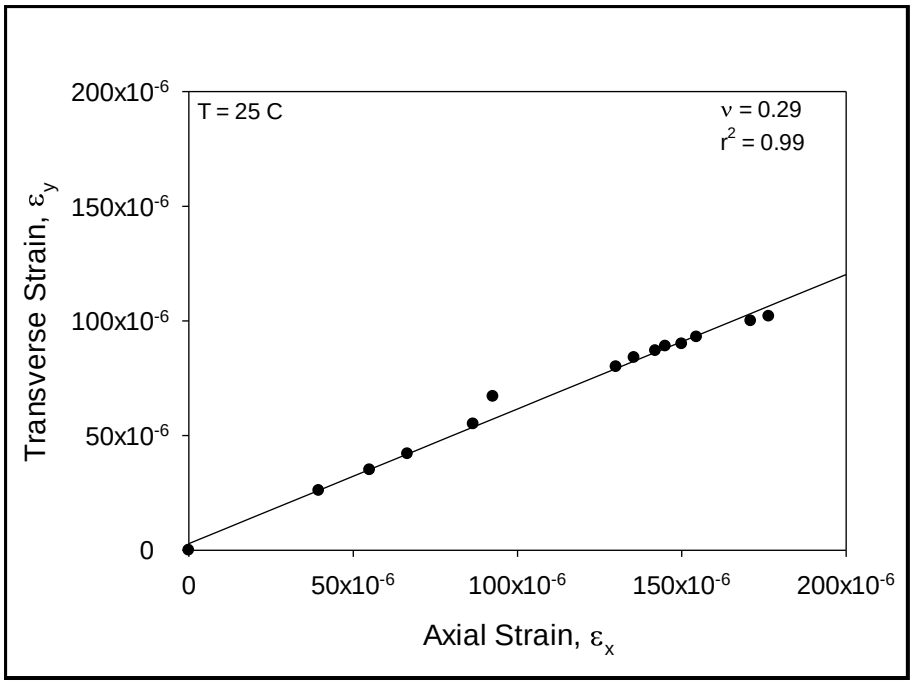

Figure 5-18 Poisson's ratio test data

Using the determined Poisson's ratio, shear and bulk modulus are calculated. The calculate shear and bulk modulus data were mathematically fitted with Prony series and sever Prony pairs were calculated (Figure 5-19 and Figure 5-20). The calculated Prony pairs were shown in Table 5-2.

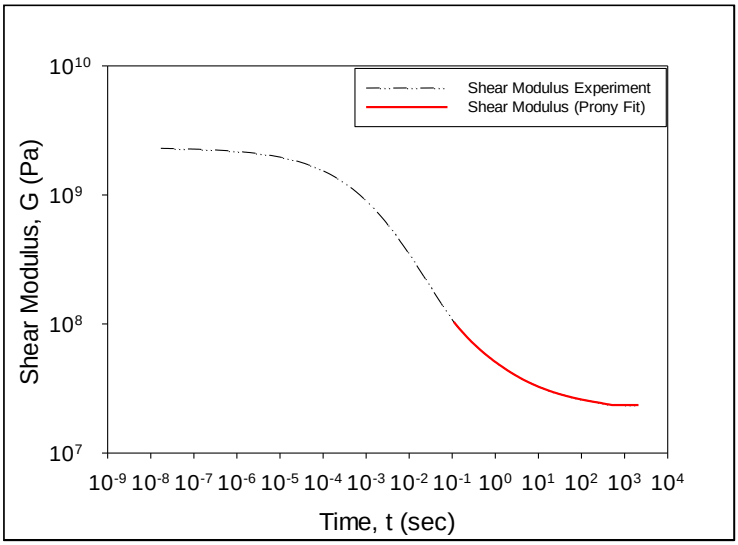

$$G = \frac{E}{2(1+\upsilon)}$$

$$G = G_0\left[\alpha_\infty^G + \sum_{i=1}^{n_G} \alpha_i^G \exp\left(-t/\tau_i^G\right)\right]$$

Figure 5-19 Shear Modulus vs Time

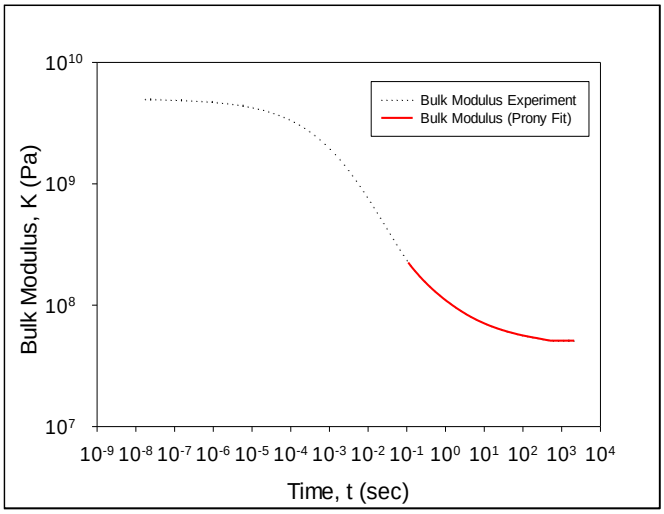

$$K = \frac{E}{3(1-2\upsilon)}$$

$$K = K_0\left[\alpha_\infty^K + \sum_{i=1}^{n_K} \alpha_i^K \exp\left(-t/\tau_i^K\right)\right]$$

Figure 5-20 Bulk Modulus vs Time

Table 5-2 Calculated Prony constants for Shear and Bulk Response

Constants for Shear Response	Constants for Volumetric Response	Constants for Shift Function (Williams-Landel-Ferry (WLF) Equation)
$\alpha_1 = 2.85 \times 10^{-1}$ $\tau_1 = 1.67 \times 10^{-1}$ $\alpha_2 = 1.82 \times 10^{-1}$ $\tau_2 = 2.77 \times 10^{-3}$ $\alpha_3 = 1.18 \times 10^{-1}$ $\tau_3 = 2.64 \times 10^{-3}$ $\alpha_4 = 9.60 \times 10^{-2}$ $\tau_4 = 2.22 \times 10^{-14}$ $\alpha_5 = 9.19 \times 10^{-2}$ $\tau_5 = 2.22 \times 10^{-14}$ $\alpha_6 = 1.05 \times 10^{-1}$ $\tau_6 = 2.07 \times 10^{0}$ $\alpha_7 = 3.65 \times 10^{-2}$ $\tau_7 = 5.92 \times 10^{1}$	$\alpha_1 = 2.85 \times 10^{-1}$ $\tau_1 = 1.67 \times 10^{-1}$ $\alpha_2 = 1.82 \times 10^{-1}$ $\tau_2 = 2.77 \times 10^{-3}$ $\alpha_3 = 1.18 \times 10^{-1}$ $\tau_3 = 2.64 \times 10^{-3}$ $\alpha_4 = 9.60 \times 10^{-2}$ $\tau_4 = 2.22 \times 10^{-14}$ $\alpha_5 = 9.19 \times 10^{-2}$ $\tau_5 = 2.22 \times 10^{-14}$ $\alpha_6 = 1.05 \times 10^{-1}$ $\tau_6 = 2.07 \times 10^{0}$ $\alpha_7 = 3.65 \times 10^{-2}$ $\tau_7 = 5.92 \times 10^{1}$	$T_{ref} = 120.0$ $C_1 = 14.76$ $C_2 = 91.52$

5.6 Stress Relaxation Tests

Stress relaxation test was performed in a micro tension torsion tester machine. The stress relaxation study has been conducted on underfill material specimens at 100, 110, 120, 130, and 140 ^{o}C. Stress relaxation experiment has been performed at $\varepsilon = 0.01$ i.e. 1%. The stress relaxation test data were shown in Figure 5-21 to Figure 5-24. Average relaxation modulus vs time data were shown in Figure 5-25 at different temperatures at 100, 110, 120, 130 and140 °C.

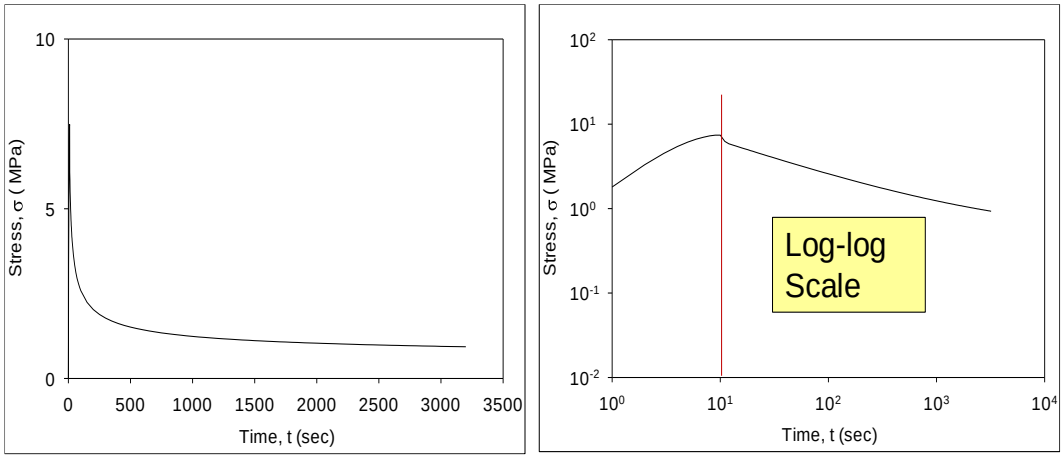

Figure 5-21 Stress Relaxation Test (Stress vs Time)

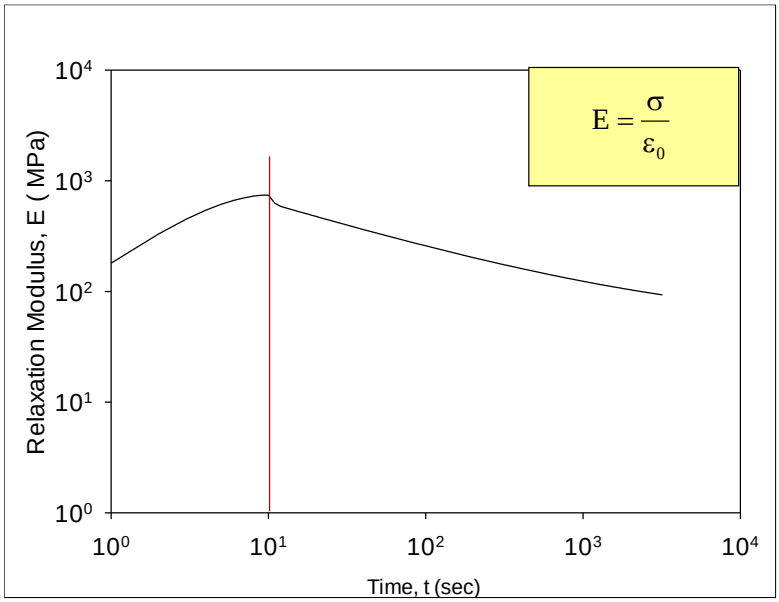

Figure 5-22 Relaxation Modulus vs Time

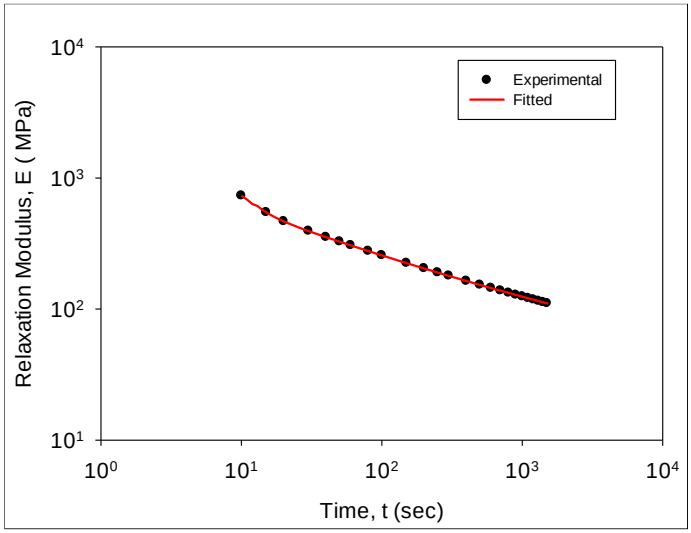

Figure 5-23 Fitted Experimental data

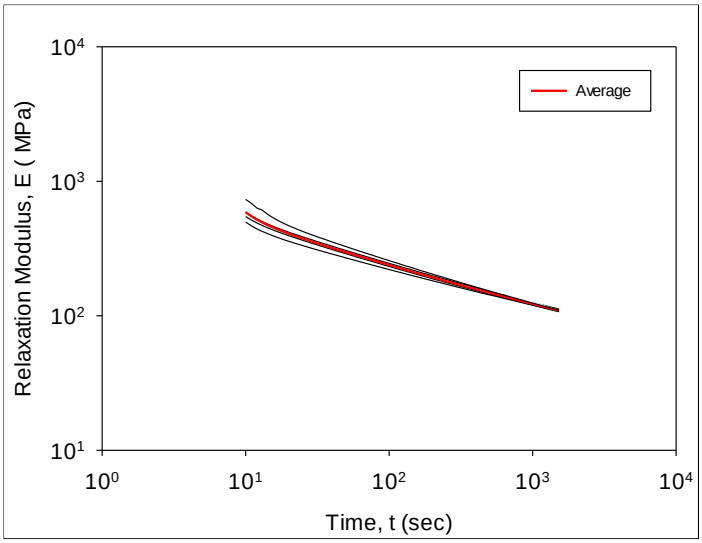

Figure 5-24 Average Curve for Relaxation Modulus

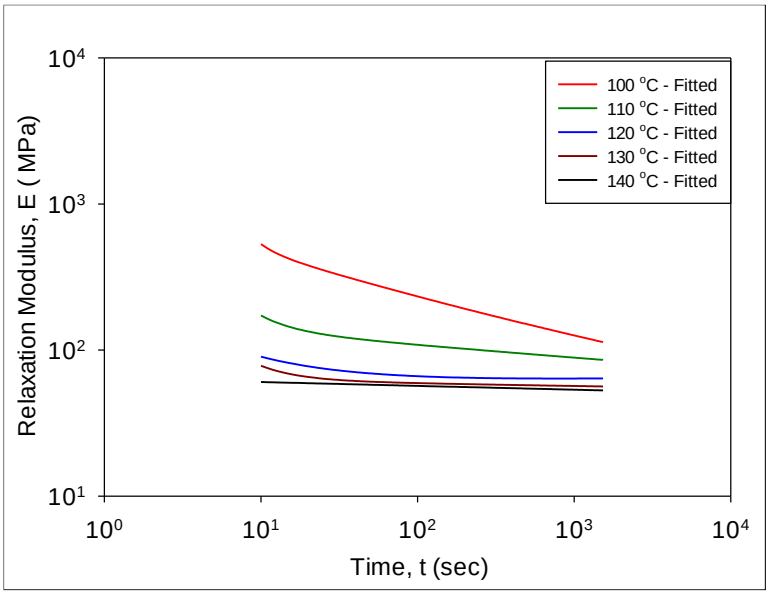

Figure 5-25 Relaxation Modulus vs Time at different temperatures

By shifting the curve horizontally, a master curve was generated which were shown in Figure 5-26 to Figure 5-28, and Table 5-3 showed the calculated shift factors. The reference temperature was maintained as 120 °C. The comparison between determined master curve using DMA and stress relaxation was shown in Figure 5-29. A nice correlation was found for both measurements.

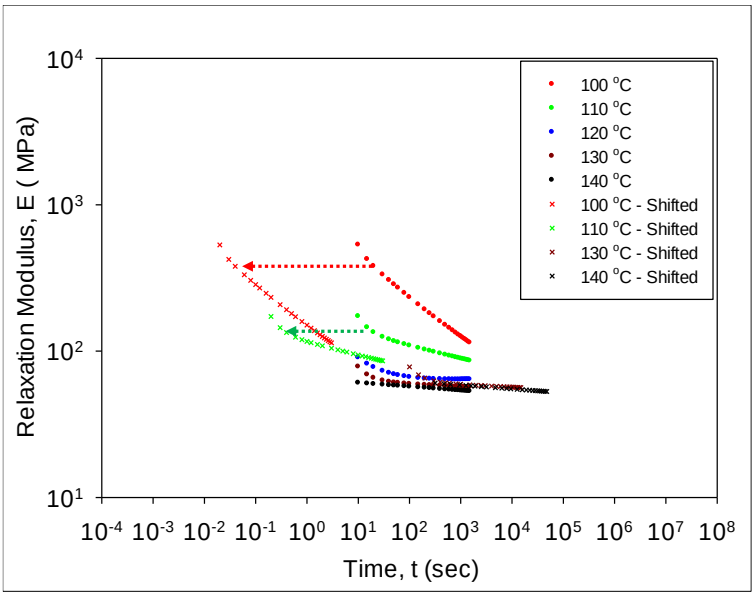

Figure 5-26 Horizontally shifted the curve for generating master curve at a reference temperature of 120 °C

Table 5-3 Calculated shift factor

Shift Factors		
Temperature (^{o}C)	a(T)	$Log_{10}a(T)$
100	501.18	2.7
110	50.12	1.7
120	1	0
130	0.1	-1
140	0.032	-1.5

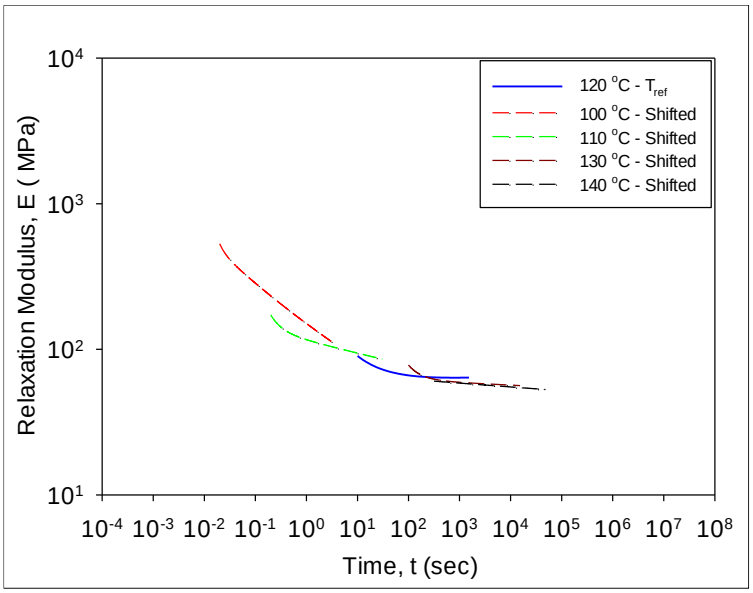

Figure 5-27 Shifted curve to reference temperature of 120 °C

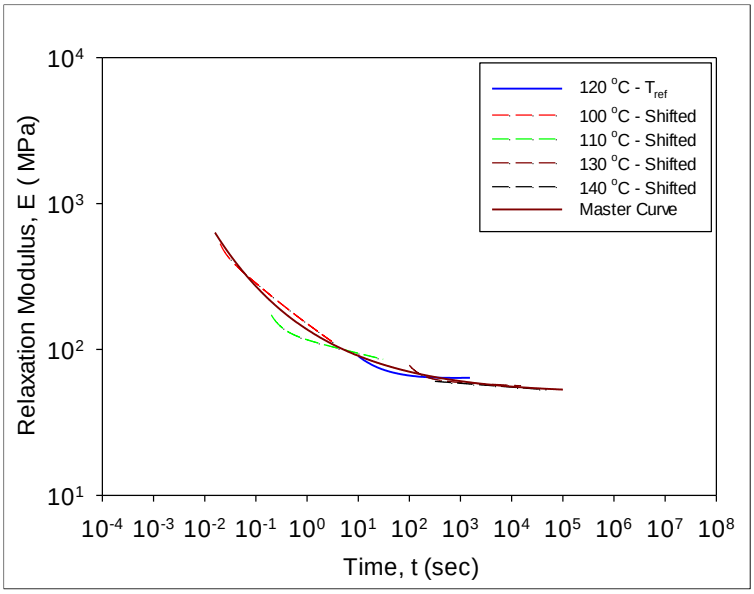

Figure 5-28 Master curve generated at a reference temperature of 120 °C

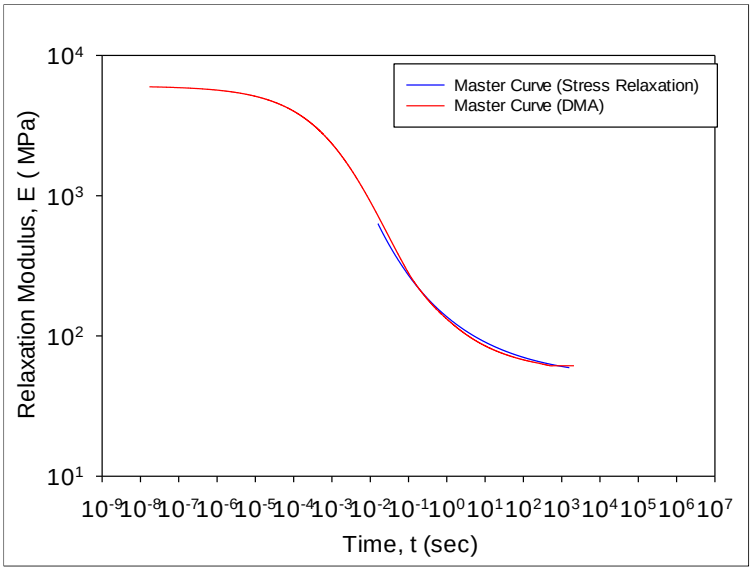

Figure 5-29 Comparison between generated master curve using DMA and stress relaxation test

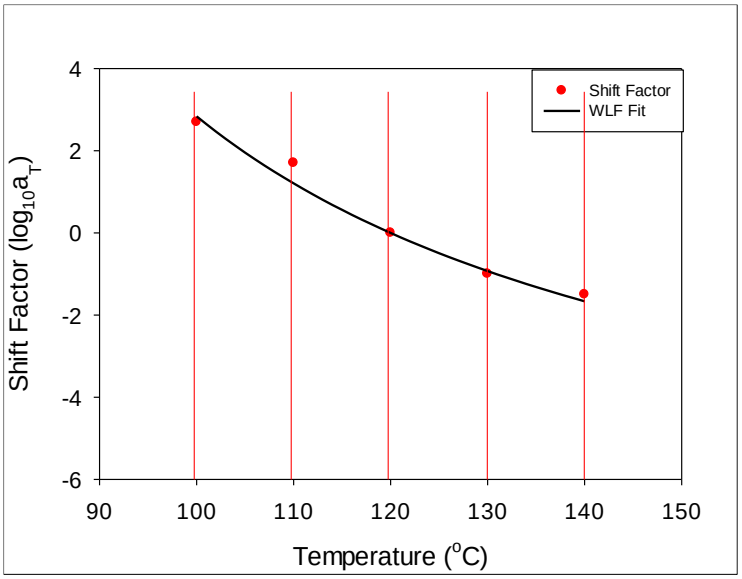

Figure 5-30 Calculated Shift factor

Table 5-4 Calculated Prony pairs at a reference temperature of 120 °C

Constants for Shear Response	Constants for Volumetric Response	Constants for Shift Function (Williams-Landel-Ferry (WLF) Equation)
$\alpha_1 = 1.47 \times 10^{-1}$ $\tau_1 = 1.12 \times 10^{-3}$ $\alpha_2 = 3.27 \times 10^{-2}$ $\tau_2 = 8.93 \times 10^{-3}$ $\alpha_3 = 2.04 \times 10^{-2}$ $\tau_3 = 7.87 \times 10^{-2}$ $\alpha_4 = 3.89 \times 10^{-3}$ $\tau_4 = 1.16 \times 10^{0}$ $\alpha_5 = 5.56 \times 10^{-3}$ $\tau_5 = 2.40 \times 10^{1}$ $\alpha_6 = 2.06 \times 10^{-3}$ $\tau_6 = 3.52 \times 10^{4}$ $\alpha_7 = 8.33 \times 10^{-4}$ $\tau_7 = 2.92 \times 10^{6}$	$\alpha_1 = 1.47 \times 10^{-1}$ $\tau_1 = 1.12 \times 10^{-3}$ $\alpha_2 = 3.27 \times 10^{-1}$ $\tau_2 = 8.93 \times 10^{-3}$ $\alpha_3 = 2.04 \times 10^{-2}$ $\tau_3 = 7.87 \times 10^{-2}$ $\alpha_4 = 3.89 \times 10^{-3}$ $\tau_4 = 1.16 \times 10^{0}$ $\alpha_5 = 5.56 \times 10^{-3}$ $\tau_5 = 2.40 \times 10^{1}$ $\alpha_6 = 2.06 \times 10^{-3}$ $\tau_6 = 3.52 \times 10^{4}$ $\alpha_7 = 8.33 \times 10^{-4}$ $\tau_7 = 2.92 \times 10^{6}$	$T_{ref} = 120$ $C_1 = -13.66$ $C_2 = -54.47$

Table 5-4 showed the calculated Prony pairs and using this Prony pair's finite element modeling were done. Experimental stress strain test were performed at different temperature from -55 to 125 °C which are shown in Figure 5-31. Finite element modeling was performed using Ansys which were used to do predict tensile and creep behavior. (Figure 5-32 and Figure 5-33)

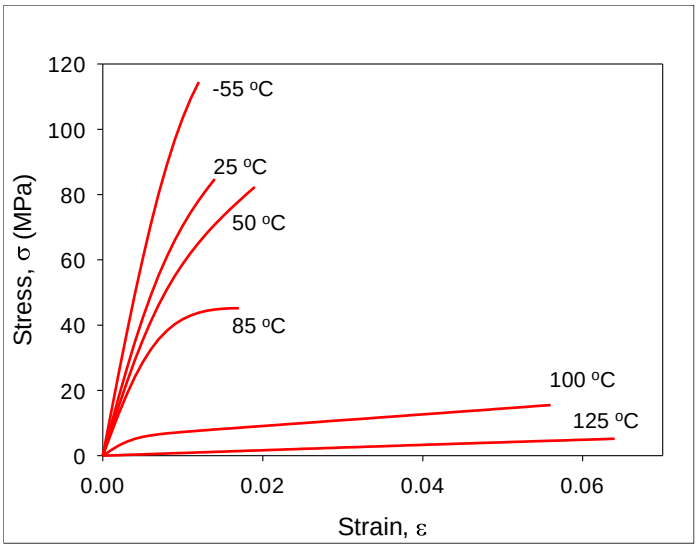

Figure 5-31 Stress Strain test at different temperatures between -55 °C to 125 °C

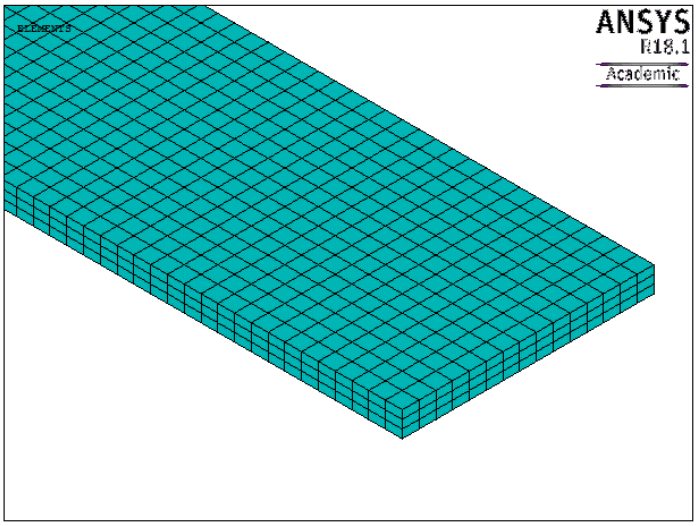

Figure 5-32 Finite element modeling for stress strain and creep test

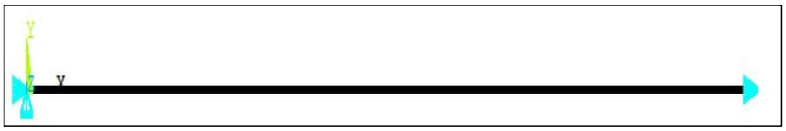

Tensile

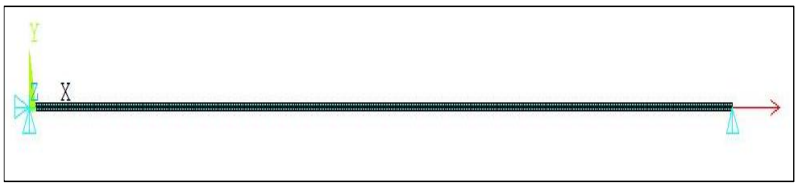

Creep

Figure 5-33 Boundary conditions for Tensile and Creep test

Using the calculated Prony pairs tensile and creep tests were simulated in Ansys. A 7 Prony pair predicted the behavior of stress strain (Figure 5-34). By performing trial and error, we have found that 17 Prony pairs predicted the behavior fairly well for stress strain results (Figure 5-36). Also, this 17 Prony pairs were also used to predict the behavior of creep test at different stress level and temperatures (Figure 5-37 to Figure 5-40). The Prony pairs were provided in Table 5-5 to Table 5-7. A higher no of Prony pairs predicted the stress strain and creep behavior better compare to lower no of Prony pairs.

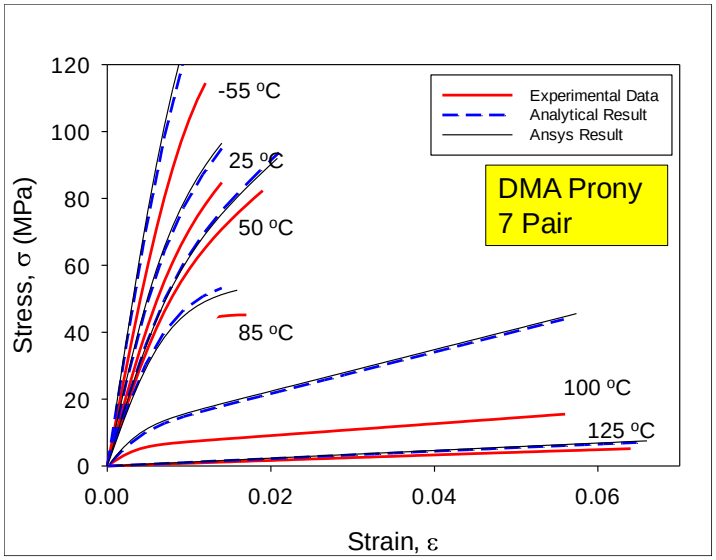

Figure 5-34 Comparison between experimental and finite element modeling using 7 Prony pairs for shear and bulk modulus from DMA experiment

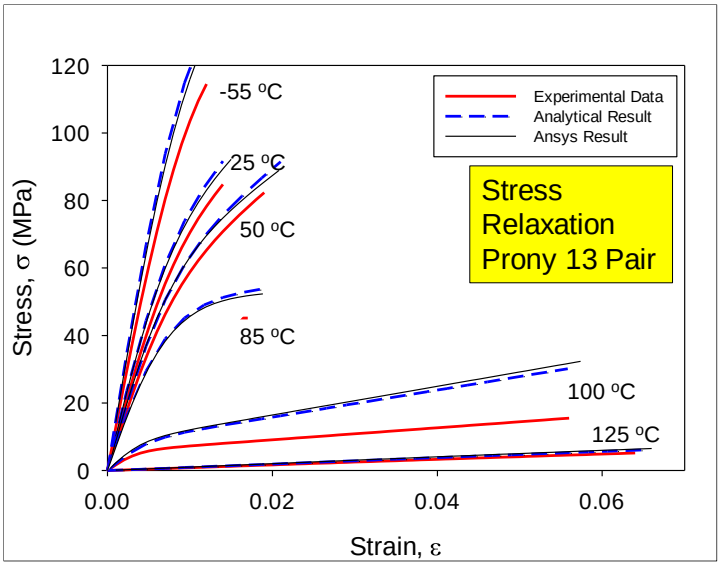

Figure 5-35 Comparison between experimental and finite element modeling using 13 Prony pairs for shear and bulk modulus from stress relaxation test data

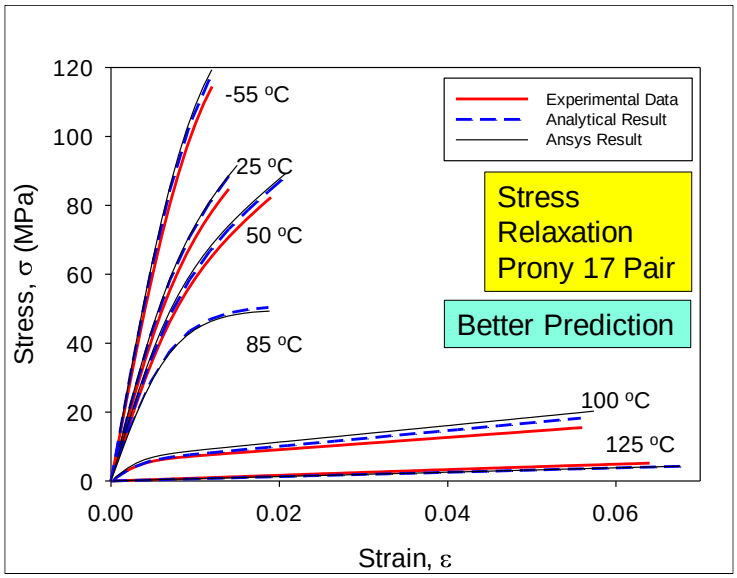

Figure 5-36 Comparison between experimental and finite element modeling using 17 Prony pairs for shear and bulk modulus from stress relaxation test data

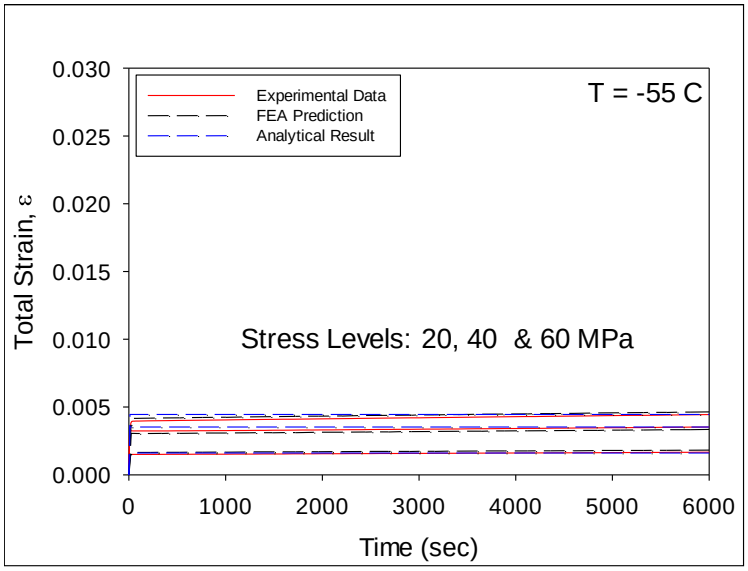

Figure 5-37 Comparison between experimental and finite element modeling using 17 Prony pairs from stress relaxation test data at -55 °C

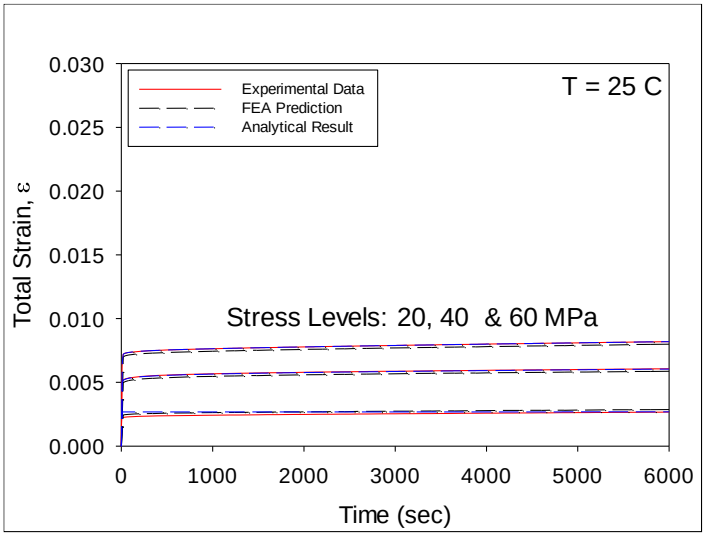

Figure 5-38 Comparison between experimental and finite element modeling using 17 Prony pairs from stress relaxation test data at 25 °C

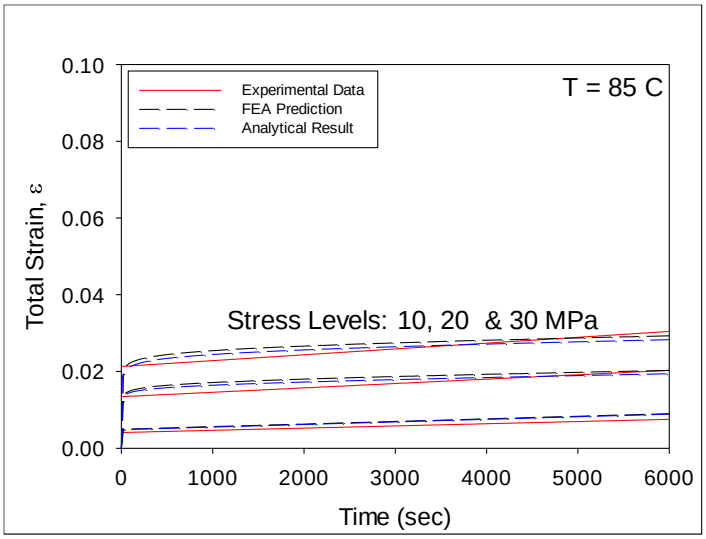

Figure 5-39 Comparison between experimental and finite element modeling using 17 Prony pairs from stress relaxation test data at 85 °C

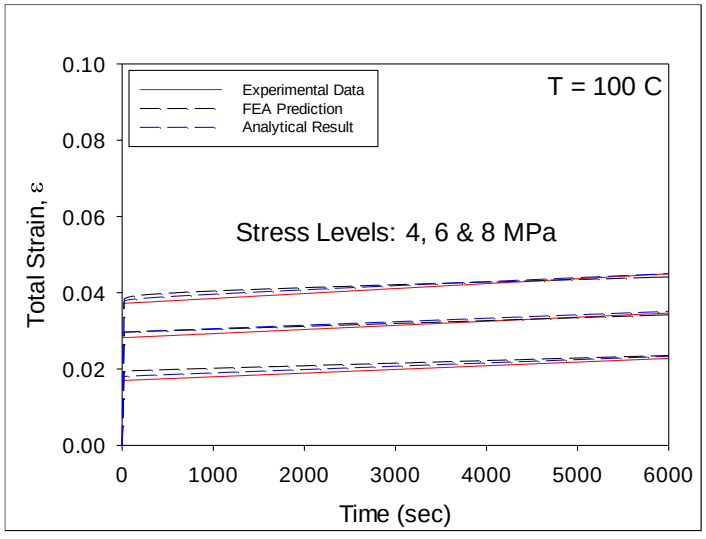

Figure 5-40 Comparison between experimental and finite element modeling using 17 Prony pairs from stress relaxation test data at 100 °C

Table 5-5 Calculated 13 Prony pairs from Stress relaxation test

Constants for Shear Response (13 Pair)			Constants for Volumetric Response (13 Pair)			Constants for Shift Function (Williams-Landel-Ferry (WLF) Equation)
i	τ_i (sec)	Relative Moduli, α_i	i	τ_i (sec)	Relative Moduli, α_i	T_{ref} = 120 C_1 = -12.28 C_2 = -44.93
1	4.33×10^{-4}	5.50×10^{-1}	1	4.33×10^{-4}	5.50×10^{-1}	
2	2.10×10^{-3}	3.91×10^{-2}	2	2.10×10^{-3}	3.91×10^{-2}	
3	9.57×10^{-3}	2.43×10^{-2}	3	9.57×10^{-3}	2.43×10^{-2}	
4	6.65×10^{-2}	1.89×10^{-2}	4	6.65×10^{-2}	1.89×10^{-2}	
5	1.08×10^{0}	3.82×10^{-3}	5	1.08×10^{0}	3.82×10^{-3}	It is Recommended That Glass Transition Temperature Should be Used as Reference Temperature ($T_{ref} = T_g$)
6	1.84×10^{1}	4.48×10^{-3}	6	1.84×10^{1}	4.48×10^{-3}	
7	9.90×10^{1}	9.29×10^{-4}	7	9.90×10^{1}	9.29×10^{-4}	
8	1.00×10^{5}	1.87×10^{-3}	8	1.00×10^{5}	1.87×10^{-3}	
9	1.00×10^{6}	3.77×10^{-4}	9	1.00×10^{6}	3.77×10^{-4}	Calculated Using Stress Relaxation Test Data From Ansys
10	1.00×10^{9}	3.28×10^{-54}	10	1.00×10^{9}	3.28×10^{-54}	
11	1.00×10^{10}	2.03×10^{-13}	11	1.00×10^{10}	2.03×10^{-13}	
12	1.00×10^{12}	6.33×10^{-4}	12	1.00×10^{12}	6.33×10^{-4}	
13	1.00×10^{14}	2.91×10^{-3}	13	1.00×10^{14}	2.91×10^{-3}	

Table 5-6 Calculated 17 Prony pairs from Stress relaxation tests

Constants for Shear Response (17 Pair)						Constants for Shift Function (Williams-Landel-Ferry (WLF) Equation)
i	τ_i (sec)	Relative Moduli, α_i	i	τ_i (sec)	Relative Moduli, α_i	T_{ref} = 120 C_1 = -12.20 C_2 = -44.42
1	2.71×10^{-5}	2.04×10^{-2}	10	1.00×10^{6}	3.92×10^{-4}	
2	4.41×10^{-4}	5.08×10^{-1}	11	1.00×10^{9}	5.62×10^{-54}	
3	2.20×10^{-3}	3.82×10^{-2}	12	1.00×10^{10}	8.49×10^{-10}	
4	1.00×10^{-2}	2.35×10^{-2}	13	1.00×10^{12}	5.58×10^{-4}	
5	6.60×10^{-2}	1.82×10^{-2}	14	1.00×10^{14}	2.88×10^{-3}	
6	9.59×10^{-1}	3.93×10^{-3}	15	1.00×10^{15}	1.82×10^{-4}	It is Recommended That Glass Transition Temperature Should be Used as Reference Temperature (T_{ref} =T_g)
7	1.63×10^{1}	4.40×10^{-3}	16	1.00×10^{16}	3.35×10^{-4}	
8	9.30×10^{1}	1.14×10^{-3}	17	1.00×10^{17}	3.58×10^{-4}	
9	1.00×10^{5}	1.83×10^{-3}				Calculated Using Stress Relaxation Test Data From Ansys

Table 5-7 Calculated 17 Prony pairs from Stress relaxation tests

Constants for Volumetric Response (17 Pair)						Constants for Shift Function (Williams-Landel-Ferry (WLF) Equation)
i	τ_i (sec)	Relative Moduli, α_i	i	τ_i (sec)	Relative Moduli, α_i	T_{ref} = 120 C_1 = -12.20 C_2 = -44.42
1	2.71×10^{-5}	2.04×10^{-2}	10	1.00×10^{6}	3.92×10^{-4}	
2	4.41×10^{-4}	5.08×10^{-1}	11	1.00×10^{9}	5.62×10^{-54}	
3	2.20×10^{-3}	3.82×10^{-2}	12	1.00×10^{10}	8.49×10^{-10}	
4	1.00×10^{-2}	2.35×10^{-2}	13	1.00×10^{12}	5.58×10^{-4}	
5	6.60×10^{-2}	1.82×10^{-2}	14	1.00×10^{14}	2.88×10^{-3}	
6	9.59×10^{-1}	3.93×10^{-3}	15	1.00×10^{15}	1.82×10^{-4}	It is Recommended That Glass Transition Temperature Should be Used as Reference Temperature (T_{ref} =T_g)
7	1.63×10^{1}	4.40×10^{-3}	16	1.00×10^{16}	3.35×10^{-4}	
8	9.30×10^{1}	1.14×10^{-3}	17	1.00×10^{17}	3.58×10^{-4}	
9	1.00×10^{5}	1.83×10^{-3}				Calculated Using Stress Relaxation Test Data From Ansys

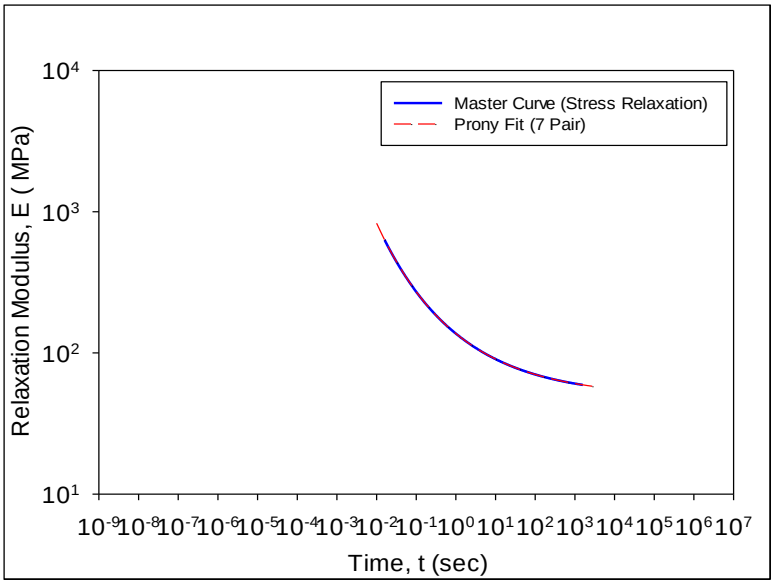

Figure 5-41 Stress Relaxation master curve fitting using 7 Prony Pair

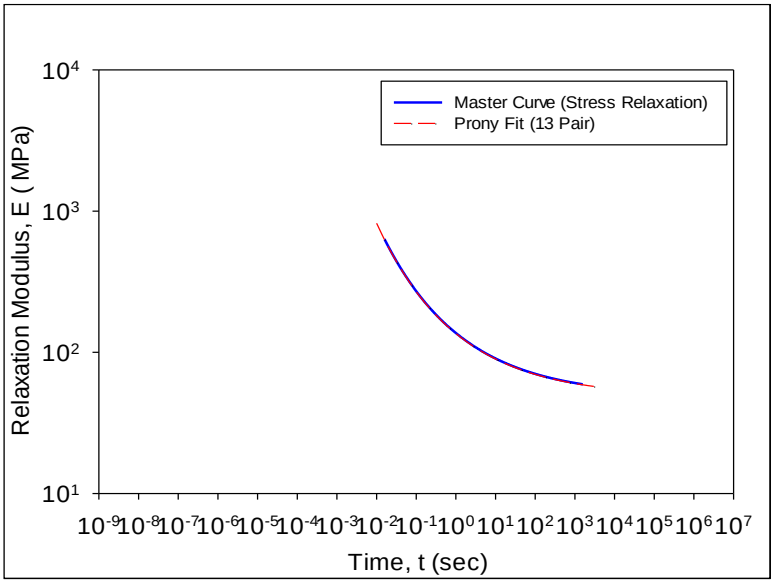

Figure 5-42 Stress Relaxation master curve fitting using 13 Prony Pair

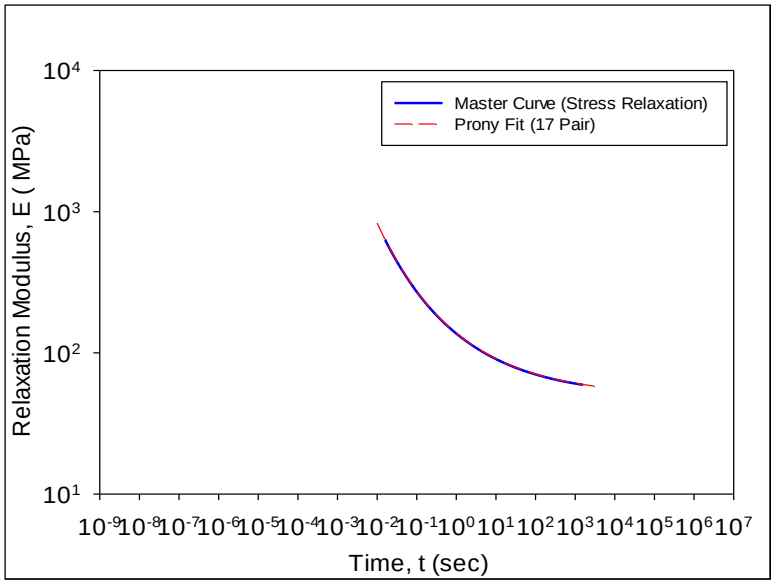

Figure 5-43 Stress Relaxation master curve fitting using 17 Prony Pair

Stress relaxation master curve data has been fitted with the calculated different Prony pair. Figure 5.41, 5.42 and 5.43 showed the Prony fit for 7 pair, 13 pair and 17 pair respectively. These Prony pair smoothly fitted the stress relaxation master curve for a wide range of time domain.

5.7 Summary and Discussion

In this work, we have characterized a commercially available underfill viscoelastic material behavior using dynamic mechanical analyzer and performing stress relaxation test. Master curve has been generated and WLF shift function has been calculated for both cases. We have also determined the Prony series parameters for shear and bulk response. By performing the stress relaxation test at different temperatures, we have generated the master

curve and WLF shift parameters. Also, Prony pairs have been determined and it is found that the higher no of Prony pairs better predict the stress strain and creep behavior compare to lower Prony pairs.

Viscoelastic properties are important to predict the solder joint life prediction in flip chip assembly, warpage analysis. By using the right input parameter for underfill material in FE analysis, the failure behavior can be correctly estimated. Moreover, package size is getting smaller day by day, and viscoelastic material like underfill, mold compound play important role in reliability. In this study, we have shown that a higher number of Prony pairs is required to get the proper viscoelastic regime. However, most of the time researchers assume smaller no of Prony pairs to reduce the simulation time but, for a better and reliable study higher no of viscoelastic parameters should be used.

CHAPTER 6

MODELING OF UNDERFILLED BGA ASSEMBLIES USING BOTH VISCOELASTIC AND ELASTIC MATERIAL PROPERTIES

6.1 Introduction

The main goal of this chapter was to research on the influence of viscoelastic parameter of underfill on reliability of solder joint in actual assemblies. The overall objective was to determine solder joint fatigue life using elastic and viscoelastic parameter of underfill and observe the variation in predicted solder joint life. A systematic approach has been described on how to determine viscoelastic Prony parameter of a typical underfill material. Prony parameters have been used in the finite element models of underfilled ball grid array packages (Ultra CSP) subjected to thermal cycling from -40 to 125 ^{o}C. Traditional finite element based predictions for solder joint reliability during thermal cycling accelerated life testing are based on solder constitutive equations (e.g. Anand viscoplastic model and failure models (e.g. Darveaux energy dissipation per cycle model.

Finite element modeling using viscoelastic underfill were performed for three different package. Three packages are:

a) No Underfill (NF)

b) Elastic Property of Underfill (ET)

c) Viscoelastic Property of Underfill (VE)

6.2 Finite Element Modeling

Due to the coefficient of thermal expansion mismatch between die and substrate, significant stress is generated. Silicon die has lower CTE compared to substrate. During thermal cycling, stress developed due to CTE mismatch and which leads to failure after certain thermal cycle. Deformation due to CTE mismatch are shown in Figure 6-1.

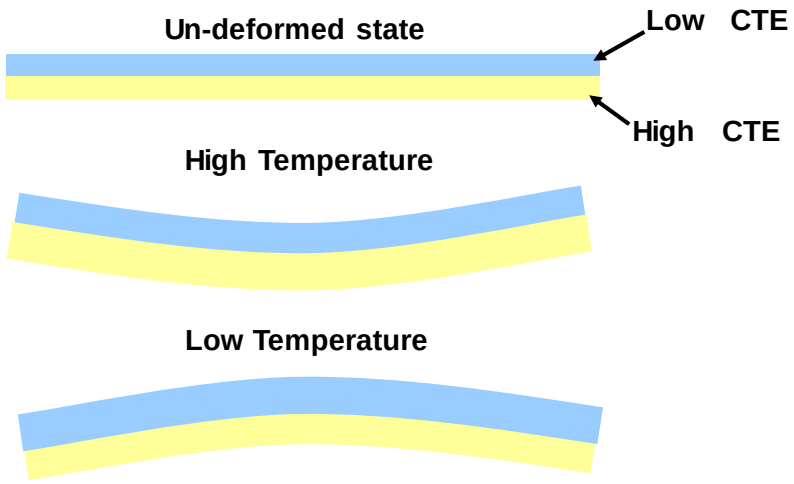

Figure 6-1 Deformation due to CTE mismatch

For solder joint reliability, prediction of life based on two items. The first one is selection of fatigue model which determines life based on assumptions made on crack initiation/growth with material response, and second one is selection of constitutive model, which determines the inclusion of inelastic, rate-dependent, and temperature-dependent effects.

There are different types of failure happens in solder joint. For example, failure can occur at interfaces such bump/pad interface, or failure may occur within the solder bulk.

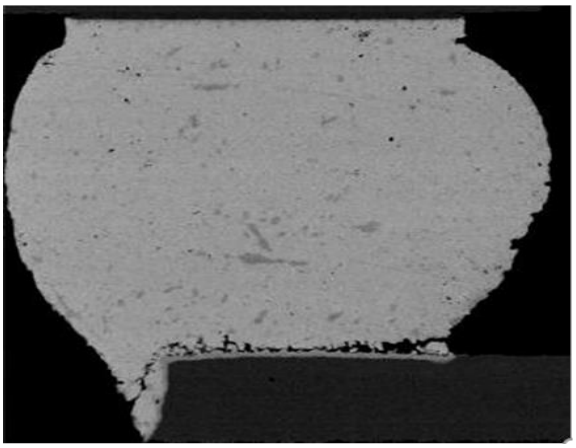

Figure 6-2 Interfacial Failure in Solder Joint

Interface and intergranular fracture are usually treated differently. Interfacial failure is more common (Figure 6-2). For solder life prediction, assumptions are made on crack initiation and propagation. Crack size or life are related to other parameters that can be readily calculated, such as plastic work or strain. By calculating plastic strain or work using FEA analysis, solder joint fatigue life can be estimated. Inelastic strain (or sometimes referred to as creep strain or plastic strain) is the irrecoverable strain that develops. This accumulated inelastic strain is an always increasing quantity. Plastic work (or creep strain energy) is the energy associated with this inelastic strain (Figure 6-3).

$$E_{pl} = \int \sigma \times \varepsilon_{pl} dV \tag{6.1}$$

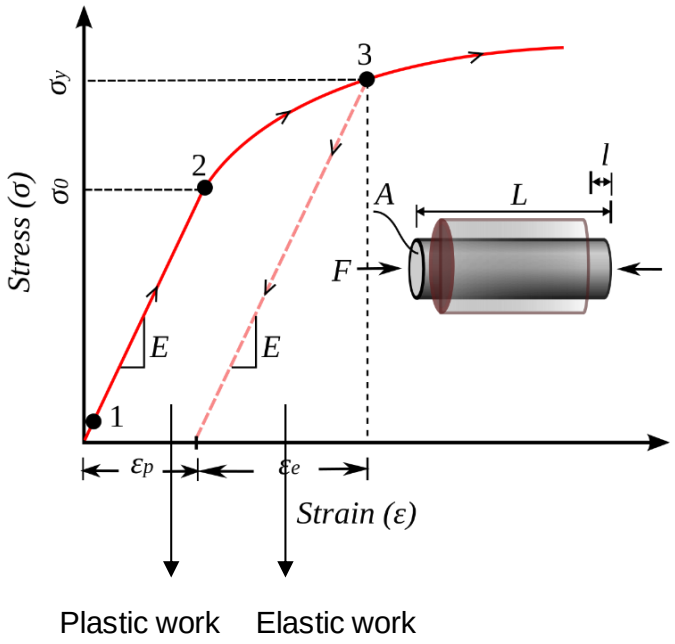

Figure 6-3 Plastic Work

where σ is generated stress and ε_{pl} is plastic strain.

There are various approaches of where to calculate life, but the two common approaches are using volume averaged approach, where a region is selected and determine a volume averaged quantity for life calculation, and another is the damage model approach, where "damage" is a quantity based on inelastic strain or plastic work that is calculated at each element (or integration point) to predict failure (Figure 6-4).

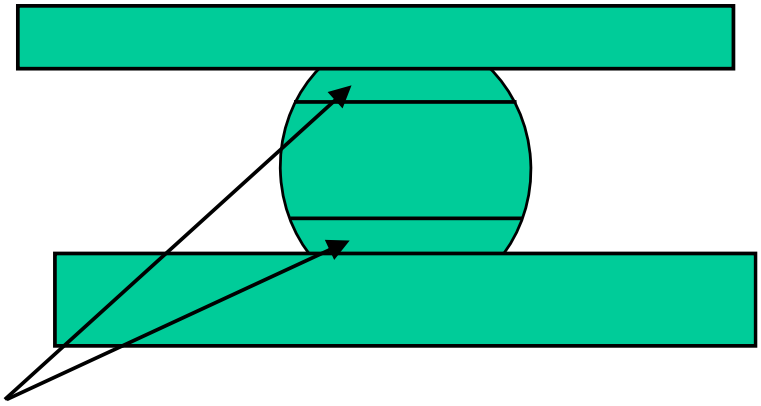

Figure 6-4 Possible failure regions. Volume Averaging done within this to Predict Time to Failure

In this study, the volume averaging technique was used to predict life. Darveaux [78] has presented energy dissipation based models for life prediction in solder joints subjected to cyclic loading. The approach consists of separate power law type relations for estimating crack initiation and crack growth rate in solder joints:

$$N_i = K_1 (\Delta W)^{K_2} \tag{6.2}$$

$$\frac{da}{dN} = K_3 (\Delta W)^{K4} \tag{6.3}$$

where N_i is the number cycles to crack initiation, da/dN is the crack growth rate (assumed constant) occurring after crack initiation, ΔW is the energy dissipation per cycle in the solder sample (e.g. critical solder ball), and K_1, K_2, K_3, and K_4 are fitting constants. Once the crack location and path are known in the solder joint, the number of cycles to failure can be estimated using:

$$N_f = N_i + \frac{a_c}{\left[\frac{da}{dN}\right]} \tag{6.4}$$

where N_f is the number of cycles to failure, a_c is the length of the fully developed crack at failure/fracture, and N_i and da/dN are calculated from ΔW using equations (6.2-6.3).

Since relating inelastic strain or plastic work to fatigue is a common approach, the next thing to consider is the constitutive law to model this inelastic behavior. Fatigue methods used in solder joint reliability related crack growth (damage) to inelastic strain/work. By knowing the amount of plastic work or inelastic strain, we may predict cycles to failure. Consequently, the choice of the constitutive model is closely tied with the fatigue model. With nonlinear constitutive models, rate-dependency - time effects are important (i.e., dependence on ramp/dwell times), temperature-dependency - dealing with a thermally-activated process, so temperature is included via Arrhenius equation, existence of yield surface are typically considered for solder joint simulations. Anand's viscoplastic constitutive model have been widely used to model solder and in this study we have used this model. The procedure to predict solder joint reliability can be depicted using the following Figure 6-5.

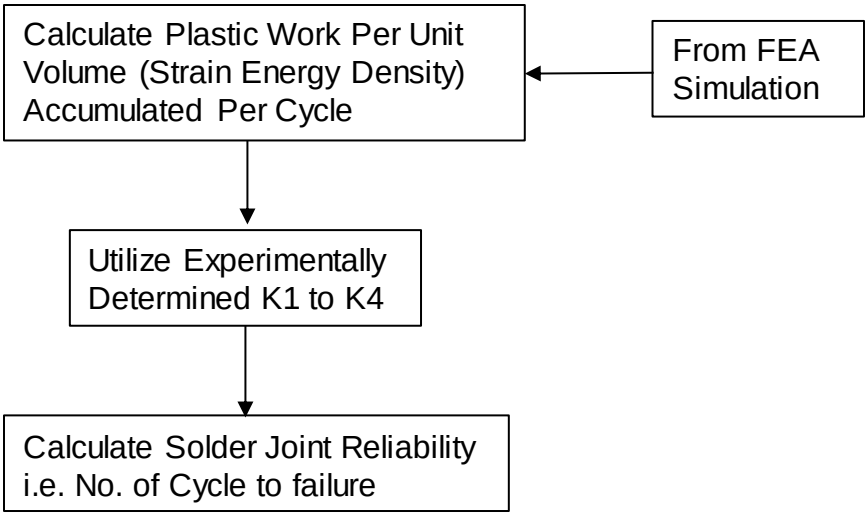

Figure 6-5 Solder joint fatigue life prediction method

6.3 Loads and Boundary Conditions

For modeling of thermal cycling, the following thermal profile has been used based on JEDEC standard (JESD22-A104D) between T = -40 to 125 ^{o}C. Figure 6-6 shows the applied temperature history consisting of 1-hour (60 minutes) temperature cycles, which featured ramp and dwell times of 15 minutes each. The package assembly is assumed to be in a stress-free state at 25 ^{o}C (room temperature). Material properties for different components are listed in Table 6-2. Anand viscoplastic constitutive parameters are used for SAC305 solder given in Table 6-1 [101]. Temperature dependent elastic properties are given in Table 6-3 and a FEA analysis was performed using these parameters.

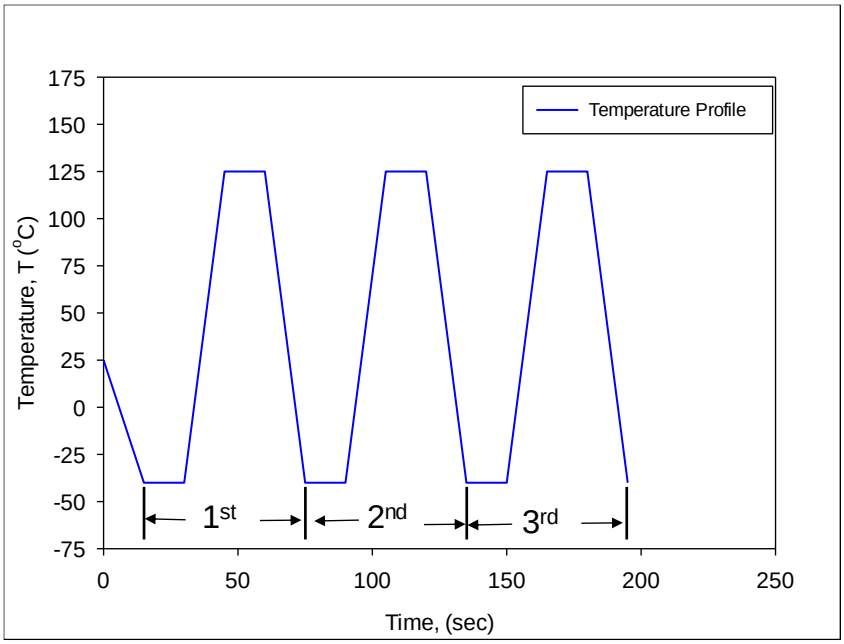

Figure 6-6 Temperature Profile of Thermal Cycling

Table 6-1 SAC 305 Anand Viscoplastic Coefficient

Constant Number	Anand Constant	Units	SAC 305
1	s_o	MPa	21.0
2	Q/R	1/K	9320
3	A	sec^{-1}	3501
4	ξ	Dimensionless	4
5	m	Dimensionless	0.25
6	h_o	MPa	180000
7	$\hat{s}$	MPa	30.2
8	n	Dimensionless	0.0100
9	a	Dimensionless	1.78

Table 6-2 Material Properties of Different Components

Material	**Elastic Modulus (GPa)**	**Shear Modulus (GPa)**	**Poisson's Ratio**	**CTE [1/K]**
Solder Ball	Anand Model	Anand Model	0.30	24.5×10^{-6}
Copper	129	-	0.34	16.3×10^{-6}
Silicon Die	163	-	0.28	2.5×10^{-6}
BT Substrate	17.89 (xy)	8.06 (xy)	0.11 (xy)	12.4×10^{-6} (xy)
	7.85 (z)	2.82 (xz ; yz)	0.39 (xz ; yz)	57.0×10^{-6} (z)
Underfill	Viscoelastic Prony Parameter			

Table 6-3 Temperature Dependent Underfill Elastic

Temperature T (^{o}C)	Initial Elastic Modulus E (GPa)	Ultimate Stress (MPa)	Ultimate Strain
-55	12.71	100.54	0.010
25	9.18	83.30	0.015
50	7.75	78.33	0.019
85	6.64	45.19	0.017
100	1.33	17.59	0.075
125	0.08	5.14	0.056

Table 6-4 Prony Coefficients for Shear Response

Constants for Shear Response						Constants for Shift Function (Williams-Landel-Ferry (WLF) Equation)
i	τ_i (sec)	Relative Moduli, α_i	i	τ_i (sec)	Relative Moduli, α_i	T_{ref} = 120
1	2.71×10^{-5}	2.04×10^{-2}	10	1.00×10^{6}	3.92×10^{-4}	C_1 = -12.20
2	4.41×10^{-4}	5.08×10^{-1}	11	1.00×10^{9}	5.62×10^{-54}	C_2 = -44.42
3	2.20×10^{-3}	3.82×10^{-2}	12	1.00×10^{10}	8.49×10^{-10}	
4	1.00×10^{-2}	2.35×10^{-2}	13	1.00×10^{12}	5.58×10^{-4}	
5	6.60×10^{-2}	1.82×10^{-2}	14	1.00×10^{14}	2.88×10^{-3}	
6	9.59×10^{-1}	3.93×10^{-3}	15	1.00×10^{15}	1.82×10^{-4}	
7	1.63×10^{1}	4.40×10^{-3}	16	1.00×10^{16}	3.35×10^{-4}	
8	9.30×10^{1}	1.14×10^{-3}	17	1.00×10^{17}	3.58×10^{-4}	
9	1.00×10^{5}	1.83×10^{-3}				

Table 6-5 Prony Coefficients for Bulk Response

Constants for Volumetric Response						Constants for Shift Function (Williams-Landel-Ferry (WLF) Equation)
i	τ_i (sec)	Relative Moduli, α_i	i	τ_i (sec)	Relative Moduli, α_i	T_{ref} = 120
1	2.71×10^{-5}	2.04×10^{-2}	10	1.00×10^{6}	3.92×10^{-4}	C_1 = -12.20
2	4.41×10^{-4}	5.08×10^{-1}	11	1.00×10^{9}	5.62×10^{-54}	C_2 = -44.42
3	2.20×10^{-3}	3.82×10^{-2}	12	1.00×10^{10}	8.49×10^{-10}	
4	1.00×10^{-2}	2.35×10^{-2}	13	1.00×10^{12}	5.58×10^{-4}	
5	6.60×10^{-2}	1.82×10^{-2}	14	1.00×10^{14}	2.88×10^{-3}	
6	9.59×10^{-1}	3.93×10^{-3}	15	1.00×10^{15}	1.82×10^{-4}	
7	1.63×10^{1}	4.40×10^{-3}	16	1.00×10^{16}	3.35×10^{-4}	
8	9.30×10^{1}	1.14×10^{-3}	17	1.00×10^{17}	3.58×10^{-4}	
9	1.00×10^{5}	1.83×10^{-3}				

6.4 Package Design

A three dimensional finite element analysis has been used to calculate accumulated plastic work in the chip scale package (CSP) type package (Ultra CSP). A 15 x 15 mm substrate was used, and the die/package size was 10 x 10 mm. SAC 305 interconnections were used, and the total number of balls was 144 with a pitch of 0.8 mm. Figure 6-7 shows the isometric view of the package and cross sectional view are shown in Figure 6-8.

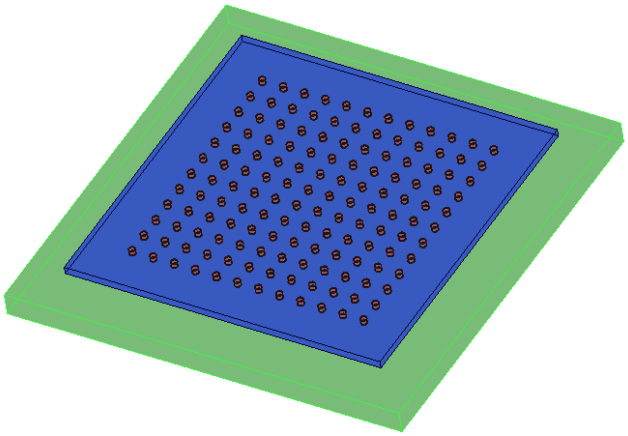

Figure 6-7 Package

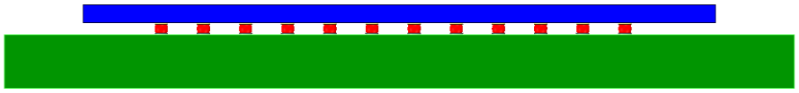

Figure 6-8 Cross section of Chip Scale Package (Ultra CSP)

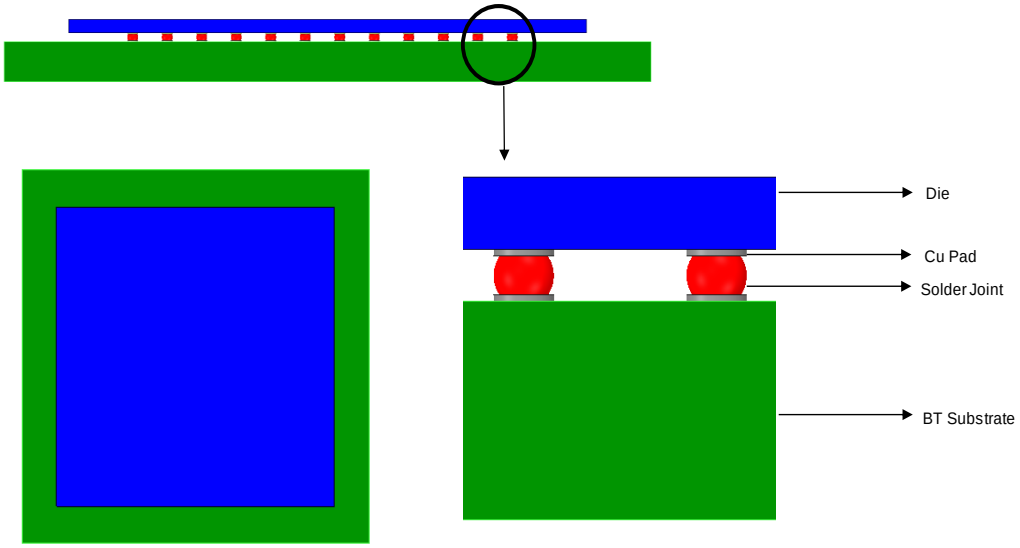

Figure 6-9 Chip Scale Package cross-section

Here, package die, copper pad and BT substrate thicknesses were 0.28, 0.025, and 0.84 mm, respectively. The ball diameter was 0.25 mm. In the Figure 6-9 , die, copper pad, solder ball, BT substrate were represented with blue, grey, red and green color respectively.

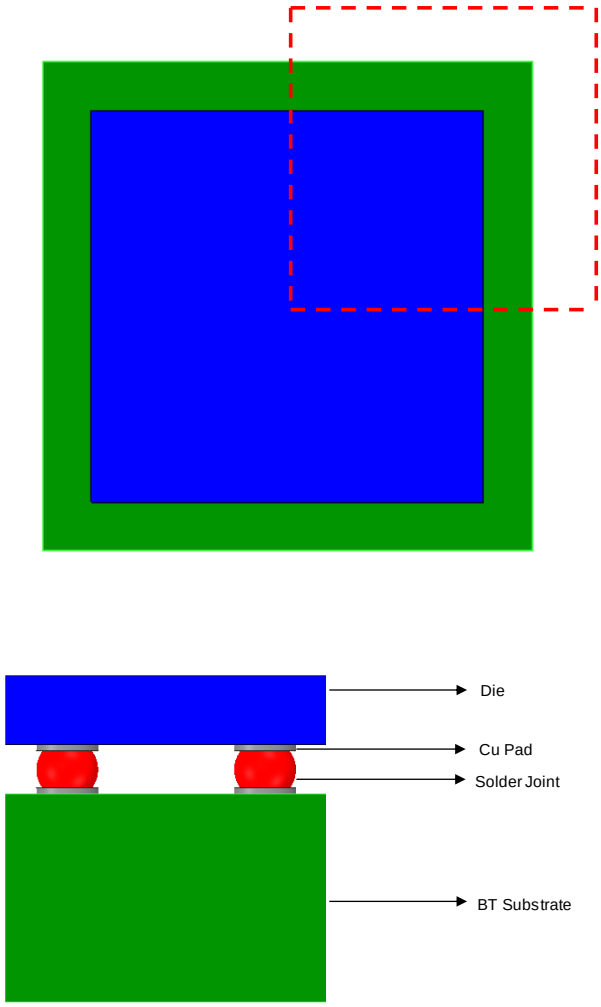

Figure 6-10 Chip Scale Package cross-section

This package was meshed using Solid185 elements. Due to symmetry, a quarter symmetry model were used for FEA analysis. A quarter model without underfill is given in Figure 6-11. Solder array and single solder ball are listed in Figure 6-12. Sub-modeling technique has been used for fine meshing in critical solder ball Figure 6-13. The critical solder ball was found at the corner ball and the contours of plastic work are shown in Figure

6-14. Using the sub modeling, fine meshing was performed in the region of interest to get better result. The package assembly was assumed to be in a stress-free state at 25 ^{o}C (room temperature), with no initial residual stresses/deformations induced in the manufacturing process. After the cool down from 25 ^{o}C to -40 ^{o}C, three thermal cycles were simulated. In all of the models, it was found that the cycle to cycle variation of the solder stress/strain behavior became stable by the third cycle. The values during the third cycle were extracted to evaluate the dissipated plastic work per cycle (ΔW) that was used to predict fatigue life.

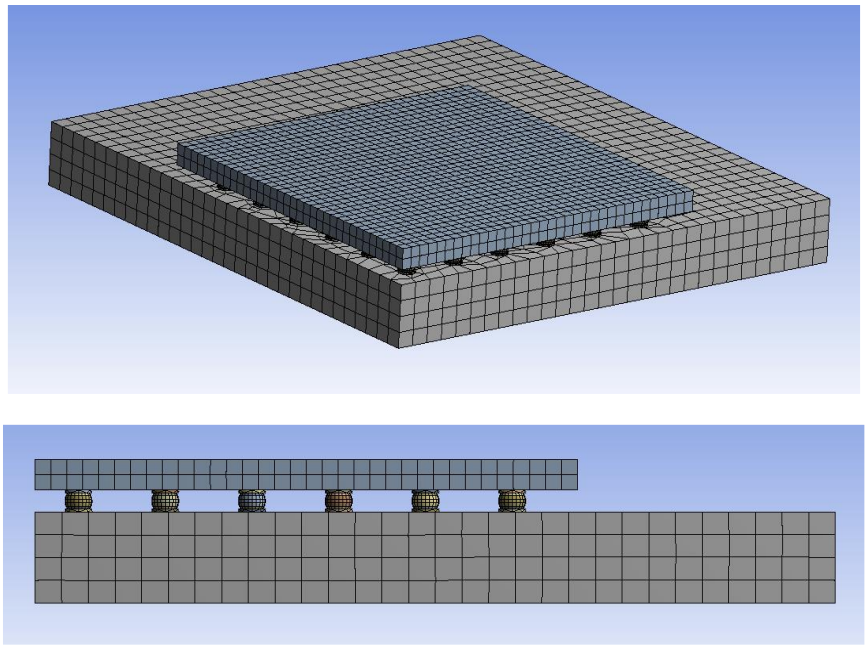

Figure 6-11 FEA Mesh for Quarter Model (without Underfill)

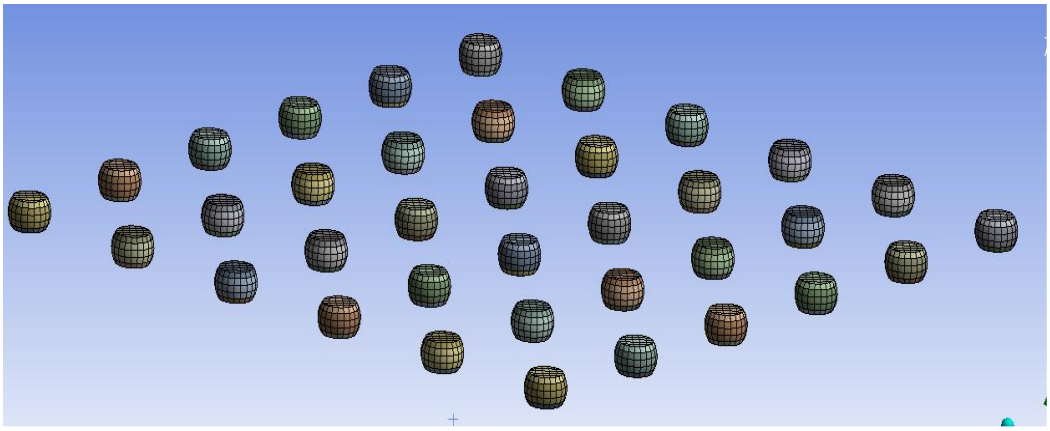

Figure 6-12 FEA Mesh for the Solder Balls

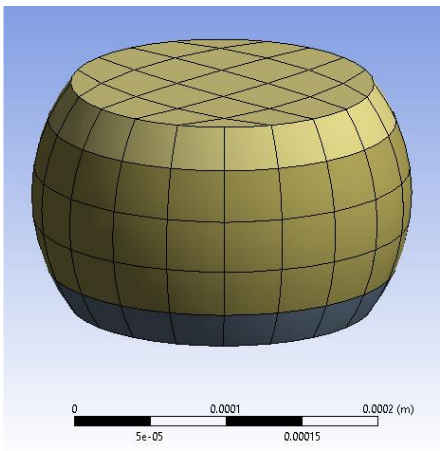

Single Solder Ball

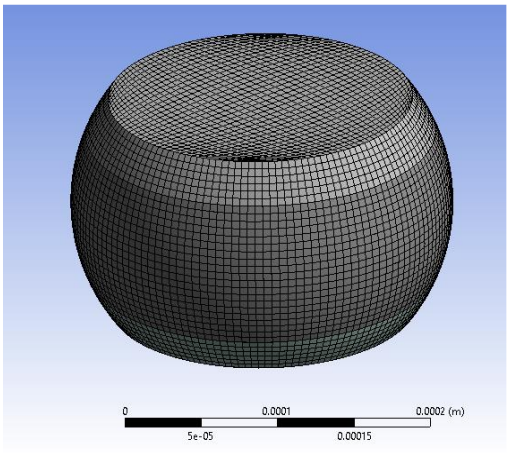

Sub-modeling for Critical Solder Ball

Figure 6-13 FEA Mesh for the Solder Balls

6.5 FEA Results

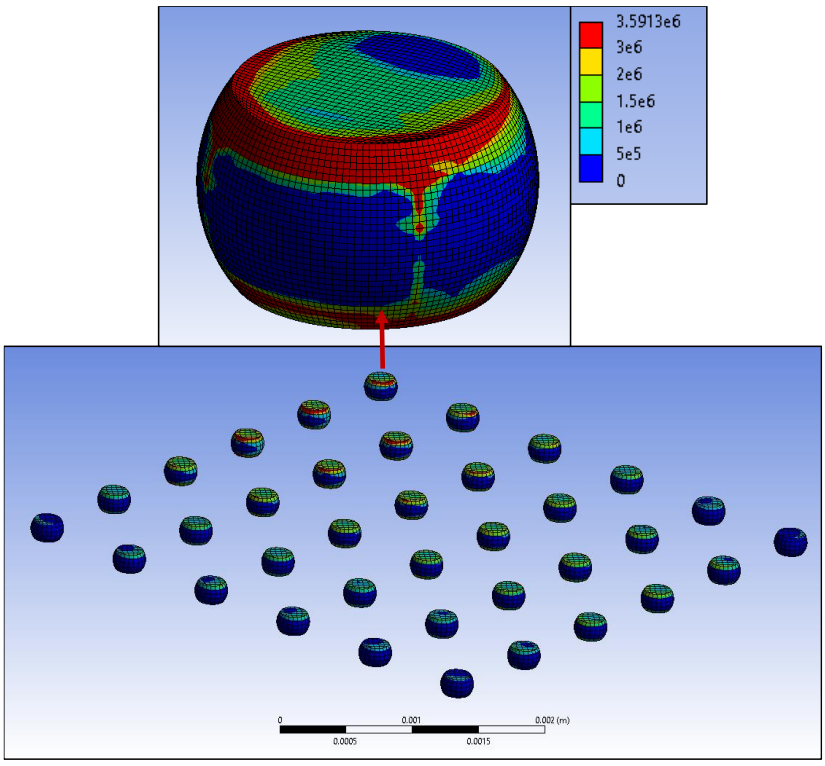

Figure 6-14 Contours of Accumulated Plastic Work (MPa) without underfill

The quarter model mesh with underfill is given in Figure 6-15. Two types of simulation has been performed based on elastic and viscoelastic material properties of underfill. Contour with elastic and viscoelastic underfill material are given in Figure 6-16 and Figure 6-17 respectively.

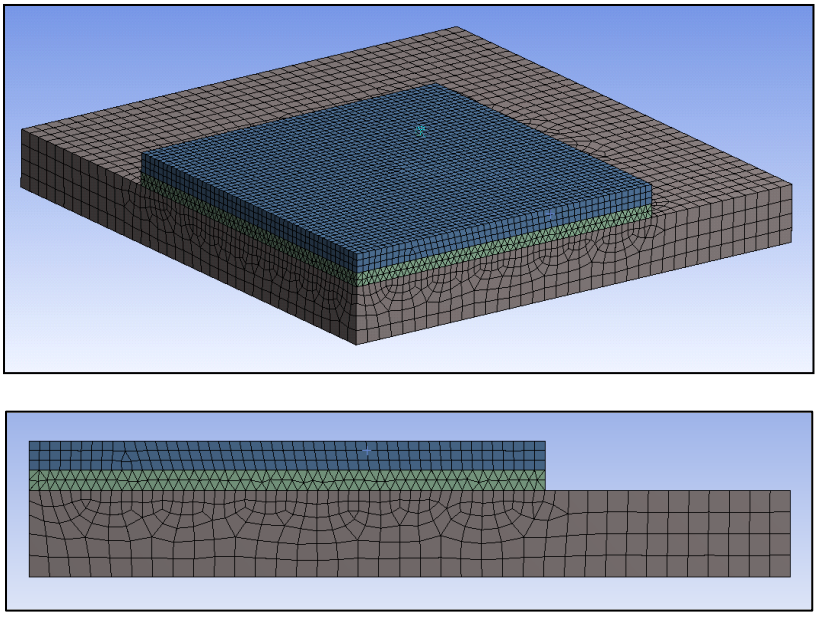

Figure 6-15 Quarter Model with Underfill

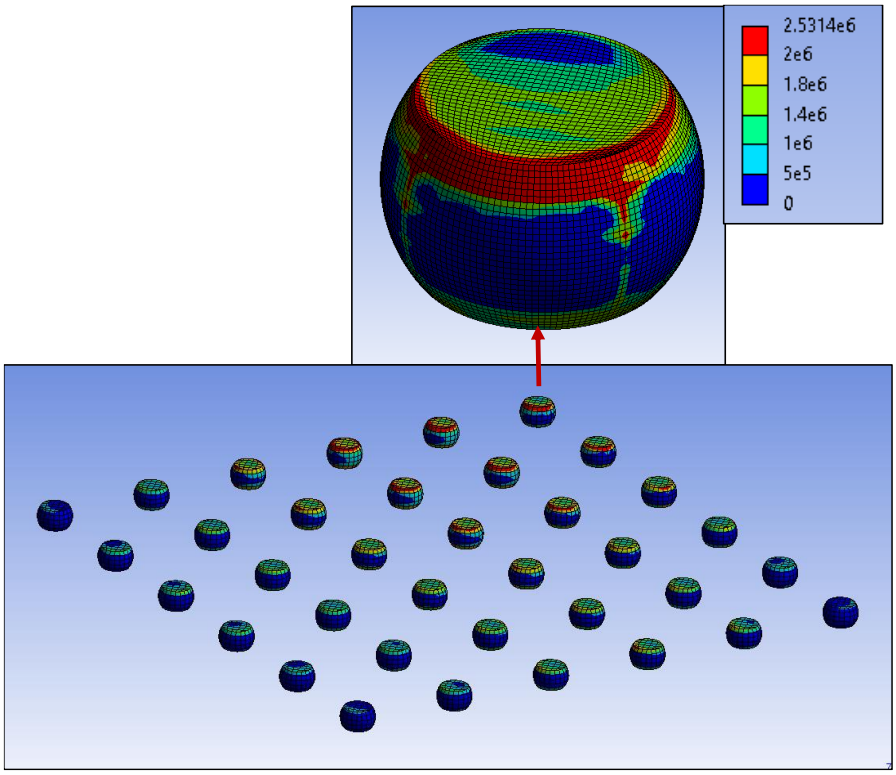

Figure 6-16 Contours of Accumulated Plastic Work (MPa) (Underfill elastic Property)

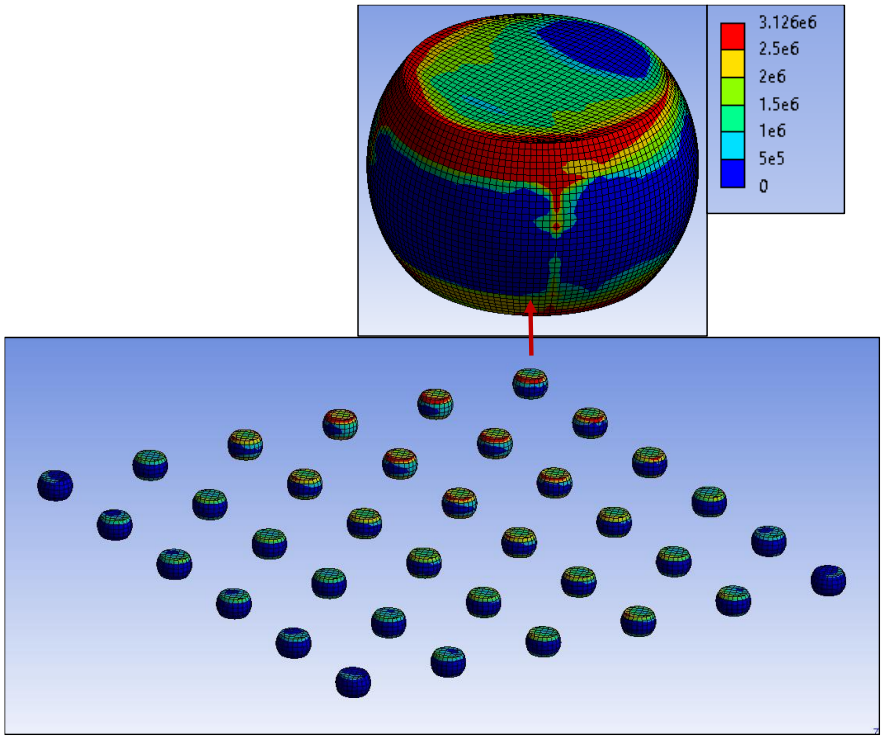

Figure 6-17 Contours of Accumulated Plastic Work (MPa) Underfill Viscoelastic Property

From the simulation, it has been found that accumulated plastic work is higher for no underfill model. For no underfill (NF) model, accumulated plastic work difference is 1.027 MPa calculated in 3rd cycle (Figure 6-18). However, elastic underfill property lowers the plastic work which confirms that using underfill property improves the fatigue behavior of solder joint. However, using viscoelastic underfill gave higher plastic work compare to elastic model. So, elastic model overestimates the failure life for solder joint (Figure 6-19). Using Darveaux constants (Table 6-6), failure life of solder joint were calculated based on equation 6.4 (Table 6-7).

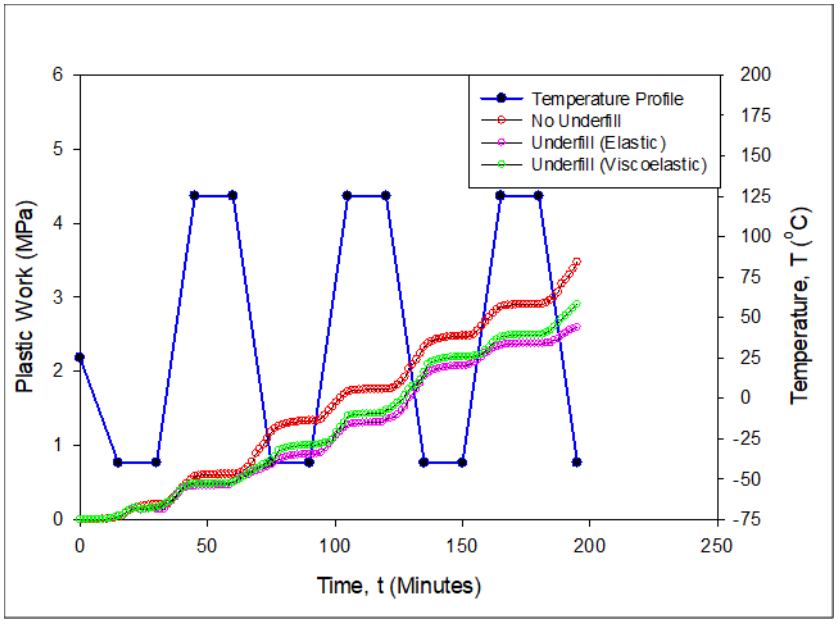

Figure 6-18 Volume Averaged Accumulated Plastic Work Vs Time up to Third Thermal Cycle

Table 6-6 Darveaux Constants [102]

Darveaux Constants	
K_1	37.97 cycles/MPa^{K_2}
K_2	-2.80
K_3	1.4 X 10^{-6} m/cycles-MPa^{K_4}
K_4	1.16

Table 6-7 Plastic Work per Cycle and Time to Failure

Model	Plastic Work Difference, ΔW_{avg} (MPa)	No of Cycles to Failure, N_f
No Underfill (NF)	1.027	173
Elastic Property (ET)	0.60	417
Viscoelastic Prony (17 Pairs)	0.71	311

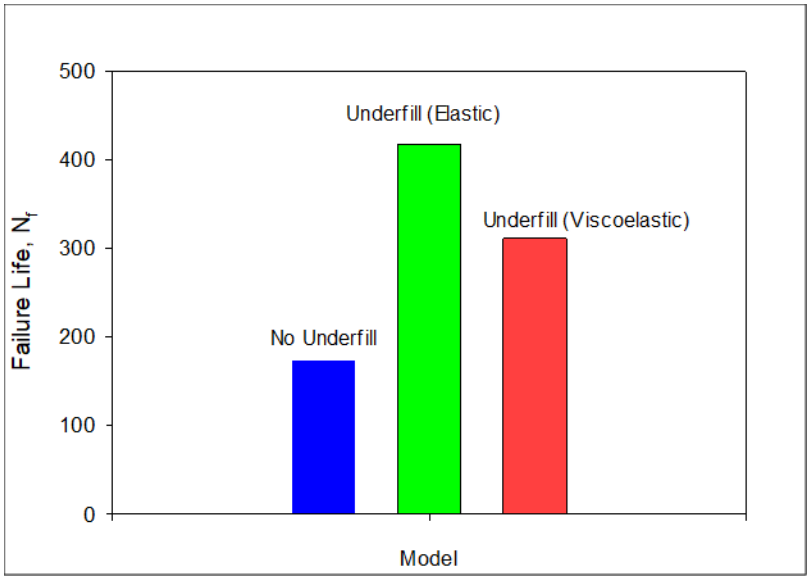

Figure 6-19 Variation of Failure Life for Different Model

The critical solder joints with the highest values was found to be at the package outside corners. To minimize the mesh dependency of the calculated plastic work values in the joints, it is conventional to calculate volume averaged values across a set of elements along the path using equation. The plastic work dissipated per cycle (delta W) was calculated for each of the first 3 cycles at the critical solder joints. Plastic work

accumulation for the 3rd cycle listed in table. Higher plastic work accumulated for without underfill model compare to elastic and viscoelastic underfill model. Elastic underfill improves the solder life by 2.4 times compare to no underfill and viscoelastic underfill improves the solder life by 1.80 times.

6.6 Summary and Discussion

Viscoelastic properties are important to predict the solder joint life prediction in flip chip assembly, warpage analysis. By using the right material property for underfill material in FE analysis, the failure behavior can be correctly estimated. Moreover, package size is getting smaller day by day, and viscoelastic material like underfill, mold compound play significant role in reliability.

In this study, we have shown that a higher number of Prony pairs is required to get the proper viscoelastic regime. However, most of the time researchers assume smaller no of Prony pairs to reduce the simulation time but, for a better and reliable study higher no of viscoelastic parameters should be used. A FEA study of an Ultra CSP package has been performed using different constitutive models for the underfill material. From the analysis, it showed that underfill improves the reliability by lowering the accumulated plastic work in the critical solder ball. However, using elastic property of underfill material overestimates the failure life by calculating lower plastic work.

CHAPTER 7

THE EFFECTS OF CURING PROFILE, TEMPERATURE, AND AGING OF THE MECHANICAL BEHAVIOR OF SOLDER MASK MATERIALS

7.1 Introduction

Consistent and wide-ranging material property data are desired for microelectronics encapsulants for mechanical design, process optimization, and reliability assessment of electronic packages. Microelectronic encapsulants show evolving properties that change prominently with environmental exposures such as isothermal aging and thermal cycling. Such aging effects are worsened at higher temperatures typical of thermal cycling qualification tests for harsh environment electronic packaging.

A solder mask is a thin polymeric coating layer, which covers the outside of a printed circuit board (PCB), and is typically green in color. It is used to prevent molten solder from adhering to selected portions of the printed circuit board traces, and the entire surface of the board is typically covered except for connection locations such as holes, pads and contact fingers. Thus, the solder mask stops oxidation and assists to resist solder bridges between copper pads. It gives mass soldering capability, prevents the growth of metal whiskers, stops corrosion in the underlying circuitry, and provides a shield to substrate from environmental effects. Typically, the thickness of solder mask ranges from 20-100 μm. The green layer in Figure 7-1 is the solder mask, while Figure 7-2 shows a cross-sectional view of a typical multi-layer printed circuit board and the solder mask layers.

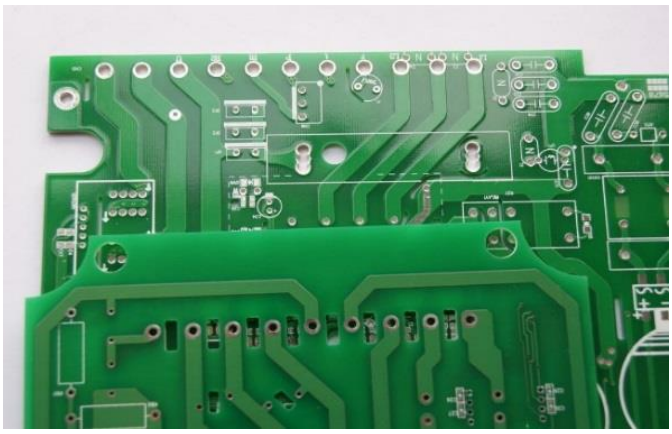

Figure 7-1 Solder Mask

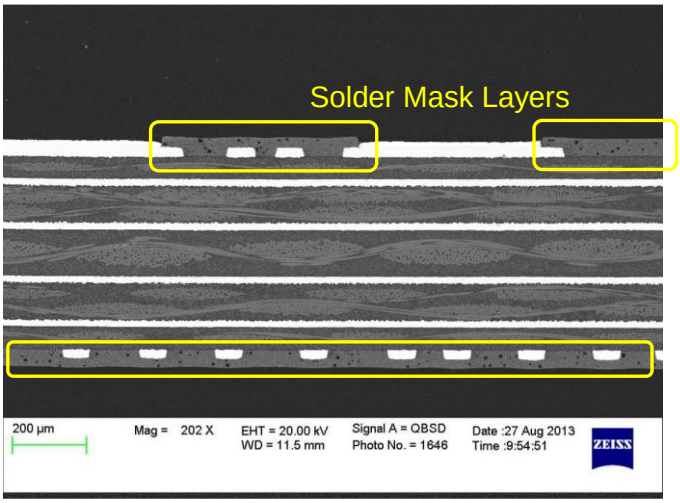

Figure 7-2 Solder Mask Cross-Section

Thin bonded layers in electronic assemblies such as underfills, die passivation, die attachment adhesives, and solder masks can play important roles in the overall reliability of the electronic system. The mechanical properties of solder masks are poorly understood and can be important factors for reliability of high-density assemblies. Michaelides and Sitaraman [1] introduced the reliability models that are based on the solder stiffness and other parameters. An integrated numerical and experimental approach in studying the effect of solder mask on the thermal fatigue life of solder joints can be found in the work

of Schubert, et al. [2]. The dependence of mechanical behavior on the temperature of solder masks and plastic packaging materials is investigated by Darveaux, Norton, and Carney [3].

It is also noted that FEM has been employed to analyze the warpage of solder masks (Ume, Martin, and Gatro) [4]. Zhu, et al. worked on several solder masks and presented the mechanical properties, creep response [5]. The mechanical properties of solder mask are very important in get reliable electronics products. Among the all mechanical properties of solder mask, tensile properties and creep response are of particular concern.

Based on the study, high temperature aging and moisture exposure to interconnect polymers has negative effect on their mechanical properties. Lin, et al. [6-8] showed that effective elastic modulus (E), ultimate tensile strength (UTS) increased with the amount of the isothermal aging or aging temperature, regardless of whether the aging temperature is below, at or above the T_g for viscoelastic material. Typically, E and UTS were increased in the range of 10-40% of the non-aged values. Aging was also found to dramatically decrease (100X) the secondary creep rate up to 6 months of aging before testing. Also, humidity exposure affects the property of this interconnect material and their property variation at different moisture condition was explored in detail [9-10]. Moisture caused detrimental effect on mechanical properties, e.g. elastic modulus and creep behavior, and the overall property degradation is depend on amount of moisture absorbed by that material.

UV curing is a photochemical process in which high-intensity ultraviolet light is used to instantly cure adhesives. In this process, a certain percent of photoinitiators are mixed with adhesive resin. The photoinitiator reacts with adhesive resin when certain

amount of UV light is delivered, and a chemical reaction take place and make the adhesive harden better. Wavelength and intensity are two important characteristics for UV light exposure. Correct light and intensity is required for the photoinitiators to react properly, otherwise chemical reaction may not happen completely and outcome will be poor or inconsistent [11]. Ramli, et al. showed that UV curing time has optimum value in which better tensile strength can be obtained. Two other adhesives also showed similar behaviors [12].

Material property data for solder mask materials are not widely available in the literature. In this work, the mechanical behavior of a typical UV curable solder mask material has been explored as a function of ultra violet (UV) curing time, testing temperature, and isothermal aging exposure. Mechanical testing has been performed using standard tensile testing. Both stress-strain and creep tests were performed. The solder mask test specimens were prepared in a unique way and no release agent is required to extract them from the mold. The mechanical behavior changes of the solder mask material were recorded for different curing profiles including various durations of UV exposure and subsequent isothermal curing.

7.2 Test Specimen Preparation

The solder mask specimens were prepared using both UV curing and thermal curing. The commercially available solder mask utilized in this work with a glass transition temperature of 104.8 ^{o}C. For making a tensile sample, at first 100 parts weight of PSR-4000-AUS5 is mixed with 43 parts CA-40 AUS2. After thoroughly mixing of both substance, the solution was poured into a Teflon-coated mold assembly which was covered

with foam tape. The tape was circulated on four sides of the mold such way that a 0.30 mm thickness was achieved. The figure is shown in below.

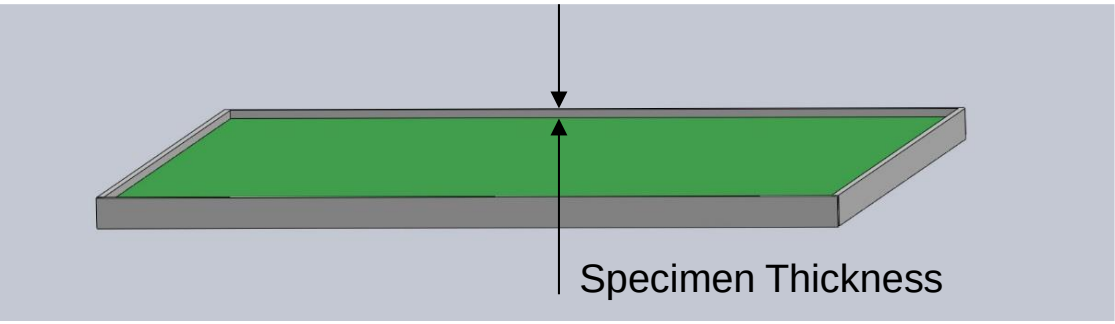

Figure 7-3 Mold Assembly for Sample Preparation

After that, solder mask poured into the cavity and it took the space with maintaining the desired thickness. Then, the whole assembly placed into an UV oven for UV light exposure. The UV oven used in this case is Dymax ECE 5000 (Figure 7-4).

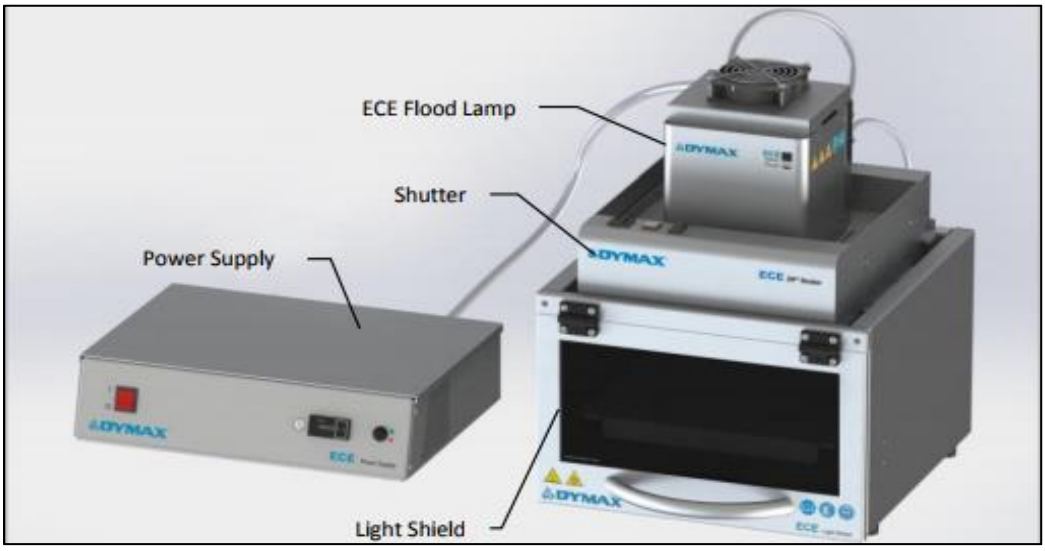

Figure 7-4 Typical UV Flood-Lamp System

Dymax UV light curing flood lamps are general purpose units for the curing of UV light curable adhesives, coating, and inks. They are extensively used for bonding, potting,

sealing and encapsulating. This unit provides an effective curing area of approximately 5'' x 5'' (12.7 cm x 12.7 cm). In that way, it is ideal for small batch processing of UV adhesives and potting compounds. Typical initial output intensity at UV-A range is 225 mW/cm^2. UV exposed sample is shown in the Figure 7-5.

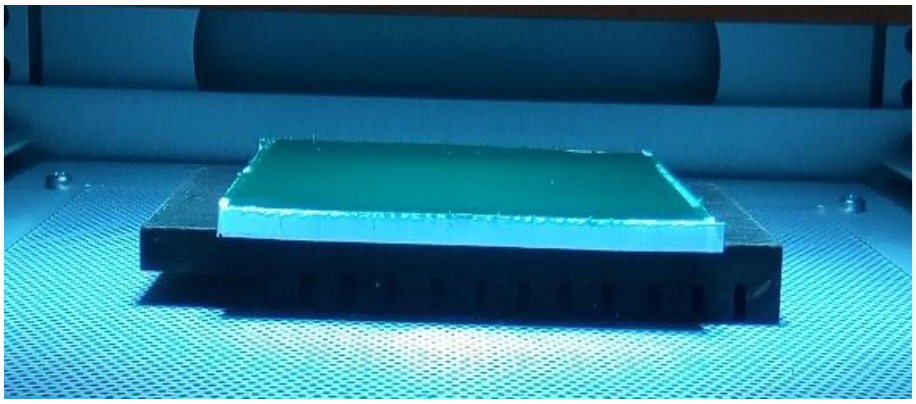

Figure 7-5 UV exposed Sample

After UV curing, solder mask was cured in a box oven at 140 ^oC for 60 minutes. Due to the Teflon coatings, the uniform thickness cured rectangular samples were easily separated from the mold. A sharp razor blade was used for cutting the samples to desired dimensions. In the described method, the specimens have a controllable constant thickness and are easily detached from the mold assembly without the help of chemical release agents. The lengths of the final trimmed samples (see Figure 7-6) were typically in the range of 70-90 mm, while the width was all 3 mm, giving a specimen length to width aspect ratio of more than 20. After having the desired dimension, the test specimens were ready for mechanical testing.

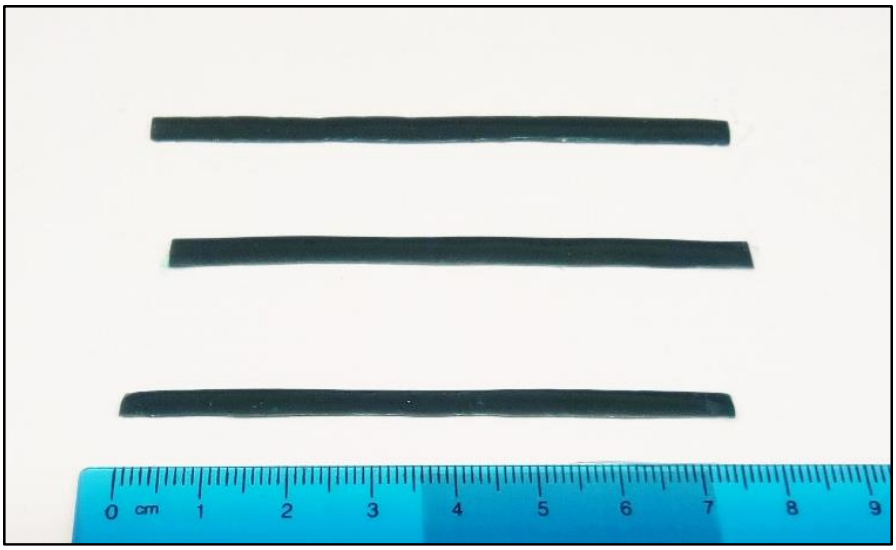

Figure 7-6 Test Specimens

7.3 Variation with UV Curing Time

Cured solder mask samples were tested using microscale tension/ torsion thermo-mechanical test system. Samples were tested at various temperatures. Samples were cured at different UV curing profile to get the optimum mechanical property. UV curing time varies from 0 to 1800 seconds. For UV curing study, all tests were performed at room temperature. Stress- strain data without any UV curing were shown in Figure 7-7. For each case, several tests had been performed to get average mechanical properties. Test was performed at 0.001 sec^{-1} strain rate.

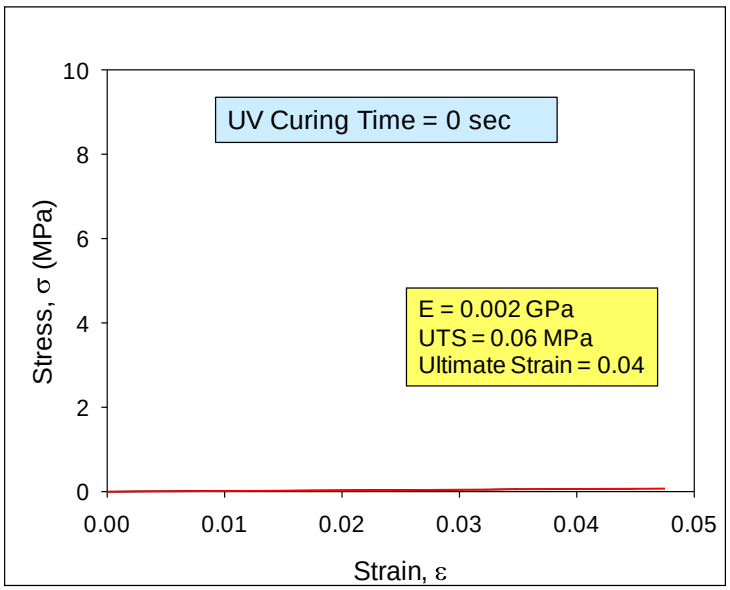

Figure 7-7 Stress Strain Tests at T = 25 ^{o}C

At different UV curing times, stress strain test results were shown in the following figures.

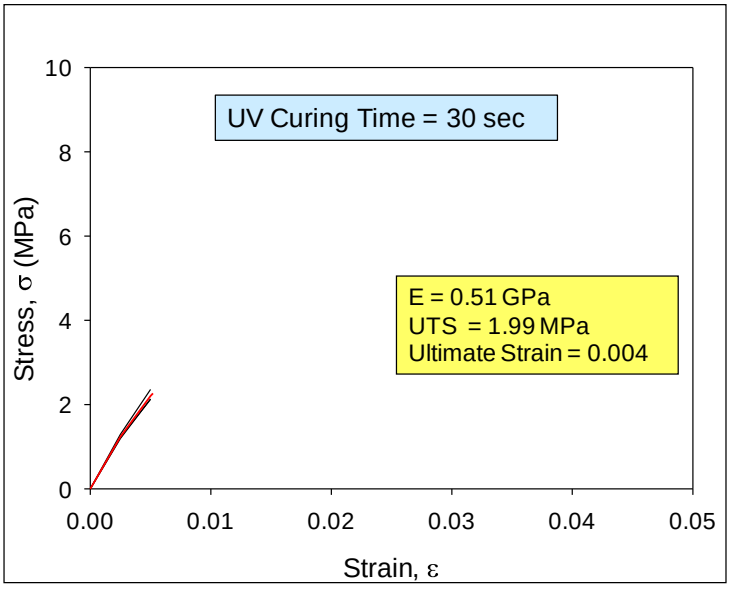

Figure 7-8 UV curing Time 30 sec

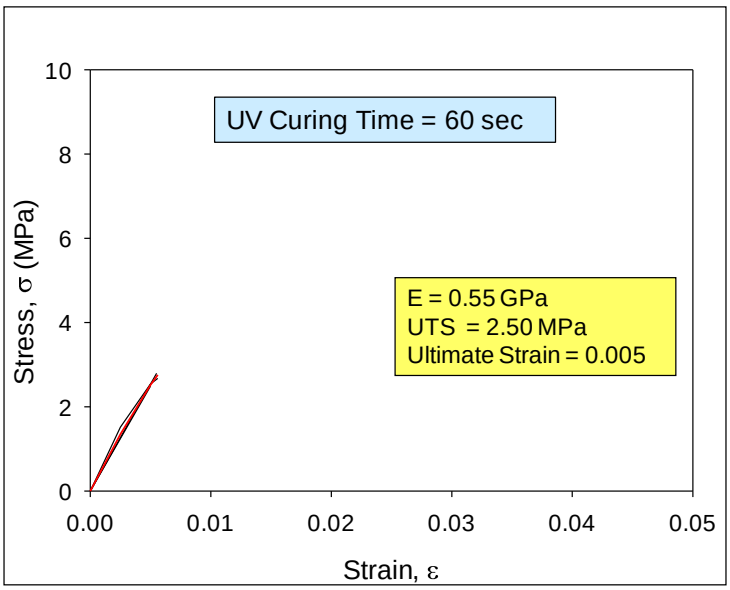

Figure 7-9 UV curing Time 60 sec

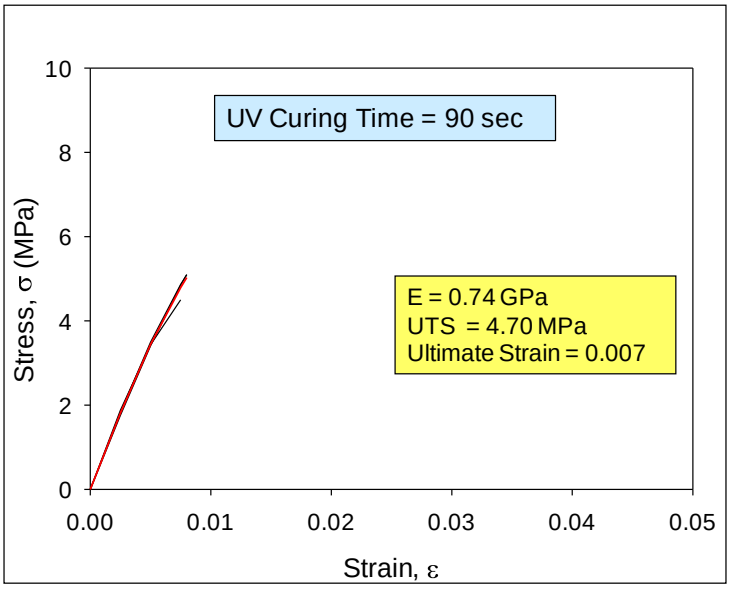

Figure 7-10 UV curing Time 90 sec

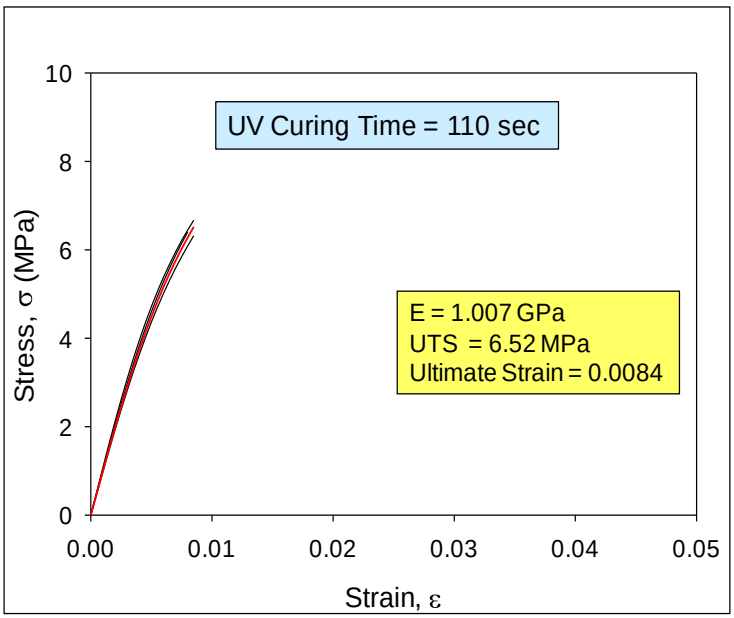

Figure 7-11 UV curing Time 110 sec

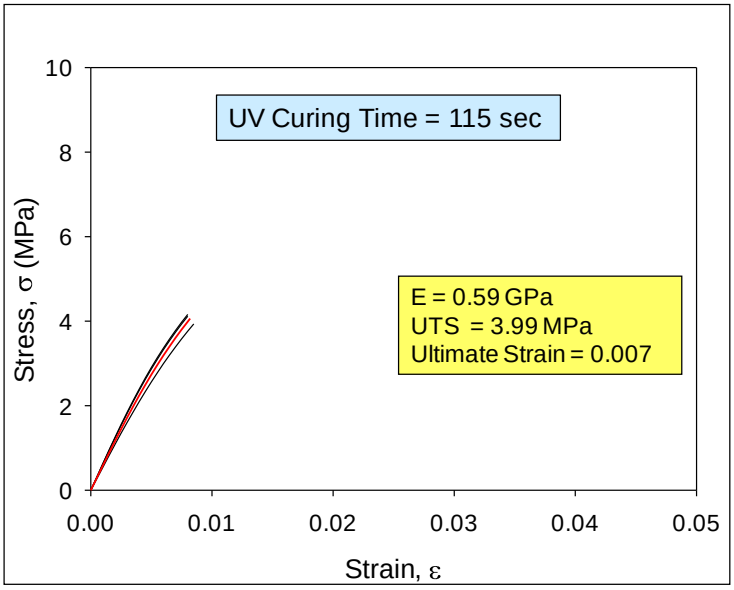

Figure 7-12 UV curing Time 115 sec

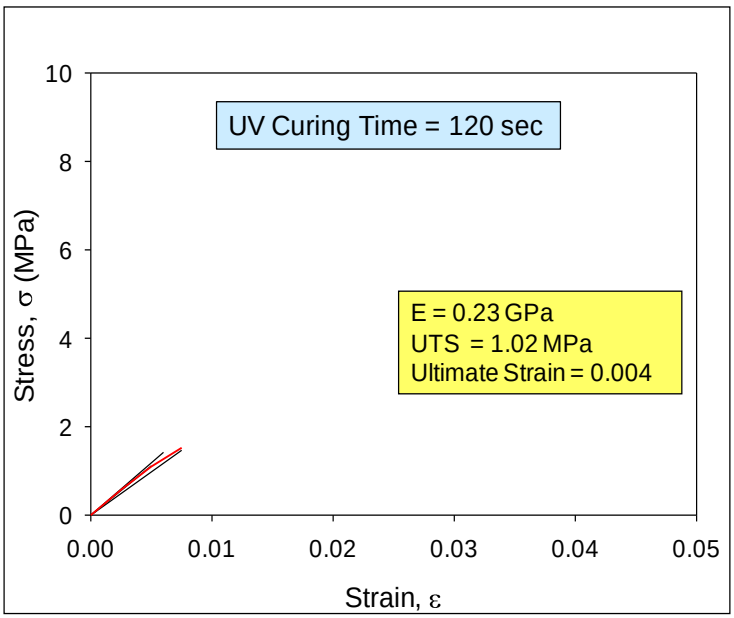

Figure 7-13 UV curing Time 120 sec

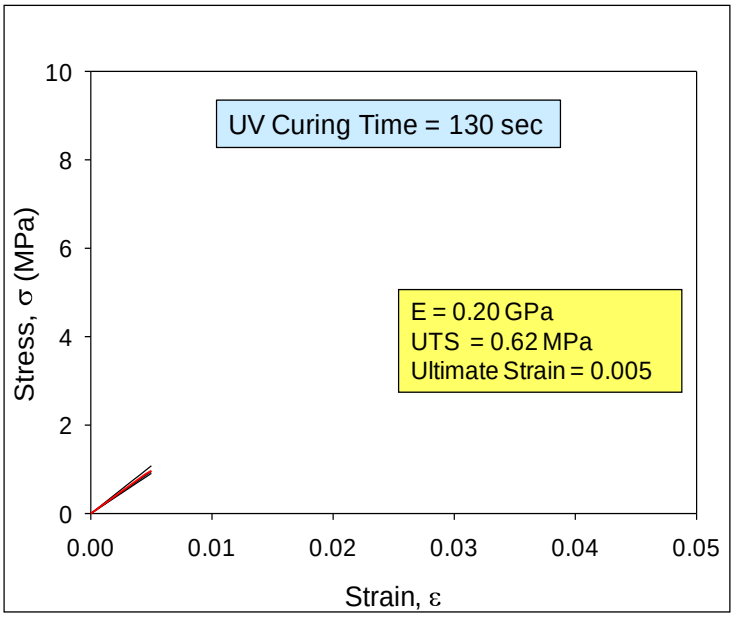

Figure 7-14 UV curing Time 130 sec

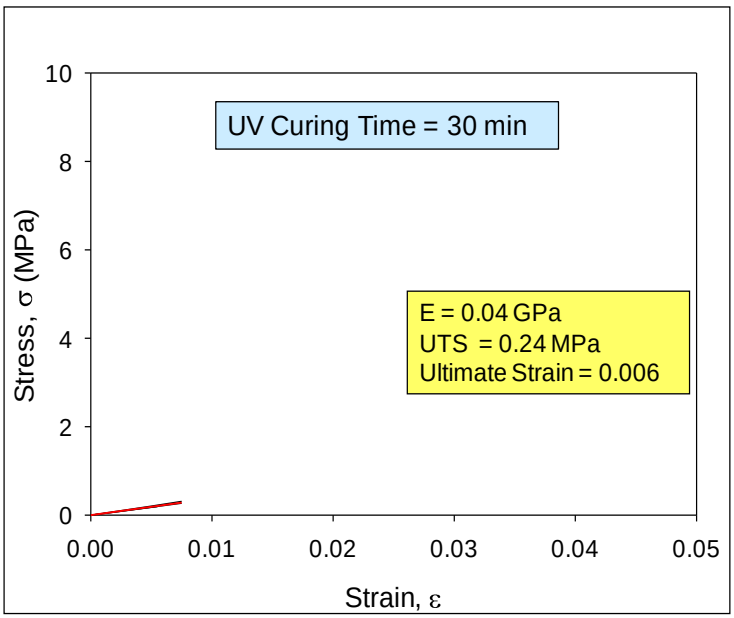

Figure 7-15 UV curing Time 30 minutes

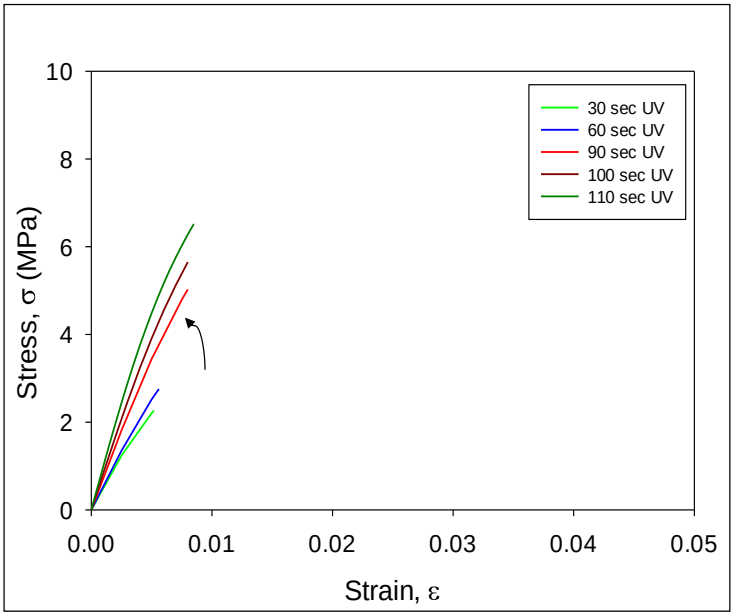

Figure 7-16 Stress vs. Strain Test Results for exposure times from 0-110 sec

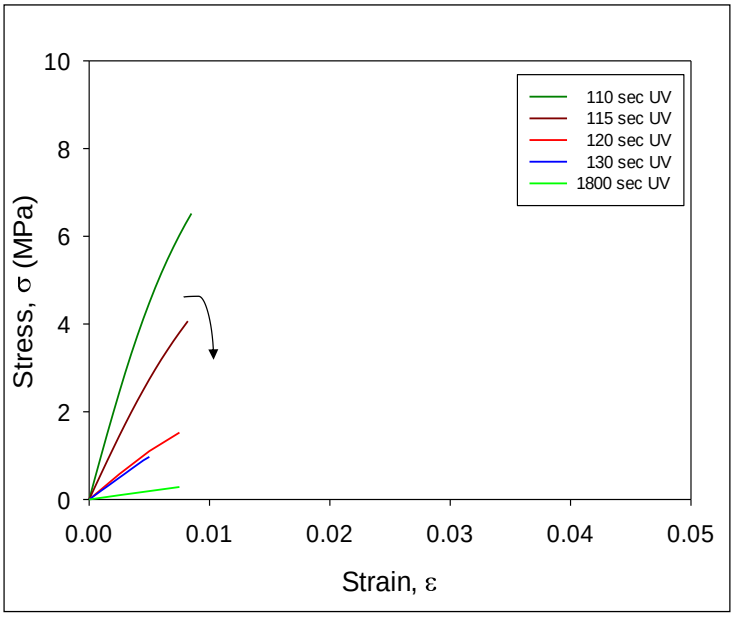

Figure 7-17 Stress vs. Strain (Exposure time 110-1800 sec)

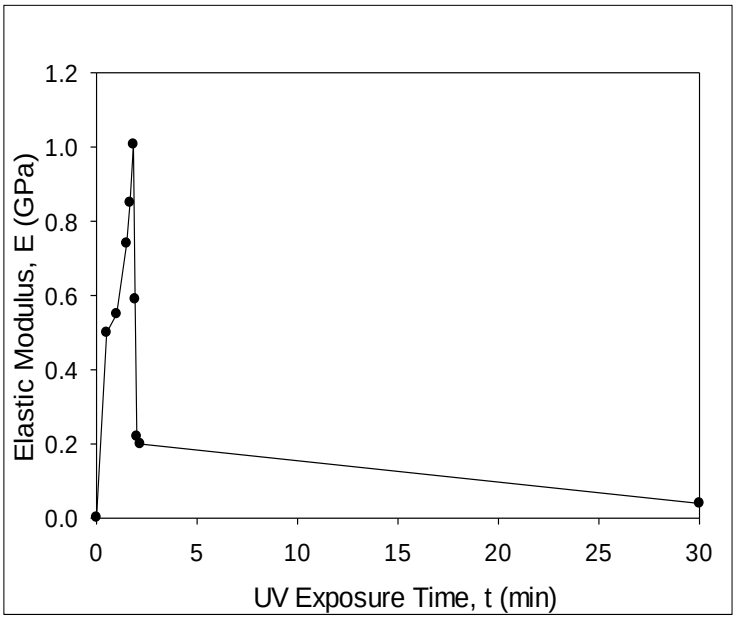

Figure 7-18 Elastic Modulus vs. UV exposure time

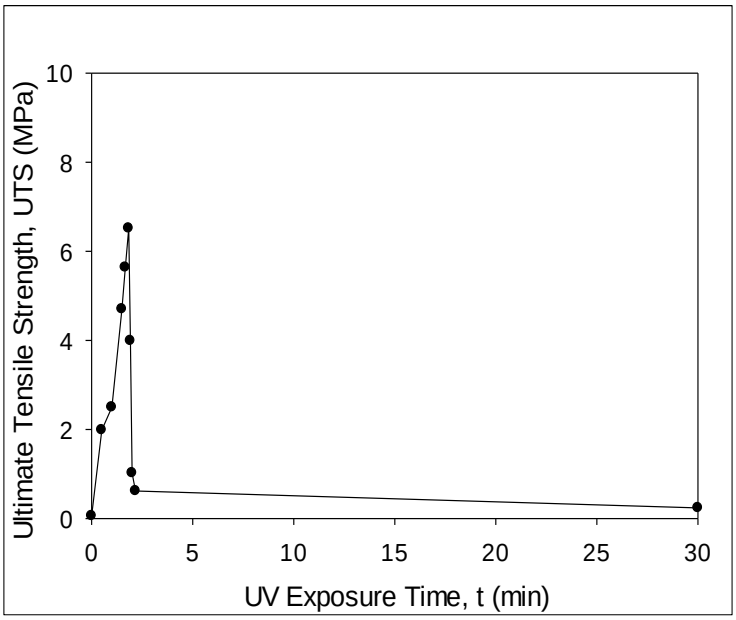

Figure 7-19 UTS vs. UV exposure time

From the study, it is obvious that better elastic modulus and ultimate strength can be found at 110 sec UV exposure time. Using this optimal curing profile, stress strain and creep behavior of this material has been explored at different temperatures.

7.4 Variation with Temperature

Stress-strain tests have been performed at 5 different testing temperatures. At each conditions, 6-10 specimens were tested at different temperatures (T = 25, 50, 75, 100, 125 ^{o}C). The raw data from each set of testing temperature were then fit with the hyperbolic tangent empirical model to generate an average stress-strain curved representation for each set of conditions. For example, the average temperature dependent stress-strain curves for 50, 75, 100, and 125 ^{o}C are shown in Figure 22, 23, 24 and 25 respectively.

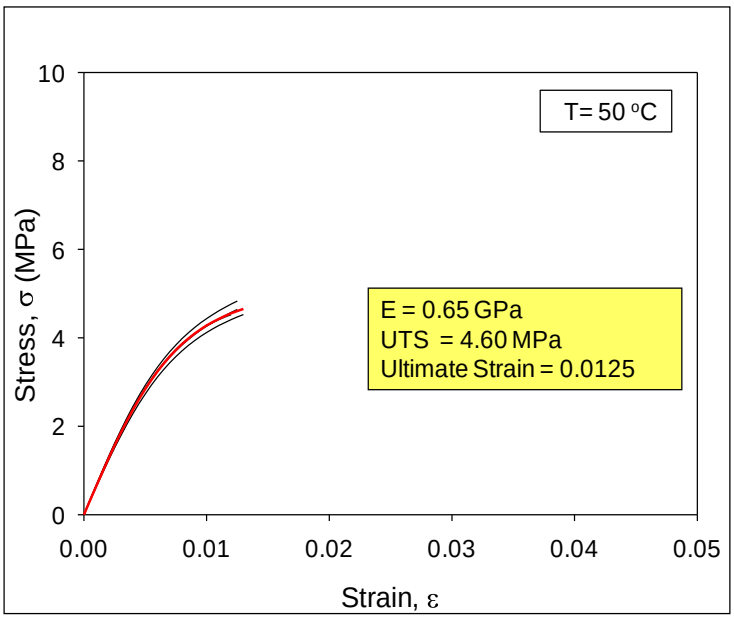

Figure 7-20 Stress Strain test at T = 50 °C

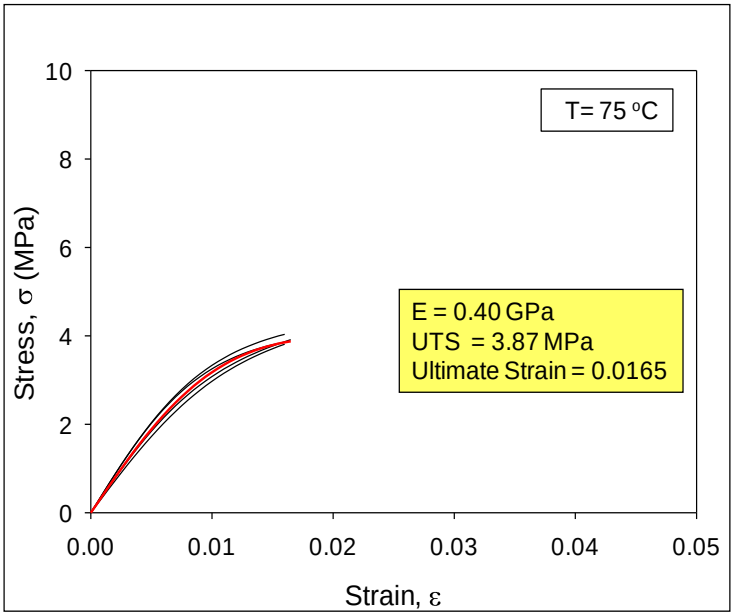

Figure 7-21 Stress Strain test at T = 75 °C

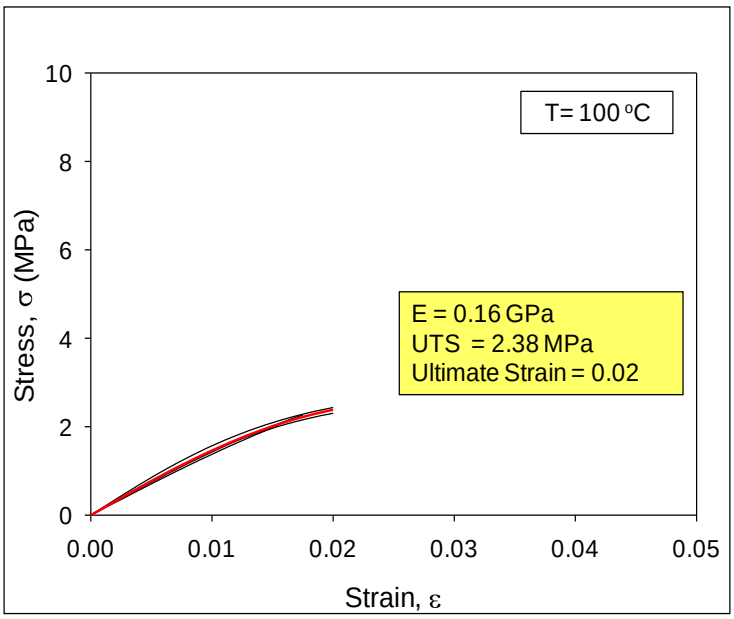

Figure 7-22 Stress Strain test at T = 100 °C

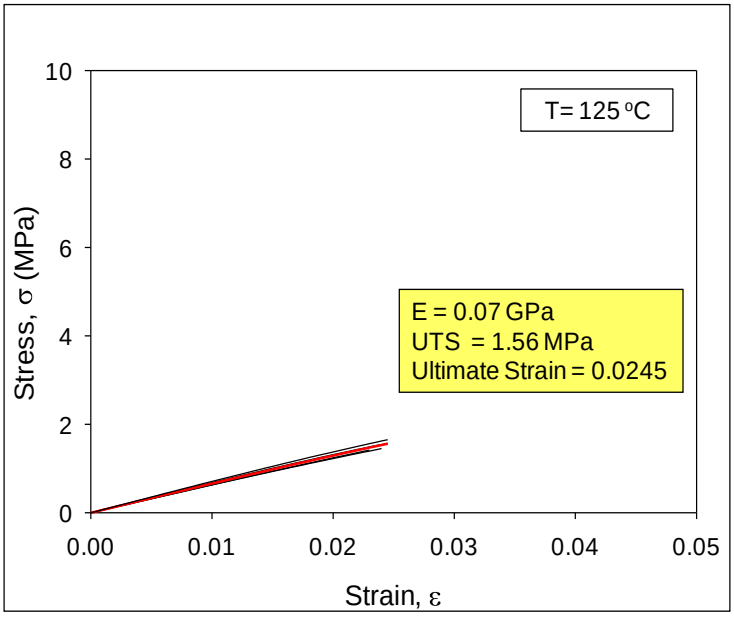

Figure 7-23 Stress Strain test at T = 125 °C

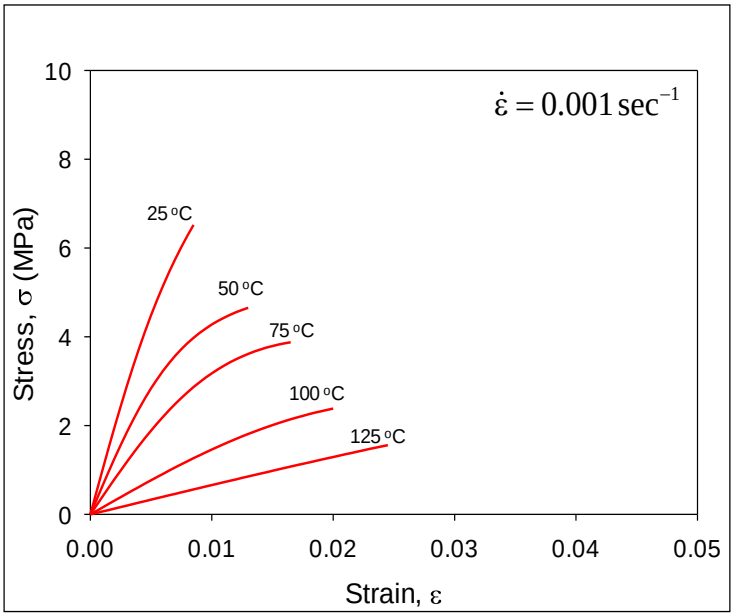

Figure 7-24 Stress-Strain Curve at Different Temperatures

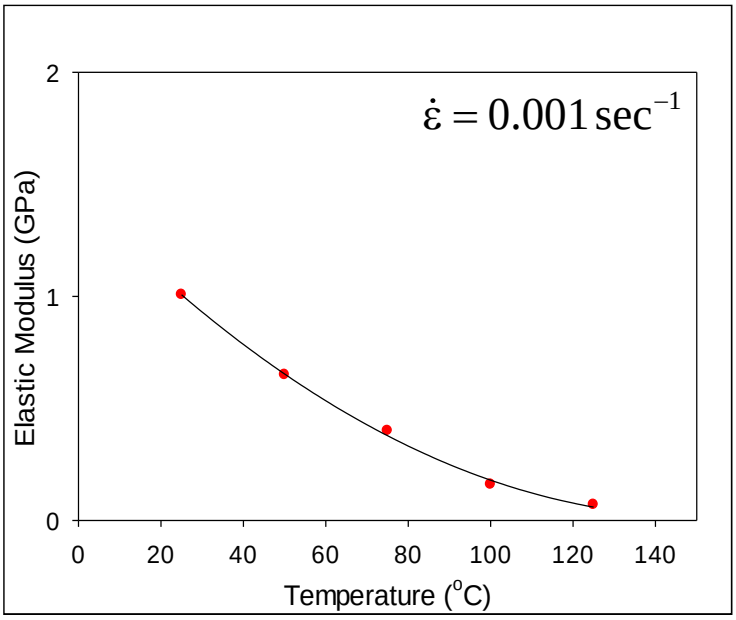

Figure 7-25 Elastic Modulus vs. Temperature

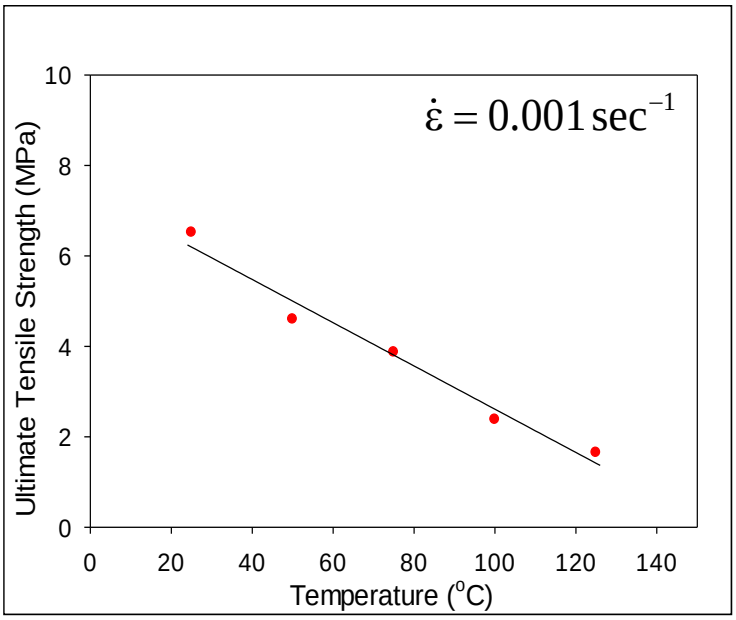

Figure 7-26 Ultimate Tensile Strength vs. Temperature

From the direct comparisons of the curves (Figure 7-24Figure 7-25Figure 7-26), it was observed that both the elastic modulus and UTS (ultimate tensile strength, i.e. the highest stress before failure) decreases significantly with test temperature.

7.5 Thermal Curing Time Variation

Cured solder mask samples were tested using microscale tension/ torsion thermomechanical test system. Samples were cured at various thermal curing profile while keeping the optimum UV curing to get the better mechanical properties. For thermal curing study, temperature was varies from 50 to 175 ^{o}C and curing time kept constant for 1 hour. All tests were performed at room temperature. Without any thermal curing test result were shown in Figure 7-27. For each case, several tests had been performed to get average mechanical properties. Test was performed at 0.001 sec^{-1} strain rate.

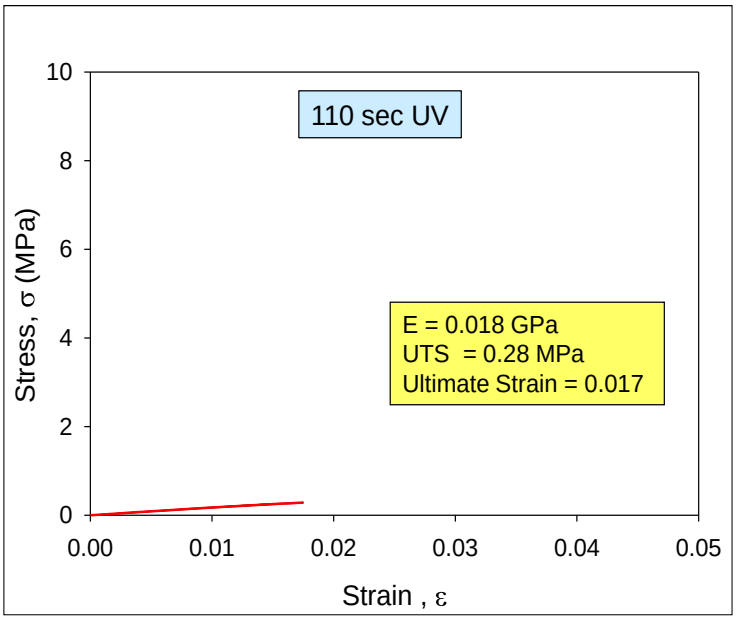

Figure 7-27 Stress Strain test at T = 25 ^{o}C (no thermal curing)

At different thermal curing time, stress strain test results were shown in the following figures.

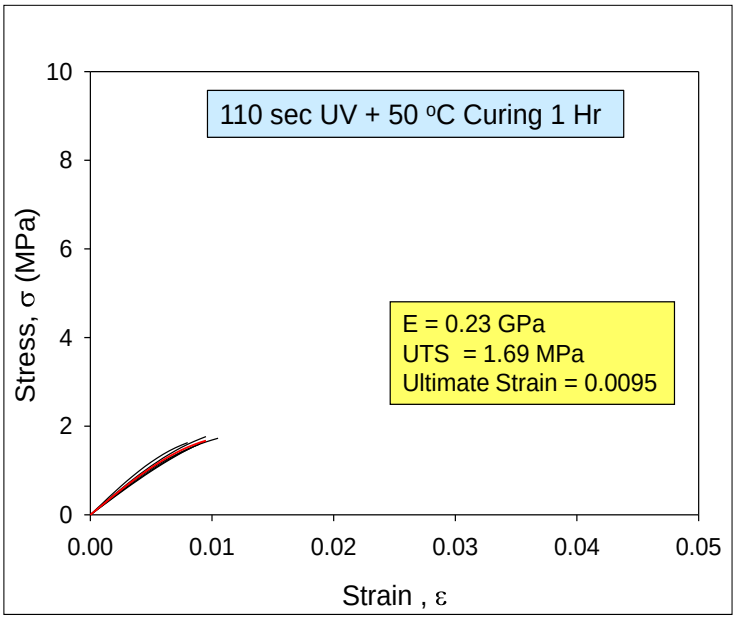

Figure 7-28 Thermal curing 50 ^{o}C for 1 hour

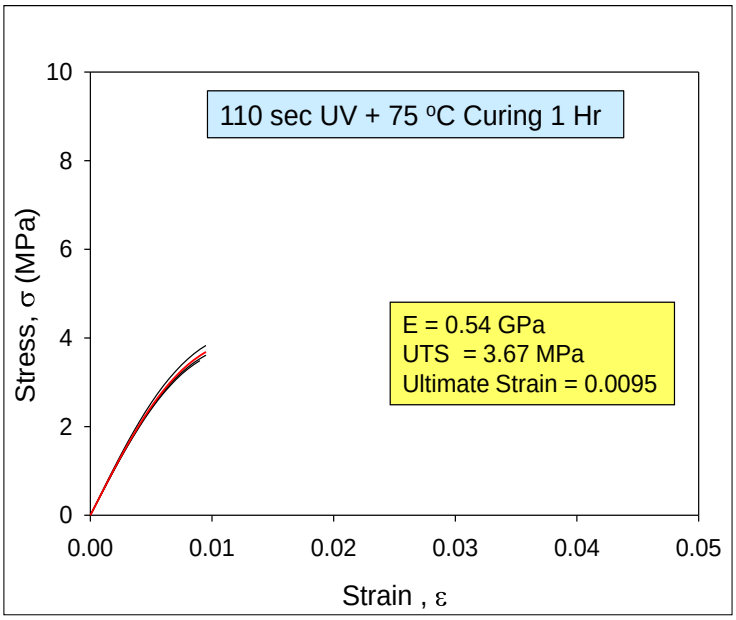

Figure 7-29 Thermal curing 75 °C for 1 hour

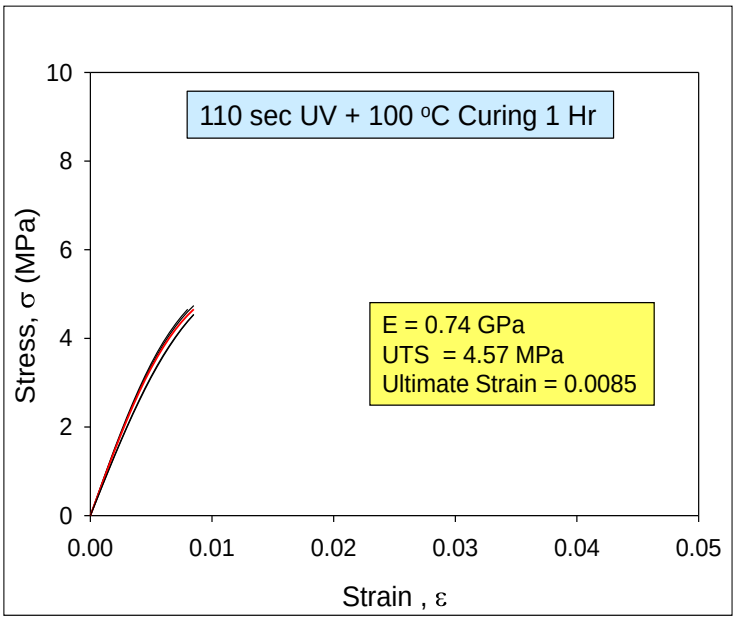

Figure 7-30 Thermal curing 100 °C for 1 hour

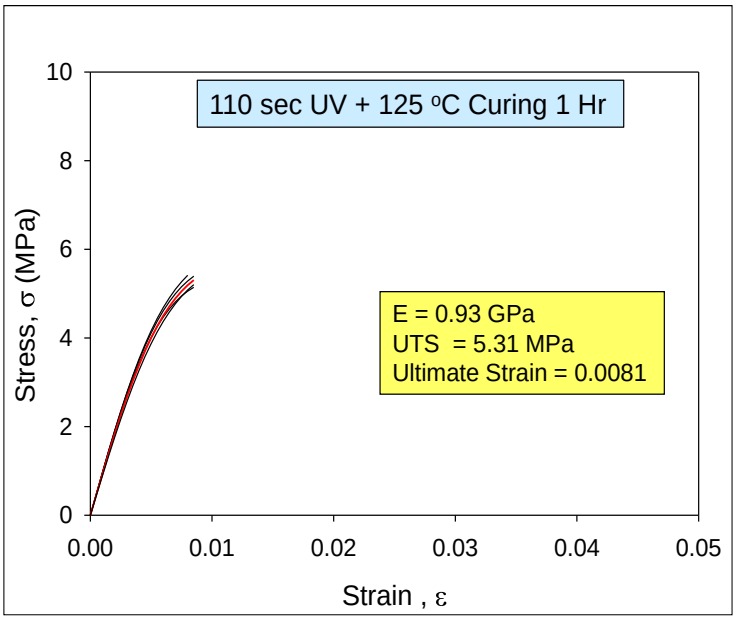

Figure 7-31 Thermal curing 125 °C for 1 hour

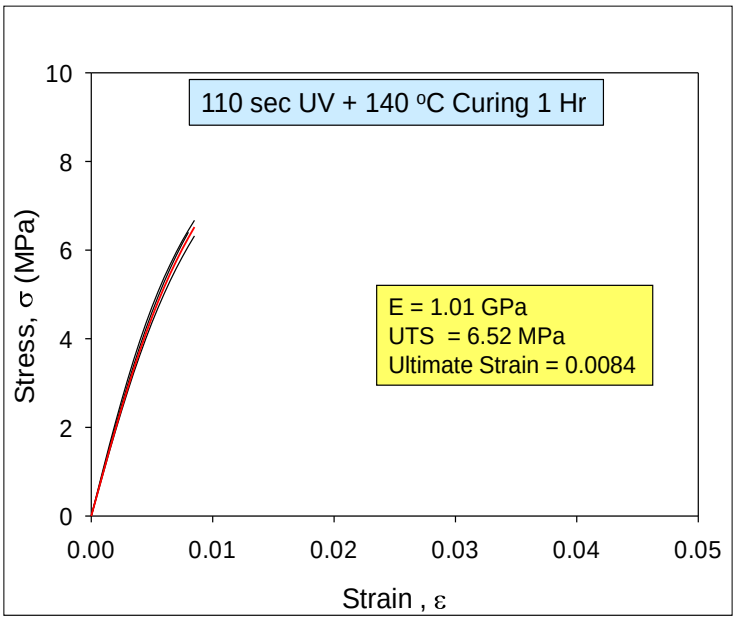

Figure 7-32 Thermal curing 140 °C for 1 hour

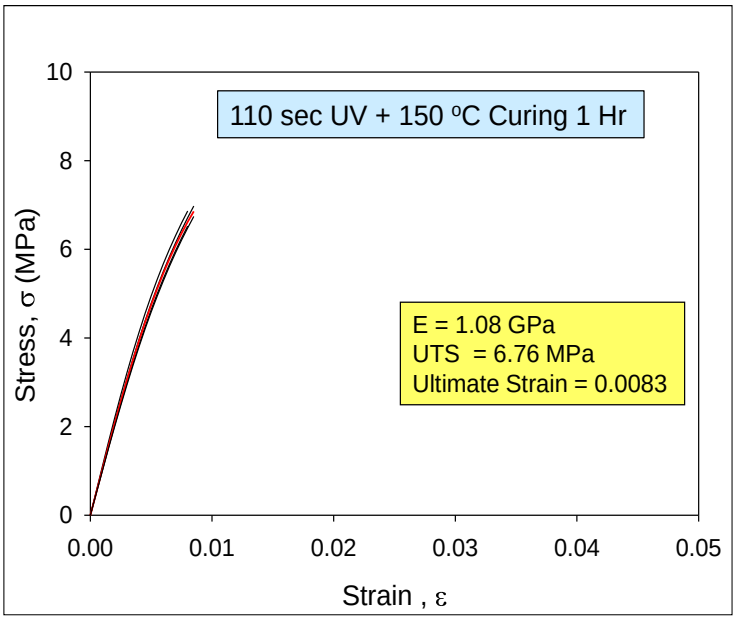

Figure 7-33 Thermal curing 150 °C for 1 hour

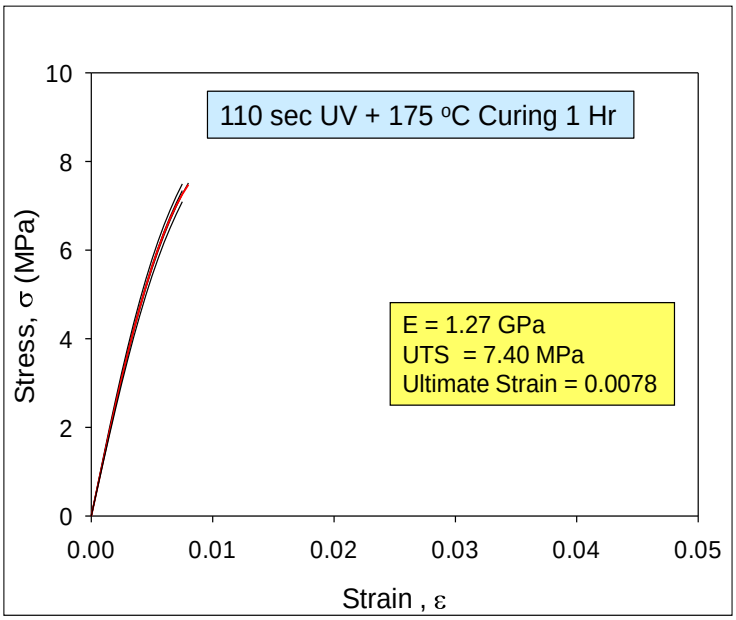

Figure 7-34 Thermal curing 175 °C for 1 hour

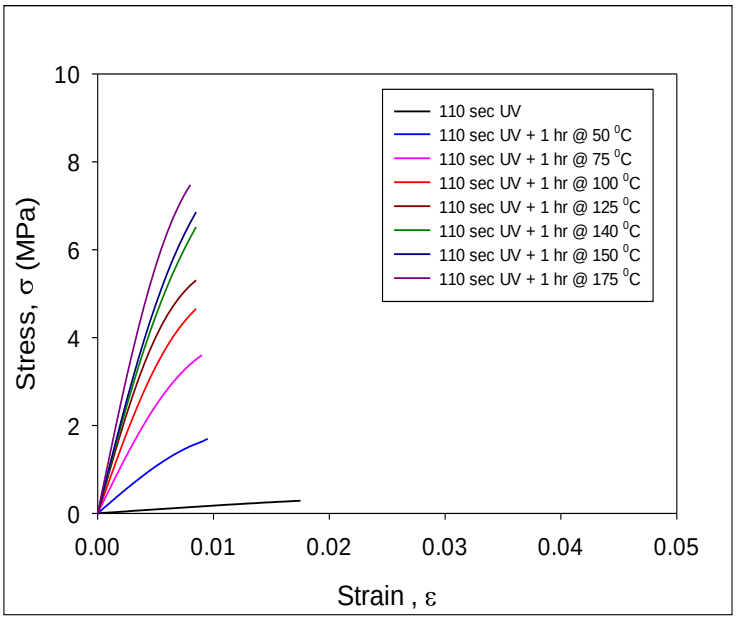

Figure 7-35 Average Stress-Strain Curve at different Thermal Curing

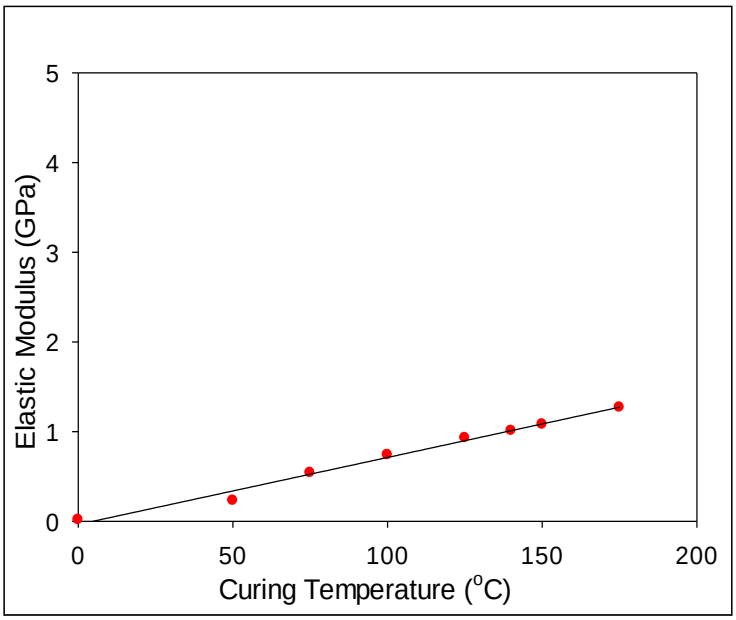

Figure 7-36 Elastic Modulus vs. Curing Temperature

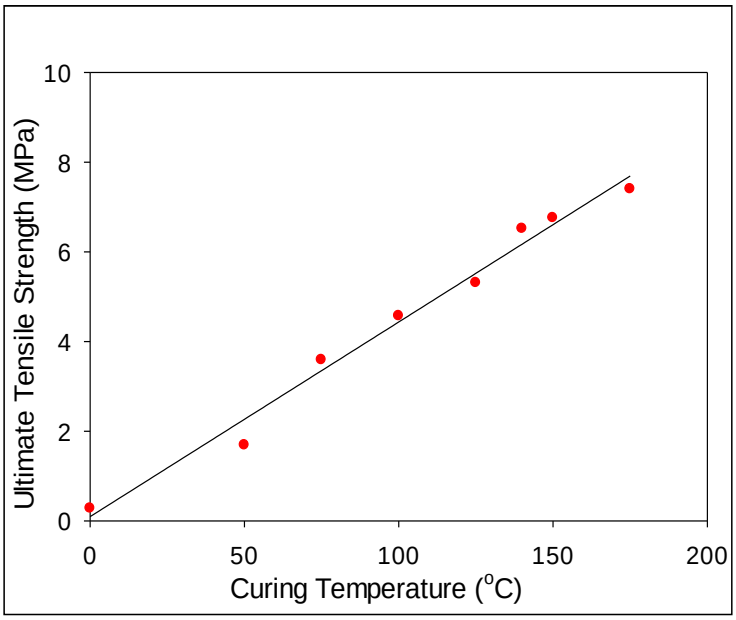

Figure 7-37 Ultimate Tensile Strength vs. Curing Temperature

From the direct comparisons of the curves (Figures 35-37), it was observed that both the elastic modulus and UTS (ultimate tensile strength, i.e. the highest stress before failure) increases with thermal curing temperature [103-104].

7.6 Aging Study

For this study, at first optimum curing profile was maintained. Then Cured solder mask samples were aged for several hours (up to 15 hours) at 100 ^{o}C before test. After certain aging time, specimens were tested using microscale tension/ torsion thermomechanical test system. For aging study, all tests were performed at room temperature. Without any aging study, test results were shown in Figure 7-11. For each case, several tests had been performed to get average mechanical properties. Test was performed at 0.001 sec^{-1} strain rate.

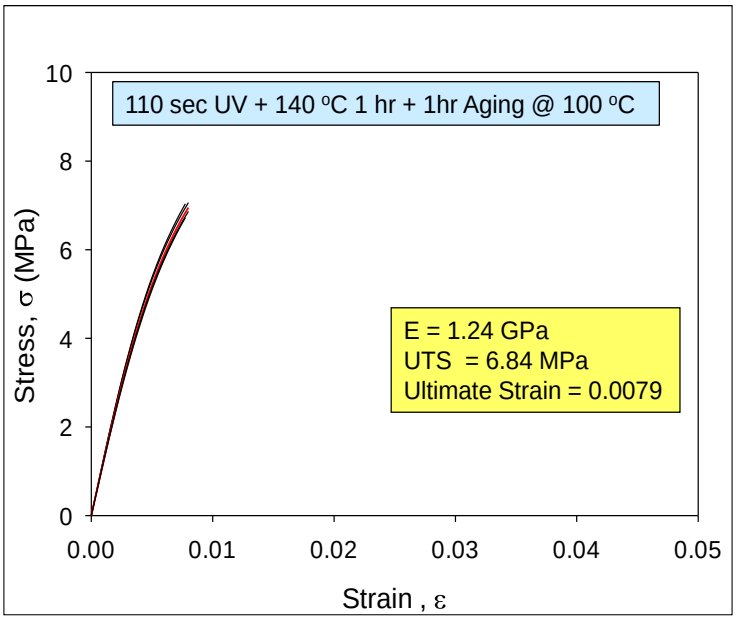

Figure 7-38 Stress Strain Curve (Aging for 1 hour at 100 °C)

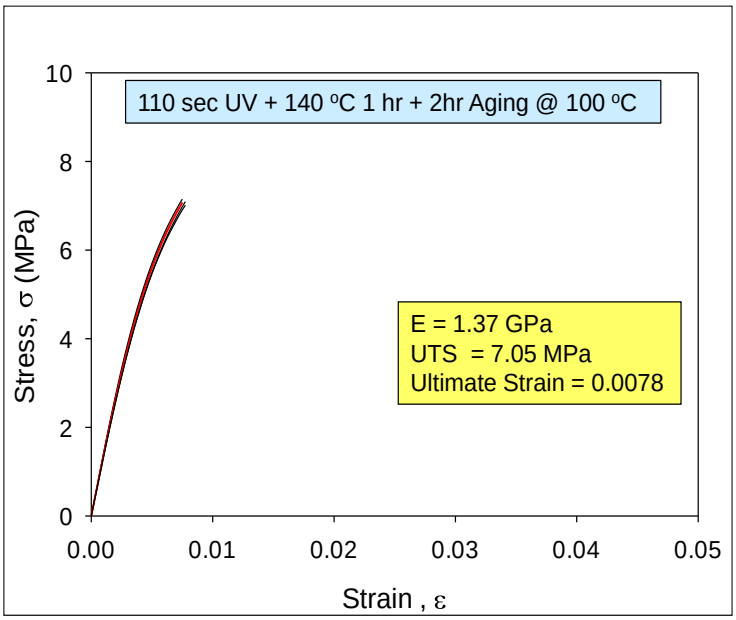

Figure 7-39 Stress Strain Curve (Aging for 2 hours at 100 °C)

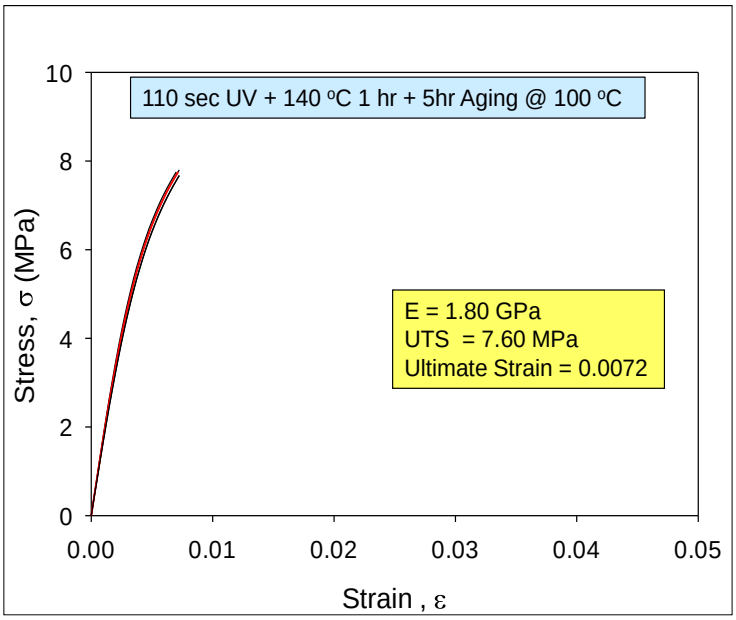

Figure 7-40 Stress Strain Curve (Aging for 5 hours at 100 oC)

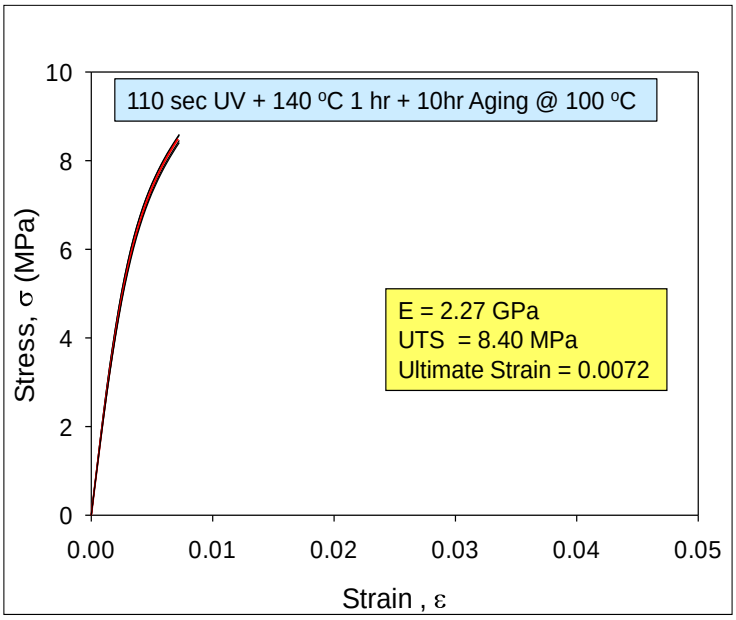

Figure 7-41 Stress Strain Curve (Aging for 10 hours at 100 °C)

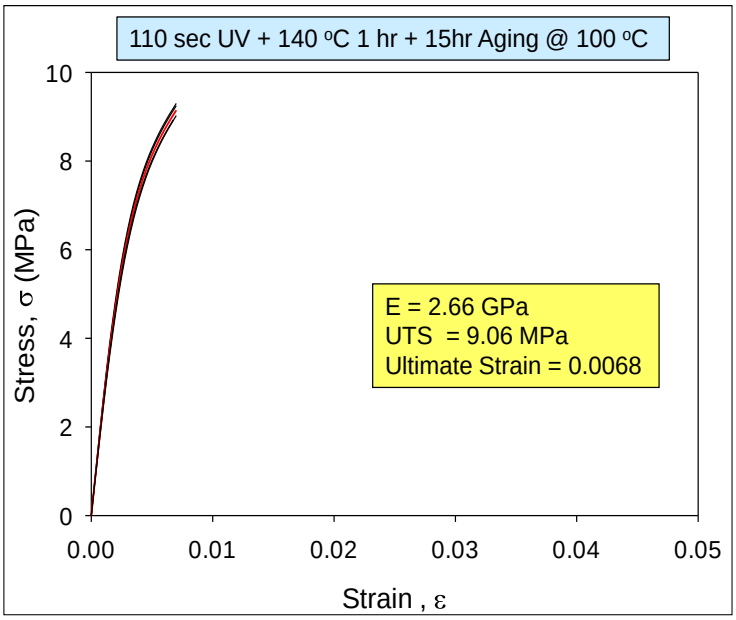

Figure 7-42 Stress Strain Curve (Aging for 15 hours at 100 °C)

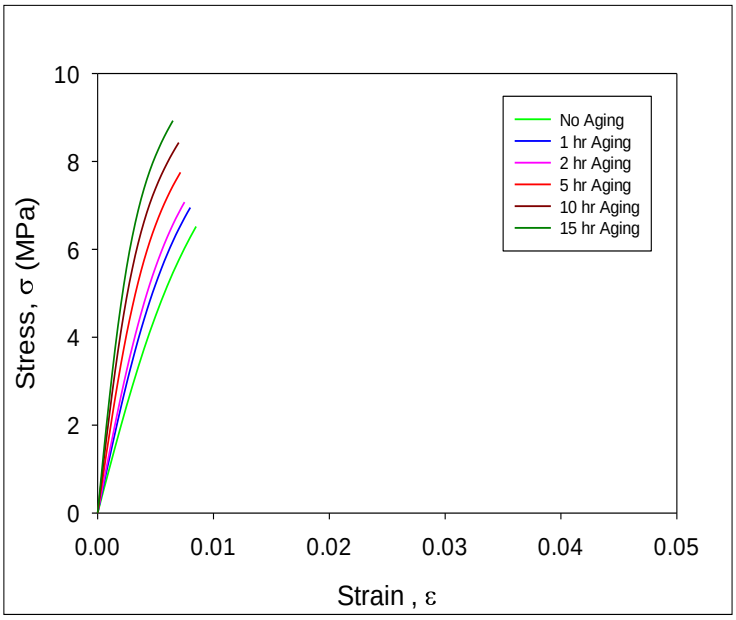

Figure 7-43 Average Stress-Strain Curves for Different Aging Time

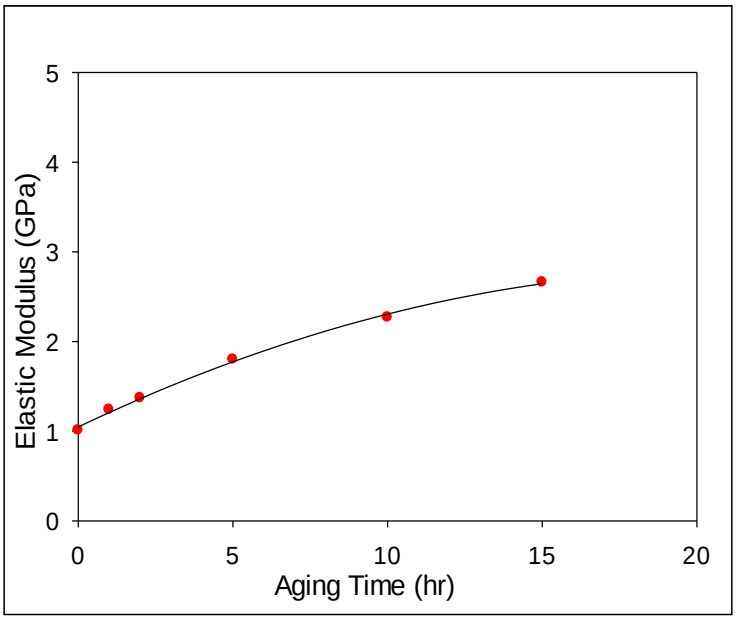

Figure 7-44 Elastic Modulus vs. Aging Time

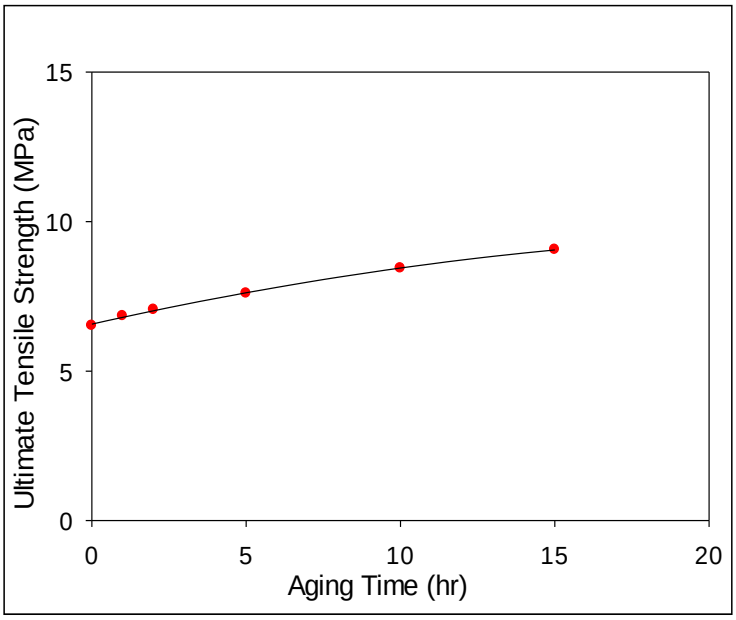

Figure 7-45 Ultimate Tensile Strength vs. Aging Time

From the direct comparisons of the curves (Figures 43-45), it was observed that both the elastic modulus and UTS (ultimate tensile strength, i.e. the highest stress before

failure) increases with thermal aging. This result supports the finding obtained by Lin, et al.[84], [85] .

7.7 Creep Study

The creep study has been conducted on solder mask specimens at room temperature. Creep experiment has been performed at 3 different stress level 0.50, 0.75 and 1.0 MPa.

In a typical creep curve, initial "elastic" strain level is followed by regions of primary and secondary creep. A very long duration of nearly constant slope is referred as the secondary creep region. This steady creep rate is often used by engineers as one of the key material parameters in finite element simulations. The measured creep rates were taken to be the slope values at the end of the linear portion in the observed secondary creep regions. Due to long testing time, 3 specimens have been tested for each condition. The curves in each set were fitted with an empirical strain-time model to generate an “average” illustration of the creep response for those circumstances. For the variety of test conditions considered in this work, the raw strain versus time data in the primary and secondary creep regions was found to be well fitted by an empirical Log Hyperbolic Tangent model figure 22.

$$\varepsilon_{cr} = c_1 \ln(1+t) + c_2 \tanh(c_3 t) + c_4 t \quad (1)$$

Constant C_4 is the long-term (steady-state) creep rate in the secondary creep region. Constants C_1 and C_2 are parameters used to describe the nonlinear response in the primary creep region. From the recorded strain vs. time curves under constant stress, the “steady state” creep strain rates have been extracted.

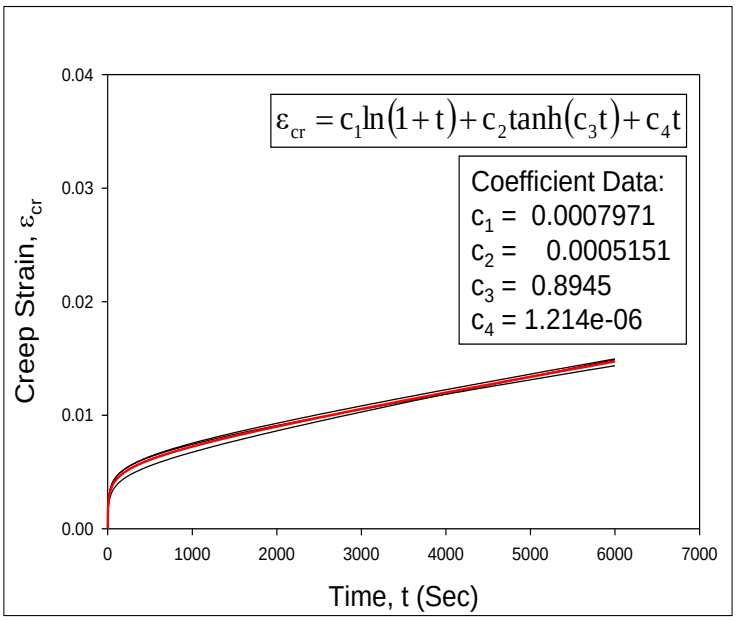

Figure 7-46 Empirical Model Fit

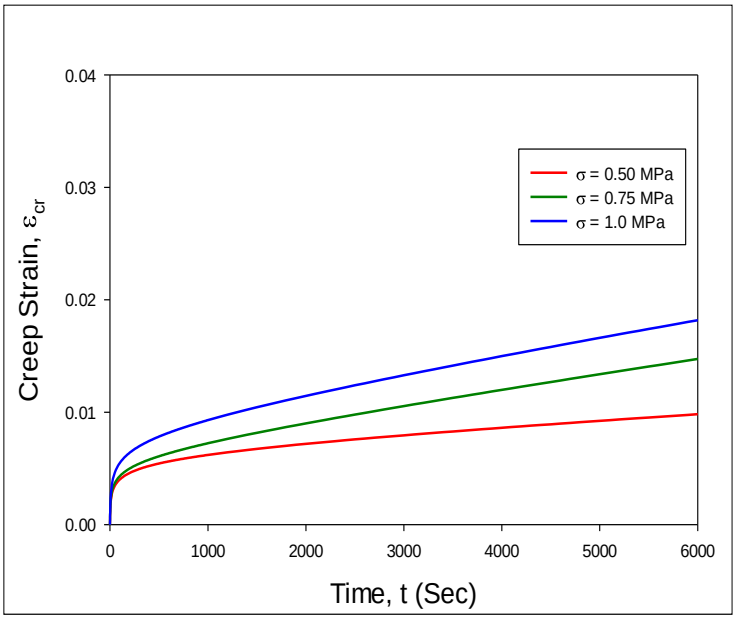

Figure 7-47 Creep Data at Different Stress Level

Measured creep strain rate at 0.50, 0.75, and 1.0 MPa stress level are 60.22 x 10^{-8}, 137.28 x 10^{-8}, and 160.52 x 10^{-8} respectively. As expected, creep strain rate is increases with stress level.

7.8 Summary and Discussion

In this work, we have shown measurements of solder mask material behavior changes with different temperatures. A microscale tension-torsion testing machine was used to evaluate the uniaxial tensile stress-strain behaviors at several test temperatures. We have also performed experiments by varying UV exposure curing time effects on mechanical properties.

The study showed an optimum UV curing time is needed to get better mechanical properties. In our study, we have seen that 110 seconds UV exposure provides higher property then other exposure time. Both the effective elastic modulus (initial slope) and ultimate tensile strength (highest stress before failure) increase monotonically with UV curing time and reaches its maximum point at 110 seconds. After that, mechanical properties decrease rapidly. Similar phenomena also observed for sunlight exposure. Sunlight also emit UV light and excessive sunlight exposure also causes problem in human skin.

As expected, solder mask mechanical properties (elastic modulus and ultimate tensile strength) decreased significantly with the testing temperature; while the creep strain rate increased is increased with stress level. The experimental result showed that variation in thermal curing profile changes the mechanical properties, and the elastic modulus and UTS both increased significantly with higher temperature curing. Further study is ongoing to characterize the changes in mechanical properties with isothermal aging. Results so far have shown that isothermal aging at 100 ^{o}C increases the mechanical properties up to 150% with aging time.

CHAPTER 8

CONCLUSIONS

8.1 Literature Review

Microelectronics packaging materials highly nonlinear in nature. In this study, an extensive literature review has been performed on moisture behavior, viscoelastic modeling in several experimental techniques, thermal cycling reliability analysis using the measure viscoelastic property and solder mask curing behavior addition to aging study.

8.2 Specimen Preparation and Experimental Setup

A unique specimen preparation procedure has been developed in this study to fabricate micro-scale uniaxial tensile specimens. A set of molds made from stainless steel and coated with Teflon have been utilized to prepare the specimens. Typical uniaxial samples with nominal dimensions have been utilized.

Uniaxial tensile and creep tests have been performed by using a multifunctional micro tester. In this study, the experimental data have been modeled by empirical constitutive laws so that the corresponding mechanical properties of materials can be extracted. Moreover, DMA have also been performed to study mechanical behavior of polymer materials.

8.3 Effect of Moisture on the Mechanical Properties of Underfill

A preliminary study was performed to determine effects of moisture exposure on the stress-strain and creep behaviors of a typical underfill material. In particular, new results detailing the effects of preconditioning on the stress-strain behavior and the effects of moisture on the creep behavior of underfills have been presented. The specimens were

exposed in an adjustable thermal and humidity chamber at a particular controlled temperature and humidity condition for specific time duration. It is found that moisture diffuses into the underfill and degrades the mechanical properties of the encapsulant (initial elastic modulus and ultimate tensile stress) up to 15%. We also found that moisture exposure slowly increases the secondary creep strain rate except at high stress levels.

Preconditioning by baking the samples for 24 hours at 85 oC was found to increase the initial material properties, but the degradations due to subsequent moisture exposures occurred in a similar manner. For 60 days of moisture exposure, the observed increases in the secondary creep rate ranged from 20-70% for applied stress levels between 20-60 MPa. MSL 1 condition degrade the material property more quickly than MSL 2 and MSL 3. Lower elastic modulus and ultimate tensile strength values were found for MSL 1 relative to the values found for MSL 2 and MSL 3.

The initial elastic modulus and Ultimate Tensile Strength were found to vary linearly with moisture concentration, and the response was not dependent on the MSL level used to force the moisture into the sample. Thus, the mechanical properties are only dependent on amount of water that has been absorbed by the material, regardless of how rapidly it was absorbed. Similar results were found for the variation of secondary creep rate with moisture concentration. For each applied stress level, the secondary creep rate data were found to lie right on top of one another for the various MSL exposure conditions, and a single model could be used to fit all of the data.

8.4 Viscoelastic Modeling of Underfill

In this work, we have characterized a commercially available underfill viscoelastic material behavior using dynamic mechanical analyzer and performing stress relaxation test. Master curve has been generated and WLF shift function has been calculated for both cases. We have also determined the Prony series parameters for shear and bulk response. By performing the stress relaxation test at different temperatures, we have generated the master curve and WLF shift parameters. Also, Prony pairs have been determined and it is found that the higher no of Prony pairs better predict the stress strain and creep behavior compare to lower Prony pairs. Viscoelastic properties are important to predict the solder joint life prediction in flip chip assembly, warpage analysis. By using the right material property for underfill material in FE analysis, the failure behavior can be correctly estimated. Moreover, package size is getting smaller day by day, and viscoelastic material like underfill, mold compound plays important role in reliability. In this study, we have shown that a higher number of Prony pairs is required to get the proper viscoelastic regime. However, most of the time researchers assume smaller no of Prony pairs to reduce the simulation time but, for a better and reliable study higher no of viscoelastic parameters should be used.

8.5 Thermal Cycling Reliability Prediction using Finite Element Analysis for Underfill BGA Assemblies with Viscoelastic Underfill

Viscoelastic properties are important to predict the solder joint life prediction in flip chip assembly, warpage analysis. By using the right material property for underfill material in FE analysis, the failure behavior can be correctly estimated. Moreover, package size is getting smaller day by day, and viscoelastic material like underfill, mold compound plays important role in reliability. In this study, we have shown that a higher number of

Prony pairs is required to get the proper viscoelastic regime. However, most of the time researchers assume smaller no of Prony pairs to reduce the simulation time but, for a better and reliable study higher no of viscoelastic parameters should be used. A FEA study of an Ultra CSP package has been performed using different constitutive models for the underfill material. From the analysis, it showed that underfill improves the reliability by lowering the accumulated plastic work in the critical solder ball. However, using elastic property of underfill material overestimates the failure life by calculating lower plastic work.

8.6 Effects of Curing Profile, Temperature, and Aging of the Mechanical Behavior of Solder Mask Materials

In this work, we have shown measurements of solder mask material behavior changes with different temperatures. A microscale tension-torsion testing machine was used to evaluate the uniaxial tensile stress-strain behaviors at several test temperatures. We have also performed experiments by varying UV exposure curing time effects on mechanical properties.

The study showed an optimum UV curing time is needed to get better mechanical properties. In our study, we have seen that 110 seconds UV exposure provides higher property then other exposure time. Both the effective elastic modulus (initial slope) and ultimate tensile strength (highest stress before failure) increase monotonically with UV curing time and reaches its maximum point at 110 seconds. After that, mechanical properties decrease rapidly.

As expected, solder mask mechanical properties (elastic modulus and ultimate tensile strength) decreased significantly with the testing temperature; while the creep strain rate increased is increased with stress level. The experimental result showed that variation

in thermal curing profile changes the mechanical properties, and the elastic modulus and UTS both increased significantly with higher temperature curing. Further study is ongoing to characterize the changes in mechanical properties with isothermal aging. Results so far have shown that isothermal aging at 100 ^{o}C increases the mechanical properties up to 150% with aging time.

8.7 Future Work

Following future work can be performed:

- The moisture dependent mechanical properties such as elastic modulus, secondary creep strain at different MSL conditions can be incorporated into simulation to better predict the moisture induced failure phenomena.
- Nanoindentation technology can be used to determine the viscoelastic property of package which can provide more reliable material property. These properties can be used to further develop a reliable model to failure prediction.
- Curing conditions effects the property of polymers. A detailed study can be developed on polymeric materials to see how the viscoelastic property as well as elastic property changes with curing temperature and time.
- Microstructure study can be performed to observe the behavior of materials exposed to different temperature/humidity condition.

REFERENCES

[1] J. Lau, *Ball grid array technology*. McGraw-Hill, 1994.

[2] K. Gilleo, *MEMS/MOEMS Packaging: Concepts, Designs, Materials, and Processes*. New York, NY: McGraw-Hill, 2005.

[3] V. P. Shevelko, *Electronic Packaging and Interconnection Handbook, 3rd edition*. McGraw-Hill, 2001.

[4] E. M. Davis, W. E. Harding, R. S. Schwartz, and J. J. Corning, "Solid Logic Technology: Versatile, high-performance microelectronics," *IBM Journal of Research and Development*, vol. 8, no. 2, pp. 102–114, 1964.

[5] C. Zweben, *Advanced electronic packaging materials*. IEEE Press, 2005.

[6] C. Harper, *Electronic Packaging and Interconnection Handbook*. McGraw-Hill, 2005.

[7] F. Nakano, T. Soga, and S. Amagi, "Resin-Insertion Effect on Thermal Cycle Resistivity of Flip-Chip Mounted LSI Devices," *International Society of Hybrid Microelectronics*, pp. 536–541, 1987.

[8] L. C. Brinson and T. S. Gates, "Effects of physical aging on long term creep of polymers and polymer matrix composites," *International Journal of Solids and Structures*, vol. 32, no. 6–7, pp. 827–846, 1995.

[9] S. Luo and C. P. Wong, "Study on influence of environment on adhesion performance of underfill for flip chip application," *International Symposium on Electronic Materials and Packaging*, pp. 243–250, 2000.

[10] J. H. Okura, A. Dasgupta, and J. F. J. M. Caers, "Hygro-mechanical durability of underfilled flip-chip-on-board interconnects," *Journal of Electronic Packaging, Transactions of the ASME*, vol. 124, no. 3, pp. 184–187, 2002.

[11] F. Feustel, S. Wiese, and E. Meusel, "Time-dependent material modeling for finite element analyses of flip chips," *Proceedings of the 50th IEEE Electronic Components and Technology Conference*, pp. 1548–1553, 2000.

[12] S. Han and K. K. Wang, "Analysis of the flow of encapsulant during underfill encapsulation of flip-chips," *IEEE Transactions on Components Packaging and Manufacturing Technology*, vol. 20, no. 4, pp. 424–433, 1997.

[13] T. Lombardi, F. Pompeo, J. Coffin, D. Plouffe, and C. Reynolds, "Rapid encapsulant for use in ceramic chip-carrier applications," *IBM-MicroNews*, vol. 5,

no. 4, 1999.

[14] P. S. Ho and T. Kwok, “Electromigration in metals,” *Reports on Progress in Physics*, vol. 52, no. 3, pp. 301–348, 1989.

[15] Y. Zhang, Y. Liu, L. Liang, and X. Fan, “The effect of atomic density gradient in electromigration,” *International Journal of Materials and Structural Integrity*, vol. 6, no. 1, pp. 36–53, 2012.

[16] D. Yu, J. B. Kwak, S. Park, and J. Lee, “Dynamic responses of PCB under product-level free drop impact,” *Microelectronics Reliability*, vol. 50, no. 7, pp. 1028–1038, 2010.

[17] Y. Zhao, C. Basaran, A. Cartwright, and T. Dishongh, “Thermomechanical behavior of micron scale solder joints under dynamic loads,” *Mechanics of Materials*, vol. 32, no. 3, pp. 161–173, 2000.

[18] J. Gomez, M. Lin, and C. Basaran, “Damage Mechanics Modeling of Concurrent Thermal and Vibration Loading on Electronics Packaging,” *Multidiscipline Modeling in Materials and Structures*, vol. 2, no. 3, pp. 309–326, 2006.

[19] P. Lall, R. Lowe, and K. Goebel, “Prognostication of accrued damage in board assemblies under thermal and mechanical stresses,” *Proceedings of the 62nd IEEE Electronic Components and Technology Conference*, pp. 1475–1487, 2012.

[20] Z. Qian, J. Wang, J. Yang, and S. Liu, “Visco-elastic-plastic properties and constitutive modeling of underfills,” *IEEE Transactions on Components and Packaging Technologies*, vol. 22, no. 2, pp. 152–157, 1999.

[21] Y. Rao, S. H. Shi, and C. P. Wong, “An improved methodology for determining temperature dependent moduli of underfill encapsulants,” *IEEE Transactions on Components and Packaging Technologies*, vol. 23, no. 3, pp. 434–439, 2000.

[22] M. S. Islam, J. C. Suhling, P. Lall, B. Xu, and R. W. Johnson, “Measurements and modeling of the temperature dependent material behavior of underfill encapsulants,” *Proceedings of the 53rd IEEE Electronic Components and Technology Conference*, pp. 1636–1643, 2003.

[23] M. S. Islam, J. C. Suhling, and P. Lall, “Measurement of the temperature dependent constitutive behavior of underfill encapsulants,” *IEEE Transactions on Components and Packaging Technologies*, vol. 28, no. 3, pp. 467–476, 2005.

[24] P. Lall, S. Islam, G. Tian, and J. C. Suhling, “Nano-Underfills for High-Reliability Applications in Extreme Environments,” *IEEE Transactions on Components and Packaging Technologies*, vol. 31, no. 1, pp. 114–125, 2008.

[25] B. Wun and J. Lau, “Characterisation and Evaluation of the Underfill Encapsulants for Flip Chip Assembly,” *Circuit World*, vol. 21, no. 3, pp. 25–32, 1995.

[26] M.-L. Sham and J.-K. Kim, “Experiment and Numerical Analysis of the Residual Stresses in Underfill Resins for Flip Chip Package Applications,” *Journal of Electronic Packaging*, vol. 127, no. 1, pp. 47–51, 2005.

[27] G. Q. Zhang, W. D. van. Driel, and X. J. Fan, *Mechanics of Microelectronics*.

Springer, 2006.

[28] X. J. Fan, "Moisture Related Reliability in Electronic Packaging," *Electronic Component Technology Conference (ECTC) Professional Development Course Handout*, pp. 1–92, 2008.

[29] X. J. Fan, G. Q. Zhang, W. D. Van Driel, and L. J. Ernst, "Interfacial delamination mechanisms during soldering reflow with moisture preconditioning," *IEEE Transactions on Components and Packaging Technologies*, vol. 31, no. 2, pp. 252–259, 2008.

[30] W. D. van Driel, M. A. van Gils, X. J. Fan, G. Q. Zhang, and L. J. Ernst, "Driving mechanisms of delamination related reliability problems in exposed pad packages," *IEEE Transactions on Components and Packaging Technologies*, vol. 31, no. 2, pp. 260–268, 2008.

[31] D. A. Bond and P. A. Smith, "Modeling the transport of low-molecular-weight penetrants within polymer matrix composites," *Applied Mechanics Reviews*, vol. 59, no. 1–6, pp. 249–267, 2006.

[32] J. E. Galloway and B. M. Miles, "Moisture absorption and desorption predictions for plastic ball grid array packages," *IEEE Transactions on Components Packaging and Manufacturing Technology*, vol. 20, no. 3, pp. 274–279, 1997.

[33] R. L. Shook, T. R. Conrad, V. S. Sastry, and D. B. Steele, "Diffusion model to derate moisture sensitive surface mount IC's for factory use conditions," *IEEE transactions on components, packaging and manufacturing technology. Part C. Manufacturing*, vol. 19, no. 2, pp. 110–118, 1996.

[34] X. Fan, J. Zhou, and A. Chandra, "Package structural integrity analysis considering moisture," *Proceedings of the 58th IEEE Electronic Components and Technology Conference*, pp. 1054–1066, 2008.

[35] E. Stellrecht, B. Han, and M. G. Pecht, "Characterization of Hygroscopic Swelling Behavior of Mold Compounds and Plastic Packages," *IEEE Transactions on Components and Packaging Technologies*, vol. 27, no. 3, pp. 499–506, 2004.

[36] E. H. Wong, R. Rajoo, S. W. Koh, and T. B. Lim, "The Mechanics and Impact of Hygroscopic Swelling of Polymeric Materials in Electronic Packaging," *Journal of Electronic Packaging*, vol. 124, no. 2, pp. 122–126, 2002.

[37] J. Zhou and J. S. Law, "Effect of Non-Uniform Moisture Distribution on the Hygroscopic Swelling Coefficient," *IEEE Transactions on Components and Packaging Technologies*, vol. 31, no. 2, pp. 269–276, 2008.

[38] H. Ardebili, E. H. Wong, and M. Pecht, "Hygroscopic swelling and sorption characteristics of epoxy molding compounds used in electronic packaging," *IEEE Transactions on Components and Packaging Technologies*, vol. 26, no. 1, pp. 206–214, 2003.

[39] X. Q. Shi, Y. L. Zhang, W. Zhou, and X. J. Fan, "Effect of hygrothermal aging on interfacial reliability of silicon/ underfill/FR-4 assembly," *IEEE Transactions on Components and Packaging Technologies*, vol. 31, no. 1, pp. 94–103, 2008.

[40] J. Zhou, S. P. Lahoti, M. P. Sitlani, S. C. Kallolimath, and R. Putta, “Investigation of non-uniform moisture distribution on determination of hygroscopic swelling coefficient and finite element modeling for a flip chip package,” *Proceedings of the 6th International Conference on Thermal, Mechanical and Multi-Physics Simulation and Experiments in Micro-Electronics and Micro-Systems - EuroSimE*, pp. 112–119, 2005.

[41] M. H. Shirangi, W. H. Muller, and B. Michel, “Effect of nonlinear hygro-thermal and residual stresses on the interfacial fracture in plastic IC packages,” *Proceedings of the 59th IEEE Electronic Components and Technology Conference*, pp. 232–238, 2009.

[42] K. Gilleo, M. Witt, D. Blumel, and P. Ongley, “Towards a better understanding of underfill encapsulation for flip chip technology: Proposed developments for the future,” *Microelectronics International*, vol. 16, no. 2, pp. 39–43, 1999.

[43] J. Lin, A. Teng, and M. M. F. Yuen, “Fast, low cost method to check for moisture in epoxy molding compound,” *Proceedings of the 2nd IEEE Electronic Packaging Technology Conference, EPTC*, pp. 359–361, 1998.

[44] T. Ferguson and J. Qu, “Effect of moisture on the interfacial adhesion of the underfill/solder mask interface,” *Journal of Electronic Packaging, Transactions of the ASME*, vol. 124, no. 2, pp. 106–110, 2002.

[45] N. J. Chhanda, J. C. Suhling, and P. Lall, “Effects of Moisture Exposure on the Mechanical Behavior of Polymer Encapsulants in Microelectronic Packaging,” *Proceedings of ASME InterPACK*, p. V001T07A017, 2013.

[46] N. J. Chhanda, J. C. Suhling, and P. Lall, “Effects of moisture exposure on the mechanical behavior of flip chip underfills in microelectronic packaging,” *Proceedings of IEEE ITherm*, pp. 333–345, 2014.

[47] C.-T. Kuo, M.-C. Yip, and K.-N. Chiang, “Time and temperature-dependent mechanical behavior of underfill materials in electronic packaging application,” *Microelectronics Reliability*, vol. 44, no. 4, pp. 627–638, 2004.

[48] T. P. Ferguson and J. Qu, “Moisture and temperature effects on the Reliability of interfacial adhesion of a polymer/metal interface,” *Proceedings of the 54th IEEE Electronic Components and Technology Conference*, pp. 1752–1758, 2004.

[49] T. P. Ferguson and J. Qu, “Elastic modulus variation due to moisture absorption and permanent changes upon redrying in an epoxy based underfill,” *IEEE Transactions on Components and Packaging Technologies*, vol. 29, no. 1, pp. 105–111, 2006.

[50] T. P. Ferguson, “Moisture and Interfacial adhesion in microelectronic assembles,” Ph.D. dissertation, Georgia Institute of Technology, 2004.

[51] S. Luo and C. P. Wong, “Influence of temperature and humidity on adhesion of underfills for flip chip packaging,” *IEEE Transactions on Components and Packaging Technologies*, vol. 28, no. 1, pp. 88–94, 2005.

[52] Y. He and X. J. Fan, “Real-Time Characterization of Moisture Absorption and

Desorption," *Moisture Sensitivity of Plastic Packages of IC Devices*, Boston, MA: Springer US, pp. 71–89, 2010.

[53] X. Chen, S. Zhao, and L. Zhai, "Moisture Absorption and Diffusion Characterization of Molding Compound," *Journal of Electronic Packaging*, vol. 127, no. 4, pp. 460–465, 2005.

[54] M. D. Placette, X. J. Fan, J.-H. Zhao, and D. Edwards, "Dual stage modeling of moisture absorption and desorption in epoxy mold compounds," *Microelectronics Reliability*, vol. 52, no. 7, pp. 1401–1408, 2012.

[55] H. Shirangi, J. Auersperg, M. Koyuncu, H. Walter, W. H. Muller, and B. Michel, "Characterization of dual-stage moisture diffusion, residual moisture content and hygroscopic swelling of epoxy molding compounds," *Proceedings of the International Conference on Thermal, Mechanical and Multi-Physics Simulation and Experiments in Micro-Electronics and Micro-Systems - EuroSimE, ,* pp. 1–8, 2008.

[56] E. H. Wong and R. Rajoo, "Moisture absorption and diffusion characterisation of packaging materials - advanced treatment," *Microelectronics Reliability*, vol. 43, no. 12, pp. 2087–2096, 2003.

[57] Y. C. Lin and X. Chen, "Moisture sorption–desorption–resorption characteristics and its effect on the mechanical behavior of the epoxy system," *Polymer*, vol. 46, no. 25, pp. 11994–12003, 2005.

[58] Y. Sun, "Characterization of Non-linear Polymer Properties to Predict Process Induced Warpage and Residual Stress of Electronic Packages," Ph.D. dissertation, University of Maryland, 2016.

[59] I. Emri, "Rheology of Solid Polymers," *Rheology Reviews*, vol. 2005, pp. 49–100, 2005.

[60] S. Jazouli, W. Luo, F. Brémand, and T. Vu-Khanh, "Nonlinear creep behavior of viscoelastic polycarbonate," *Journal of Materials Science*, vol. 41, no. 2, pp. 531–536, 2006.

[61] E. T. J. Klompen and L. E. Govaert, "Nonlinear Viscoelastic Behaviour of Thermorheologically Complex Materials," *Mechanics of Time-Dependent Materials*, vol. 3, no. 1, pp. 49–69, 1999.

[62] C. F. Popelar and K. M. Liechti, "Multiaxial Nonlinear Viscoelastic Characterization and Modeling of a Structural Adhesive," *Journal of Engineering Materials and Technology*, vol. 119, no. 3, pp. 205–210, 1997.

[63] L. Chen, Q. Zhang, G. Wang, X. Xie, and Z. Cheng, "The effects of underfill and its material models on thermomechanical behaviors of a flip chip package," *IEEE Transactions on Advanced Packaging*, vol. 24, no. 1, pp. 17–24, 2001.

[64] M.-L. Sham, J.-K. Kim, and J.-H. Park, "Numerical analysis of plastic encapsulated electronic package reliability: Viscoelastic properties of underfill resin," *Computational Materials Science*, vol. 40, no. 1, pp. 81–89, 2007.

[65] J. Thompson, S. Groothuis, and P. Koeneman, "Transient Behavior of a Polymer

Fill Material with Time Dependent Viscoelastic Properties." [Online]. Available: https://www.ansys.com/-/media/ansys/corporate/resourcelibrary/conference-paper/2002-int-ansys-conf-56.pdf

[66] F. Liu, G. Meng, and M. Zhao, "Viscoelastic Influence on Dynamic Properties of PCB Under Drop Impact," *Journal of Electronic Packaging*, vol. 129, no. 3, pp. 266–272, 2007.

[67] M. Mottahedi, A. Dadalau, A. Hafla, and A. Verl, "Numerical Analysis of Relaxation Test Based on Prony Series Material Model," *Integrated Systems, Design and Technology*, Springer Berlin Heidelberg, pp. 79–91, 2011.

[68] M. Fernanda, P. Costa, and C. Ribeiro, "Parameter Estimation of Viscoelastic Materials: A Test Case with Different Optimization Strategies," *AIP Conference Proceedings*, vol. 1389, no. 1, pp. 771–774, 2011.

[69] H. Yan, X. Zhang, and L. Zhang, "Methods of Fitting the Prony Series of Viscoelastic Models of Asphalt Mixture Based on Dynamic Modulus," *ICTE 2011*, pp. 1384–1389, 2011.

[70] S. W. Park and Y. R. Kim, "Fitting Prony-Series Viscoelastic Models with Power-Law Presmoothing," *Journal of Materials in Civil Engineering*, vol. 13, no. 1, pp. 26–32, 2001.

[71] S.-H. Chae, J.-H. Zhao, D. R. Edwards, and P. S. Ho, "Characterization of the Viscoelasticity of Molding Compounds in the Time Domain," *Journal of Electronic Materials*, vol. 39, no. 4, pp. 419–425, 2010.

[72] Y. He, "Thermomechanical and viscoelastic behavior of a no-flow underfill material for flip-chip applications," *Thermochimica Acta*, vol. 439, no. 1–2, pp. 127–134, 2005.

[73] N. J. Chhanda, J. C. Suhling, and P. Lall, "Experimental Characterization and Viscoplastic Modeling of the Temperature Dependent Material Behavior of Underfill Encapsulants," *Proceedings of ASME InterPACK*, pp. 749–761, 2011.

[74] N. J. Chhanda, J. C. Suhling, and P. Lall, "Impelementatoin of a viscoelastic model for the temperature dependent material behavior of underfill encapsulants," *Proceedings of IEEE ITherm*, pp. 269–281, 2012.

[75] A. Syed, "Updated Life Prediction Models for Solder Joints with Removal of Modeling Assumptions and Effect of Constitutive Equations," *Proceedings of the 7th International Conference on Thermal, Mechanical and Multiphysics Simulation and Experiments in Micro-Electronics and Micro-Systems - EuroSime*, pp. 1–9, 2006.

[76] B. A. Zahn, "Solder joint fatigue life model methodology for 63Sn37Pb and 95.5Sn4Ag0.5Cu materials," *Proceedings of the 53rd IEEE Electronic Components and Technology Conference*, pp. 83–94, 2003.

[77] S. Ridout and C. Bailey, "Review of methods to predict solder joint reliability under thermo-mechanical cycling," *Fatigue and Fracture of Engineering Materials and Structures*, vol. 30, no. 5, pp. 400–412, 2007.

[78] R. Darveaux, “Effect of simulation methodology on solder joint crack growth correlation,” *Proceedings of the 50th IEEE Electronic Components and Technology Conference*, pp. 1048–1058, 2000.

[79] S. Michaelides and S. K. Sitaraman, “Effect of material and geometry parameters on the thermo-mechanical reliability of flip-chip assemblies,” *Thermomechanical Phenomena in Electronic Systems -Proceedings of the Intersociety Conference*, pp. 193–200, 1998.

[80] A. Schubert, R. Dudek, B. Michel, H. Reichl, and H. Jiang, “Materials mechanics and mechanical reliability of flip chip assemblies on organic substrates,” *Proceedings of the International Symposium and Exhibition on Advanced Packaging Materials Processes, Properties and Interfaces*, pp. 106–109, 1997.

[81] R. Darveaux, L. Norton, and F. Carney, “Temperature dependent mechanical behavior of plastic packaging materials,” *Proceedings of the 45th IEEE Electronic Components and Technology Conference*, pp. 1054–1058, 1995.

[82] I. C. Ume, T. Martin, and J. T. Gatro, “Finite element analysis of PWB warpage due to the solder masking process,” *IEEE Transactions on Components Packaging and Manufacturing Technology Part A*, vol. 20, no. 3, pp. 295–306, 1997.

[83] H. Zhu, Y. Guo, W. Y. Li, A. A. Tseng, and B. Martin, “Micro-mechanical characterizations of solder mask materials,” *Proceedings of the 3rd IEEE Electronic Packaging Technology Conference, EPTC*, pp. 148–153, 2000.

[84] C. Lin, J. C. Suhling, and P. Lall, “Physical aging and evolving mechanical behavior of underfill encapsulants,” *Proceedings of IEEE ITherm*, pp. 695–704, 2008.

[85] C. Lin, J. C. Suhling, and P. Lall, “Isothermal aging induced evolution of the material behavior of underfill encapsulants,” *Proceedings of the 59th IEEE Electronic Components and Technology Conference*, pp. 134–149, 2009.

[86] C. Lin, N. J. Chhanda, J. C. Suhling, and P. Lall, “The influence of aging on the creep behavior of underfill encapsulants,” *Proceedings of IEEE ITherm*, pp. 1–11, 2010.

[87] P. R. Chowdhury, N. J. Chhanda, J. C. Suhling, and P. Lall, “Experimental Characterization of Underfill Materials Exposed to Moisture Including Preconditioning,” *Proceedings of ASME InterPACK*, p. V002T01A013, 2015.

[88] P. R. Chowdhury, J. C. Suhling, and P. Lall, “Experimental characterization of underfill materials exposed to different moisture conditions,” *Proceedings of IEEE ITherm*, pp. 1–12, 2017.

[89] J. R. Bolton, “Fundamentals of Ultraviolet Treatment – Terms and Definitions do Matter !,” *Water Conditioning and Purification International*, pp. 27–31, 2004.

[90] J. Ramli, A. R. Jeefferie, and M. M. Mahat, “Effects of uv curing exposure time to the mechanical And physical properties of the epoxy and vinyl ester Fiber glass laminates composites,” *ARPN Journal of Engineering and Applied Sciences*, vol. 6, no. 4, pp. 104–109, 2011.

[91] Nanoscience, “Components in a SEM - Nanoscience Instruments,” 2016. [Online]. Available: https://www.nanoscience.com/techniques/scanning-electron-microscopy/components/.

[92] “Scanning Electron Microscope.” [Online]. Available: https://en.wikipedia.org/wiki/Scanning_electron_microscope.

[93] C. Tzikang, “Determining a Prony Series for a Viscoelastic Material From Time Varying Strain Data,” *NASA/TM-2000-210123, NAS 1.15:210123, ARL-TR-2206*, pp. 1–21, 2000.

[94] J. D. Ferry, *Viscoelastic properties of polymers*, 3rd ed. New York: Wiley, 1980.

[95] S. W. Park and R. A. Schapery, “Methods of interconversion between linear viscoelastic material functions. Part I - A numerical method based on Prony series,” *International Journal of Solids and Structures*, vol. 36, no. 11, pp. 1653–1675, 1999.

[96] W. N. Findley, J. S. Lai, K. Onaran, and R. M. Christensen, “Creep and Relaxation of Nonlinear Viscoelastic Materials With an Introduction to Linear Viscoelasticity,” *Journal of Applied Mechanics*, vol. 44, no. 2, pp. 364–364, 1977.

[97] F. R. Schwarzl and L. C. E. Struik, “Analysis of relaxation measurements,” *Advances in Molecular Relaxation Processes*, vol. 1, no. 3, pp. 201–255, 1968.

[98] D. J. O’Brien, P. T. Mather, and S. R. White, “Viscoelastic properties of an epoxy resin during cure,” *Journal of Composite Materials*, vol. 35, no. 10, pp. 883–904, 2001.

[99] K. Ninomiya and J. D. Ferry, “Some approximate equations useful in the phenomenological treatment of linear viscoelastic data,” *Journal of Colloid Science*, vol. 14, no. 1, pp. 36–48, 1959.

[100] K. Menard, “Time and Temperature Scans Part II,” *Dynamic Mechanical Analysis*, vol. 2, pp. 123–143, 2008.

[101] M. M. Basit *et al.*, “Thermal cycling reliability of aged PBGA assemblies - Comparison of Weibull failure data and finite element model predictions,” *Proceedings of the 65th IEEE Electronic Components and Technology Conference*, pp. 106–117, 2015.

[102] M. Motalab *et al.*, “Correlation of reliability models including aging effects with thermal cycling reliability data,” *Proceedings of the 63rd IEEE Electronic Components and Technology Conference*, pp. 986–1004, 2013.

[103] P. R. Chowdhury, J. C. Suhling, and P. Lall, “Mechanical Characterization of Solder Mask Materials,” *Proceedings of IEEE ITherm*, pp. 1133–1141, 2018.

[104] P. R. Chowdhury, J. C. Suhling, and P. Lall, “The Effects of Curing Profile, Temperature, and Aging on the Mechanical Behavior of Solder Mask Materials,” *Proceedings of ASME InterPACK*, p. V001T03A004-V001T03A004, 2018.

APPENDIX

MATLAB CODE FOR PRONY COEFFICIENT

```
%==============Determining Prony Coefficient==========%

clc;
clear;
xdata = xlsread('try5.xlsx',15,'E167:E554');    %==time
data
ydata =
xlsread('try5.xlsx',15,'F167:F554');    %==Relaxation
Modulus data

E_inf = 61220915;   % Specifiy infinite relaxation modulus
value

%======= Equation ===%

fun = @(x,xdata)((E_inf+x(1)*exp(-xdata/x(2))+x(3)*exp(-
xdata/x(4))+x(5)*exp(-xdata/x(6))+...
    x(7)*exp(-xdata/x(8))+x(9)*exp(-
xdata/x(10))+x(11)*exp(-xdata/x(12))+x(13)*exp(-
xdata/x(14))));

%==Initial guess

x0=[158631040.7,5.00E-01,...
    129931025.1,1.07E+00,...
    84461926.79,1.05E+01,...
    69827695.62,6.35E+01,...
    67433236.17,1.02E+02,...
    61220915.86,1.00E+03,...
    61220915.86,2.10E+03];

%====Lsqcurvefit algorithm===%

options = optimoptions('lsqcurvefit','Algorithm','trust-
region-reflective',...
```

```
    'MaxFunEvals',1e100,'MaxIter',1e100,'TolFun',1e-20);


lb = zeros(size(x0));
ub =
[10e20,10e20,10e20,10e20,10e20,10e20,10e20,10e20,10e20,10e2
0,10e20,10e20,10e20,10e20];
x = lsqcurvefit(fun,x0,xdata,ydata,lb,ub,options)
xcoeff=x';


times = linspace(xdata(1),xdata(end),2000);
loglog(xdata,ydata,'ko',times,fun(x,times),'b-')
xlim([10e-4 2000])
ylim([1e7 8e9])
legend('Data','Fitted exponential')
title('Data and Fitted Curve')
fittedydata=(fun(x,times));

%==================================End=====================
========%
```